Finite element analysis of fractured rock mass with PLAXIS 2D using different discontinuity constitutive models

M.Sc. Thesis in Geo-Engineering

Vasileios Skordilis

Delft, September 2023

Finite element analysis of fractured rock mass with PLAXIS 2D using different discontinuity constitutive models

By

Vasileios Skordilis

in partial fulfilment of the requirements for the degree of

Master of Science
in Civil Engineering

at the Delft University of Technology
to be defended publicly on September 22, 2023

Graduation Committee:	Dr. Ir. R.B.J. Brinkgreve	TU Delft, Geo-Engineering
	Prof. Dr. M.A. Hicks	TU Delft, Geo-Engineering
	Dr. A.M.H. Pluymakers	TU Delft, Applied Geophysics & Petrophysics
	Dr. Ir. T.A Bui	Seequent, the Bentley subsurface company
	Dr. Ir. G. Cammarata	Seequent, the Bentley subsurface company

Cover: Norwegian Geotechnical Institute, field of construction and infrastructure
Section of Rock Engineering

An electronic version of this thesis is available at http://repository.tudelft.nl/.

SEEQUENT TU Delft PLAXIS

Acknowledgements

This dissertation represents the final work performed for the completion of my Master of Science studies at the Faculty of Civil Engineering and Geosciences at Delft University of Technology. The thesis was conducted in collaboration with PLAXIS BV, where I had the chance to work as an intern, gaining invaluable experiences that made me grow on both professional and personal levels.

The fulfilment of this work was possible thanks to the support, guidance, and patience of several people from PLAXIS BV and TU Delft. First of all, I would like to express my heartfelt gratitude to my daily supervisors at PLAXIS BV, Tuan Bui and Giuseppe Cammarata for their unwavering assistance and guidance in each one of the stages of the thesis while also for their unconditional willingness to share with me their knowledge and insights, which are invaluable for me. Their diligence and their dedication to my work were inspiring and motivated me to strive for the clarity and precision of my dissertation. I am especially thankful to Prof. R. Brinkgreve, Prof. M. Hicks and Prof. Anne Pluymakers for being members of the evaluation committee of my thesis and for supporting me with their constructive feedback. Additionally, I extend my sincere appreciation to Anita Laera for her support, to Sandro Brasile and all the colleges at PLAXIS BV for offering me a friendly and stimulating working environment.

My deepest gratitude goes to my family whose unwavering support has been a cornerstone of my accomplishments. Their encouragement and their belief in my abilities have uplifted me during the challenging times of this important stage of my life.

Last but not least, my special thanks are extended to each one of my friends. Their encouragement and support have been the driving force behind my academic journey and my effort to achieve my goals.

September 2023

Vasileios Skordilis

Abstract

The stability of rock engineering projects is tightly related to the mechanical behaviour of rock discontinuities. Although the mechanical behaviour of a discontinuity is often associated with shearing (sliding), experimental data have shown that it can be accompanied by more complex phenomena such as dilation and post-peak strength reduction.

Numerous researchers have contributed to the understanding and modelling of discontinuities behaviour. However, many of the constitutive models available in the literature are questionable when applied in practice either because they are highly empirical with parameters that are hardly determined or because they oversimplify the examined behaviour. Moreover, the models are often proposed for a certain range of stresses and specific stress paths, which makes numerical implementation difficult for large-scale engineering applications. This dissertation aims to evaluate the capabilities and the limitations of different constitutive models for rock discontinuity in the context of both numerical **implementation** and **simulation** of the mechanical behaviour of rock discontinuity.

The first part of the research project investigates the main features of the existing models in the literature. From the investigated models, the two models highly adopted in research and engineering practice, namely the Coulomb's model and Barton-Bandis's model, are extensively investigated. Some enhancements and modifications are made to these two models to improve their modelling capabilities and ensure the numerical stability of numerical implementation. Regarding the Coulomb model, the adopted modifications include the reformulation of the model within the framework of strain softening providing a rigorous implemented version that describes the post-peak behaviour of a discontinuity adopting a linear reduction of the strength. Additionally, the employed modifications to the Barton-Bandis model provide a robust version of the model applying reformulations to the original yield surface that increase its validity in the whole range of the τ-σ_n space. Furthermore, a simplified definition of the post-peak behaviour, which aligns with the original formulation of the model but at the same time allows for a straightforward numerical implementation, is proposed. To validate the implementation of these models in PLAXIS (implementation done by the PLAXIS research team), the models are implemented in Python scripts for Constant Normal Load (CNL) shear test configuration. Concretely the implemented models are calibrated with experimental data to simulate CNL tests using a PLAXIS 2D Finite Element (FE) model and the obtained results are compared with both Python theoretical simulation and experimental results to verify the FE implementation. The results of these simulations validate the numerical implementation in PLAXIS and prove the applicability of the enhanced models to reproduce with adequate accuracy the mechanical behaviour of a rock discontinuity on a lab scale.

Finally, the implemented constitutive laws are employed to perform a FE analysis of a large-scale application of a deep underground excavation in a discontinuous rock layer using PLAXIS 2D. To facilitate the creation of this complex geometry, an automatic discontinuity network generator is developed and improved using PLAXIS Python scripting API. The implemented discontinuity laws are then applied to the randomly generated discontinuity sets to simulate the behaviour of the rock mass. Stress and failure analyses are performed for the most critical discontinuities and wedges formed around the excavation to validate the numerical implementation and analyze the applicability of the constitutive models. The analysis of the boundary value problem confirms both the reliability of the numerical implementation and the applicability of the enhanced constitutive laws to simulate the analyzed large-scale problem.

Contents

List of Figures

List of Tables

1 Introduction

1.1 Problem description

1.1.1 Overview

The term “Rock Mass” refers to the generally discontinuous, inhomogeneous, anisotropic, and non-linear elastoplastic material consisting of intact rock and discontinuities of different types and scales that represent breaks in the rock continuum. ”Discontinuity” is a general term denoting any separation in a rock mass having low (or nil) tensile strength. It is a collective term for most types of joints, weak bedding planes, weak schistosity planes, weakness zones, and faults. Discontinuities and intact rock blocks dictate the overall behaviour of rock mass. Rock engineering projects like underground excavations, designing and stabilization of slopes, foundations on rocks, and dams are vulnerable to movements of intact rock blocks along rock discontinuities even if the intact rock blocks themselves are stiff.

Movements along discontinuities can occur in multiple directions depending on kinematic constraints and the external forces acting on the structure. The importance of acquiring a deep understanding of the mechanical behaviour of discontinuities is highlighted by several cases which indicate the failure of rock engineering constructions due to the limited understanding or wrong estimation of the discontinuities’ behaviour. These considerations have been documented by many case studies where failures occurred, such as the failure of the Malpasset dam in 1954, in the southern part of France, which caused a considerable number of fatalities. After the sudden failure, investigations were executed in the rock valley, where the dam was located, and it was observed that the structure failed due to the sliding of rock blocks along discontinuities which were in the foundation rock mass (Duffaut, 2013).

In the last decades, many researchers focused their interest on understanding all the aspects of the behaviour of rock masses and trying to suggest reliable estimates of the variation of strength and deformation characteristics of discontinuities in fractured rock masses. Generally, the main characteristics which control the stress and strain behaviour of discontinuities are the level of the effective normal stress acting on them, the properties of the rock walls (including the rock type) and the filling material between them (if exists), the degree of roughness and weathering and the size of the discontinuities.

Several constitutive models have been developed to simulate the mechanical behaviour of rock discontinuities, based on either empirical or theoretical methods. However, constitutive models are only a simplification of reality, and it is of fundamental importance to understand the assumptions they are based on, together with the possible advantages and limitations, when modelling rock mass behaviour. Frequently, simple linear models are preferred because they require few and easy-to-determine parameters, but their drawback is that they cannot capture important aspects of the mechanical behaviour observed experimentally. Therefore, this Master of Science thesis focuses on performing numerical analyses with the FE software PLAXIS 2D of discretely fractured rock mass using two constitutive laws for simulating the mechanical behaviour of discontinuities.

1.1.2 Problem statement

The stability of rock engineering projects is highly dependent on the mechanical behaviour of discontinuities. Neglecting the behaviour of fractures often leads to a misinterpretation of the rock mass response to external loading conditions. Although the mechanical behaviour of a

discontinuity is often associated with shearing (sliding), experimental data have shown that it can be accompanied by more complex phenomena such as dilation and post-peak strength reduction. These concepts indicate that the mechanical behaviour of discontinuities is non-linear. Proper consideration of discontinuity behaviour is crucial for the reliable stability assessment of rock engineering works. Numerous models have been proposed by researchers (e.g. Patton (1966), Goodman (1976), Barton et al. (1985), Saeb and Amadei (1992), Grasselli and Egger (2003)) which have helped rock engineers to understand the evolution of stress and deformation characteristics of discontinuities. However, many of the models available in the literature are questionable when applied in practice either because they are very simplistic (linear models like Coulomb) or because they are strongly dependent on empirical parameters or require complex input parameters which are hard to calibrate through lab or in situ tests.

1.2 Objective

In this context, the main objective of this Master's project is to evaluate the capabilities and limitations of different constitutive models for rock discontinuities in terms of numerical implementation and modelling of the mechanical behaviour of fractured rock masses.

1.3 Research questions

To accomplish the research objective, the following research questions were formulated:

- How, can the behaviour of a single discontinuity be modelled?
  - Which mechanical features control the behaviour of discontinuities under mechanical loading?
  - Which are the capabilities of the discontinuity constitutive models proposed in the literature?
  - Do the conditions under which these models were developed apply to practical engineering problems?
  - How accurate are the proposed models with respect to the observed behaviour?
  - How to calibrate the parameters of these models?

- How to validate the implemented model?
  - How to set up a FEM model for validation?
  - Which test conditions are going to be applied?
  - Which experimental data are going to be selected for comparison?

- To what extent can the implemented model capture the real mechanical behaviour of a fractured rock mass?
  - How does each model perform in a FEA of a Boundary Value Problem?
  - Which features of the fractured rock mass cannot be modelled in the analysed practical application?

1.4 Research approach

The research methodology is divided into the following consecutive procedures:

- Literature review:

An indispensable part of this Master's Thesis is to primarily conduct a literature review to acquire the theoretical background required to adequately respond to the research questions. The literature review will be focused on the investigation of constitutive models available in

the literature which can model the behaviour of discontinuities. For each model mainly the following four aspects will be examined:

- The assumptions that each model is based on
- The complexity of the used parameters
- The understanding of the proposed mathematical approaches which describe the evolution of shear stress, shear stiffness, normal stress, normal stiffness, and normal closure with the increase of shear displacement
- The amount of data through which the model has been validated and the alignment of the extracted results with the experimental data

- Formulation of the incremental equations of the models for the theoretical simulation of a typical Constant Normal Load shear test:

  The constitutive laws found in the literature which will be considered the most suitable from the aspect of both their theoretical consistency and practical values will be selected for further investigation. The governing equations of the selected models will be written in an incremental form within the framework of Plasticity theory to serve as the base for the Finite Element implementation (FE) In addition, the formulated equations are implemented in a Python script to theoretically simulate a typical shear test under Constant Normal Load conditions (using an explicit integration scheme) and support the reliability of the FE numerical implementation.

- Further development of the tool for generating discontinuity networks:

  During previous research activities, a tool for the automatic generation of sets of discontinuities in a FEM model has been created. The research framework of this Master's thesis includes the further development of the existing tool. The considered tool will be updated with the aim of being able to generate the complete geometry of a Boundary Value problem with sets of discontinuities that can automatically be trimmed when extending outside the boundary of the model. The tool will be used in the following phases.

- Models' validation:

  Once the implementation of the constitutive laws is completed by members of the research team of PLAXIS, its validity will be confirmed. More specifically, for each constitutive law, a simple numerical model (made of two blocks and a single discontinuity) will be used to simulate shear tests. Furthermore, the implemented Python script will be used to simulate theoretically the same shear tests. A comparison between the two simulations will be conducted to verify the validity of the implementation in PLAXIS.

- Boundary value problem application:

  Finally, the applicability of the implemented constitutive laws will be tested in an underground rock excavation application where the rock mass is simulated as a discretely fractured medium. To further investigate the impact of using more advanced constitutive laws, a comparison of the results obtained through the adoption of the Mohr-Coulomb model (which is already implemented in PLAXIS) for the same engineering application cases will also be performed.

- Results analysis:

  The results of the performed analysis will be critically evaluated to verify the implementation of different models and analyse the advantages and limitations of the implemented constitutive models for the simulation of a fractured rock mass and to provide recommendations for potential future improvements.

2 Theoretical Framework

2.1 Introduction

In the last few decades, many researchers have provided essential contributions to studying the mechanical response of rock discontinuities. The main scope of the present chapter is to introduce and describe existing constitutive models from the field of discontinuity modelling found in the literature by indicating their main characteristics.

The first part of this chapter delineates in detail the experimentally observed mechanical response of a rock discontinuity subjected to normal and shear loading. Then, different factors which affect this behaviour are described. Finally, the last part of this chapter introduces existing constitutive models, discussing their formulations, advantages as well as limitations.

2.2 Mechanical behaviour of a single rock discontinuity

This section aims to introduce the main aspects of the mechanical behaviour of a single rock discontinuity, including the stress-strain response under normal loading (perpendicular to the discontinuity plane) as well as shear loading (parallel to the discontinuity plane).

2.2.1 Behaviour under normal stress

A non-linear trend governs the relationship between a discontinuity's normal stress-normal deformation behaviour. At low normal stress, two rough joint surfaces are only in contact at a few contact points. However, during the increment of the applied normal stress the number of contact points is increased. According to Goodman (1976), the non-linear behaviour of a discontinuity is observed because the increment of the normal stress leads some contact points to deform elastically while others deform plastically either by crushing or cracking under tension.

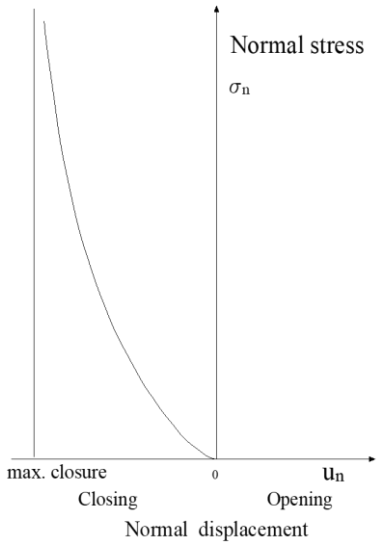

Figure 2.1: Idealised behaviour of discontinuity under normal stress

Figure 2.1, illustrates the idealised behaviour of a discontinuity under normal loading. Goodman (1976) noted two considerations concerning physical constraints on normal deformations. Firstly, an open joint has null tensile strength and secondly, he noted the existence of a limit to the amount of compression which corresponds to the maximum possible closure, $u_{n_{max}}$. This amount of maximum closure (as indicated in Figure 2.1) is represented

mathematically as an asymptote to the non-linear function which described the normal deformation of a discontinuity under the application of normal loading. The non-linear closing behaviour can be described either by a hyperbolic (e.g., Goodman, 1976; Bandis et al., 1983) by a logarithmic (e.g., Brown and Scholtz, 1986; Evans et al., 1992) or by power (e.g., Itasca, 2019) function.

Barton et al., (1983) noted that upon stress loading and unloading of a discontinuity, the hysteresis effect is caused by processes arising from the surface mismatch, sampling disturbances, and crushing of asperities. Furthermore, it was proved by the same author, that upon return to the initial stress level, a considerably large amount of permanent deformation occurs. Subsequent loading cycles produce much steeper curves. Finally, Barton et al. (1983) based on interlocked fractured block samples which were subjected to a sequence of loading/unloading cycles proved that the normal stiffness of discontinuity is not cyclic-dependent. More specifically he showed that almost three cycles are required to obtain a single reproducible stress-deformation curve. Figure 2.2 illustrates the experimental results obtained from a typical test case of cyclic normal loading on a sample of limestone. The non-linear stress-strain behaviour and the hysteresis experienced by the fracture during the cycling loading can be observed.

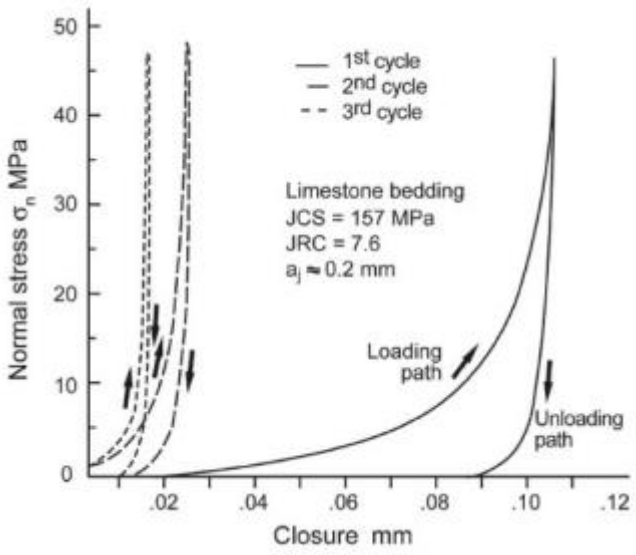

Figure 2.2: Normal stress-closure of fracture sample of limestone under repeated loading cycles

(modified after Barton et al.,1983)

2.2.2 Behaviour under shear stress

It can be stated that the evolution of shear stress, as well as the normal deformation of a discontinuity subjected to shear displacement, are affected by the magnitude of the applied normal stress, the roughness of the two surfaces of the discontinuity and the strength of both rock matrix and infilling material. Commonly, the shear behaviour of a rock discontinuity is investigated in the laboratory under Constant Normal Load conditions (CNL) where the applied normal stress remains constant, and the walls of the discontinuity can dilate freely during the shearing process. In situ, a rock slope where a rock block slides along the existing discontinuity without any constraint is considered the ideal representation of a CNL condition.

On the other hand, in rock engineering practice the applied normal stress on a rock discontinuity may vary during the shearing and the dilation may be constrained by the stiffness of the

surrounding rock. In these cases, the shear behaviour of the rock discontinuity is studied under constant Normal Stiffness Conditions (CNS). This in situ boundary condition is simulated laboratory by using a spring perpendicular to the fracture. Unstable rock blocks in the roof or walls of underground cavity constructions (caverns, mining, tunnels) or reinforced rock wedges sliding in a rock slope or foundation are practical applications in which the shearing of a rock discontinuity is executed under CNS conditions (Leichnitz, 1985; Thirukumaran and Indraratna, 2016).

Figure 2.3 describes schematically both CNL and CNS boundary conditions but also indicates how these in situ conditions are simulated in the laboratory:

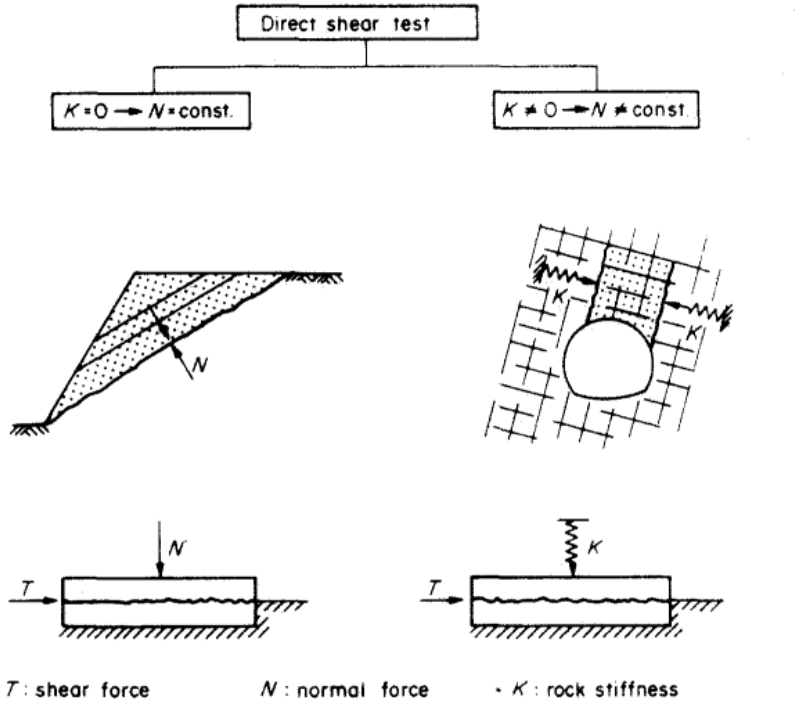

Figure 2.3: Representation of CNL and CNS conditions in situ and laboratory (Leichnitz, W., 1985)

A typical shear stress-shear deformation behaviour of a rough and clean discontinuity that undergoes shearing under CNL conditions is characterized by a relatively rapid increase in shear stress up to a peak τ_{peak} which is observed after a relatively small amount of shear displacement, $u_{s_{peak}}$. This peak of the value of shear stress is followed by a significant loss in load-carrying capacity up to residual value τ_{res} (Figure 2.4, curve A). On the other hand, experimental data that describe the shear stress-shear deformation behaviour of filled discontinuities under the same boundary conditions (Figure 2.4, curve B), denote a more gradual increase of shear stress with a peak shear stress which is poorly defined (Goodman, 1976). In both cases, the slope characterizing the elastic region denotes the value of the shear stiffness k_s.

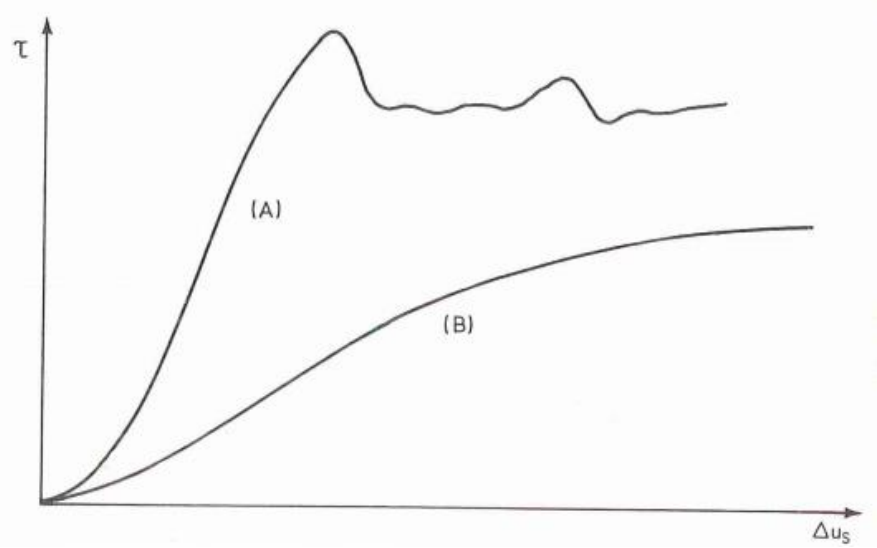

Figure 2.4: Idealised shear stress-shear deformation behaviour of clean (A) and filled (B) discontinuities under CNL conditions (modified after Goodman, 1976)

The shearing behaviour of a rock discontinuity is also accompanied by the mechanism of dilation (normal deformation) which originates from surface roughness. In more detail, the elastic phase of the shear deformation is characterized by a small amount of dilation. Many researchers (Barton et al., 1985; Barton and Choubey, 1977; Goodman, 1976), showed that dilation starts before the shear stress reaches its peak value. Dilation onsets when the asperities start to slide against each other (approximately after an amount of shear displacement which is equal to 1% of the fracture sample length (Barton et al., 1985)).

Figure 2.5 illustrates the experimentally observed mechanical behaviour of discontinuity after the application of shear stress under CNL conditions.

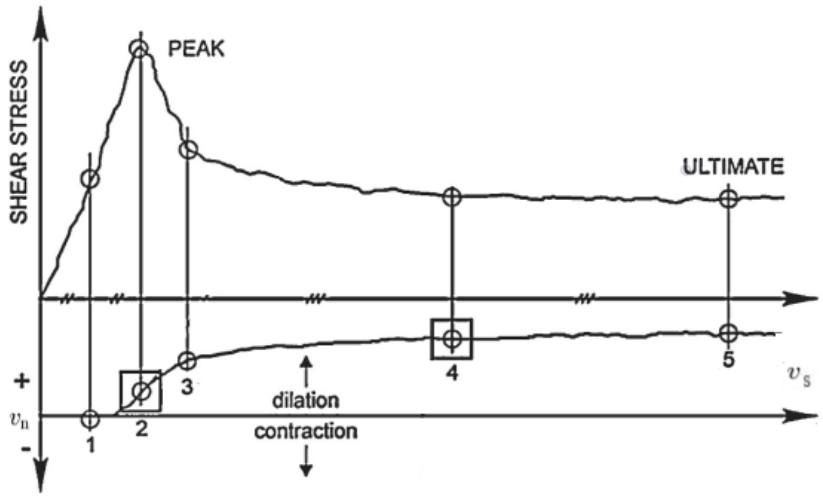

Figure 2.5: Experimentally observed mechanical behaviour of discontinuity under shear stress (modified after Barton, 1976)

Figure 2.6 illustrates the idealized mechanical behaviour of a discontinuity subject to shearing under CNL conditions. In general, it can be observed that the elastic phase of the shear deformation is characterized initially by a small amount of compression while later by a very small amount of dilation. Once the peak shear strength has been reached dilation starts and obtains its maximum value when the shear stress attains its residual value. The rate of dilation is quantitatively described by the tangent of the dilation angle.

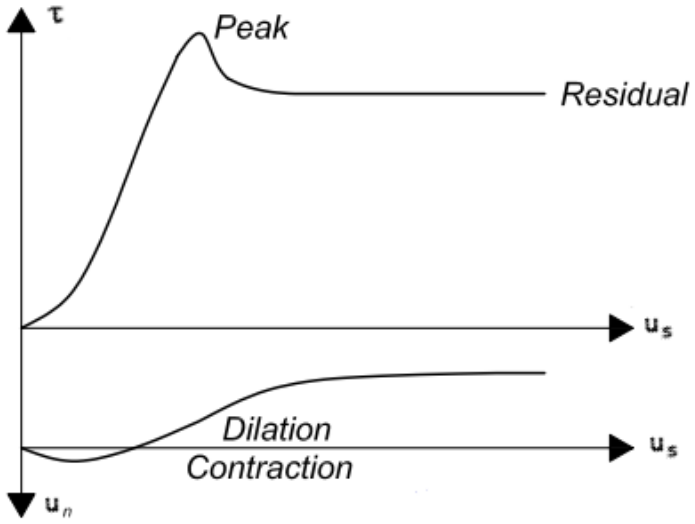

Figure 2.6: Idealised shear behaviour of a rough fracture under CNL condition (after Goodman, 1976)

Barton and Bandis (1982), based on shear tests under CNL conditions indicated that the evolution of shear stress-shear displacement is scale-dependent. It was proven that the shear stiffness reduces with the increase in sample size. On the other hand, they proved that an increase in the applied normal stress during the shearing process leads to a stiffer response of the material.

A typical shear behaviour under CNS conditions is characterized by a steep increase in shear stress (Figure 2.7). With the further application of shear displacement, the rate of the evolution of shear stress becomes lower until a constant value of shear stress is obtained. The higher value of the applied normal stress leads to the highest shear stiffness (Goodman, 1976). Finally, the shearing of fracture under CNS conditions leads to lower values of normal displacement (dilation).

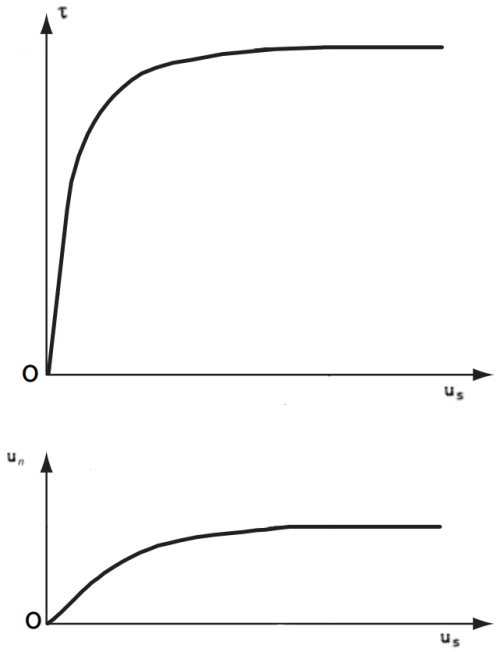

Figure 2.7: Shear behaviour of rough discontinuity under CNS conditions (modified after Jing and Stephansson, 2007)

Experimental results reported by Bandis et al. (1983) denoted that the shear strength of a discontinuity is increased with the increment of the applied normal stress. In more detail, Barton (1976) indicated that, at a low level of effective normal stress, the frictional strength of a joint can be related to the strength of the intact rock by means of the unconfined compression strength. On the other hand, under high effective normal stress, the frictional strength of a joint can be related to the strength of the intact rock by means of the confined compression strength which is expressed by the differential stress ($\sigma_1 - \sigma_3$). Finally, under very high normal stress levels it was observed that the stress required to fracture the intact rock in non greater than the shear strength of the resulting discontinuity.

2.3 Properties of discontinuities which control their mechanical behaviour

When a fractured rock mass is subjected to mechanical loads both the intact rock and rock discontinuities will deform. However, most of the deformation occurs in discontinuities (Fardin, 2003). A discontinuity or rock fracture consists of two rock surfaces with irregular shapes which are in contact in randomly distributed zones along their length. The existing volume of the void between the two surfaces could be either filled or not (Hakami, 1995).

In particular, the mechanical behaviour of a discontinuity (strength and stress-strain relationship) depends on several parameters (e.g., Patton, 1966; Goodman, 1976; Barton et al., 1985; Saeb and Amadei, 1992; Grasselli and Egger, 2003). Figure 2.8, illustrates the main properties of rock discontinuities which control their mechanical response.

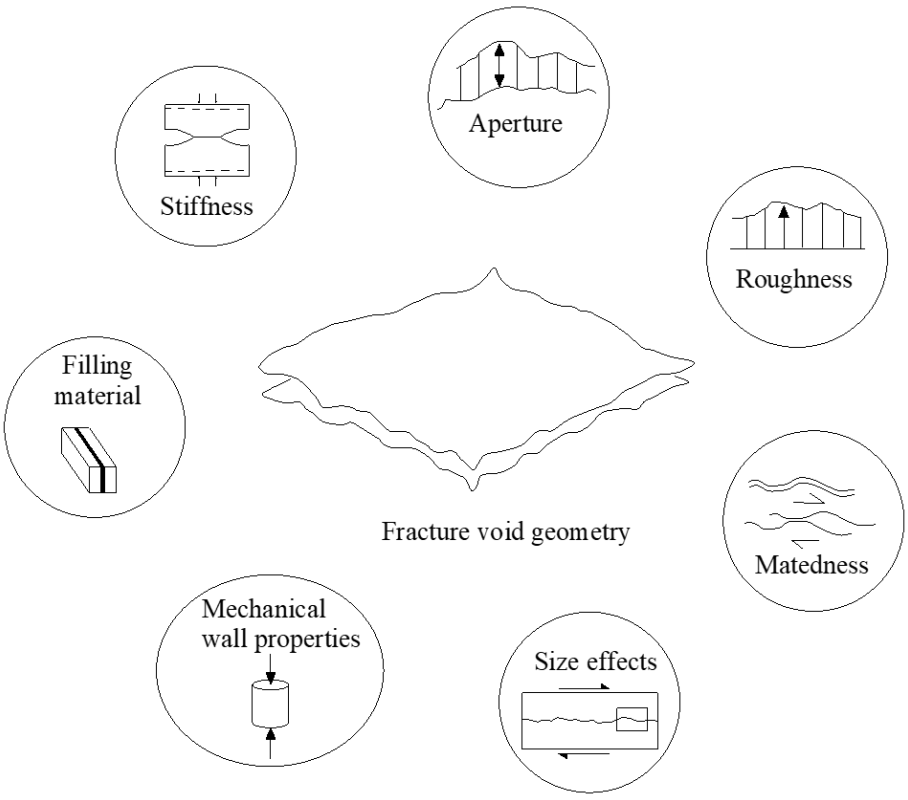

Figure 2.8: Features of discontinuities which control their mechanical behaviour (modified after Hakami, 1995)

A brief description of the properties depicted in Figure 2.8 follows.

2.3.1 Aperture

According to the International Society of Rock Mechanics (ISRM), the aperture is the perpendicular distance separating the adjacent rock walls of an open discontinuity, in which the intervening space is air or water-filled. More specifically, the displacement of the adjacent rock walls relative to each other and/or the differences in the morphology of the adjacent rock walls are principally the two reasons why the aperture of a discontinuity is not zero. The difference in the morphology of the rock walls of a discontinuity is created mainly by the damaging and crushing of the asperities or by chemical processes like mineral precipitation and dissolution.

The aperture can be determined either through the analysis of the profiles of the rock surfaces; or by filling the void space with casting material. Furthermore, the distribution of the aperture is only valid at a certain state of stress and if the stress changes the distribution will be altered (Hakami, 1995). More specifically, at a given stress state the value of the aperture (mechanical aperture, e_m) is related to the mechanical parameters of a discontinuity. From this aspect, the mechanical aperture is calculated by subtracting the measured value of closure from the value of maximum closure:

$$e_m = u_{n_{max}} - u_n \tag{2.1}$$

where u_n renders the measured value of closure which describes the normal relative displacement of the discontinuity walls, while $u_{n_{max}}$ indicates the maximum closure. In more detail, the maximum closure defines the closure corresponding to normal stress beyond which no further normal deformation in excess with respect to one of the intact rock is observed (Cammarata, 2005).

2.3.2 Roughness

All natural discontinuity surfaces exhibit some degree of roughness, varying from relatively smooth surfaces with very low roughness to rough and irregular tension joints with a considerable degree of roughness (Wyllie and Mah, 2004).

The measurement of the roughness can be accomplished using a simple mechanical profilometer. Using the profilometer, rock engineers can acquire the surface morphology of natural discontinuities. In engineering practice, it is accepted to give the parameter an empirical number in some way irrespective of its real physical meaning and relate this number with the relevant mechanical parameter.

In this context, Barton and Choubey (1977) reported the JRC (Joint Roughness Coefficient) coefficient through which the roughness of a discontinuity can be quantified. Based on a large number of shear tests on natural discontinuities the authors proposed ten standard roughness profiles that provide typical JRC values (Figure 2.9). The introduced scale varies from 0, which indicates smooth discontinuity, to 20 which denotes rough discontinuities. The importance of the parameter JRC for the normal deformation and shearing analysis of discontinuities is highlighted by Barton who introduced the well-known strength criterion based on the concept of mobilized roughness (Barton et al., 1985). This concept indicates that the shear strength of a discontinuity and the occurred dilation during the shearing process are highly controlled by the roughness of the discontinuity walls.

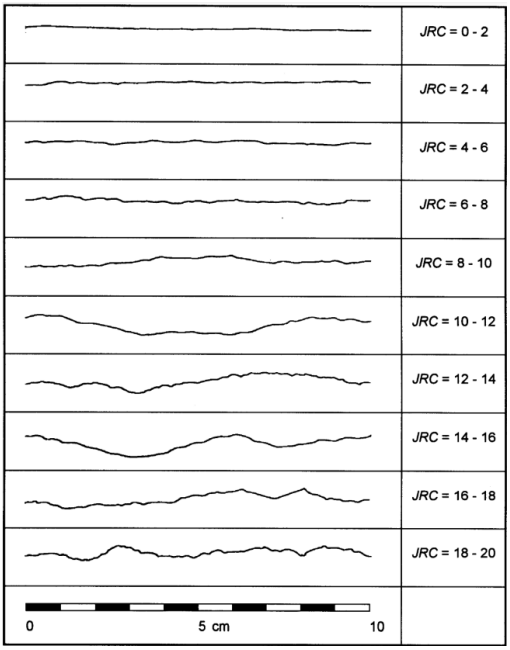

Figure 2.9: Roughness profiles and corresponding JRC values (Barton and Choubey 1977)

2.3.3 Matedness

According to Hakami (1995), the term matedness is used to describe the general match between the two opposing discontinuity surfaces. Mated discontinuities have different properties compared to unmated ones. In more detail, the mated discontinuities are stronger and stiffer than the unmated discontinuities while the permeability of the unmated discontinuities is significantly higher than the permeability of the mated ones.

2.3.4 Size Effects (length)

According to Pratt et al. (1972), an important consideration for the determination of the mechanical properties of jointed rock is the effect of specimen size on strength and deformation characteristics. Based on the extensive investigation of Pratt, Barton and Choubey (1977) and Barton et al. (1985) continued the research work and proved that the mechanical behaviour of a discontinuity subjected to shearing is significantly affected by the size of the examined sample. More specifically, Barton et al. (1985) stated that the shear stiffness is the parameter affected most, due to the simultaneous reduction of shear strength and increase of peak shear displacement as the dimensions of the discontinuity are increased. In the context of discontinuity modelling, the increment of discontinuity size causes notable reductions in JRC and JCS parameters and leads to the increment of the shear displacement required for the peak shear strength to be reached.

2.3.5 Mechanical wall properties

The strength of the discontinuity rock walls may significantly differ from the strength of the surrounding intact rock. The properties of rock walls are commonly estimated through the Joint wall Compressive Strength (JCS) coefficient which was introduced by Barton (1973).

The values of this fundamentally important parameter are obtained by conventional unconfined compression tests on intact cylinders or from point load tests on rock cores. In engineering practice, this parameter is also measured using the Schmidt hammer test which consists of a

spring released when the plunger is pressed against a surface. The impact of the piston onto the plunger transfers energy to the material (ISRM, 2007).

According to Barton (1976), the values of the JCS are closely dependent on the weathering conditions of the discontinuity. Unweathered discontinuities provide the rock engineers with significantly higher JCS values in comparison with the weathered ones. Furthermore, Barton (1976), after conducting a series of shear tests in fractured rock blocks with different morphological and mechanical properties, stated that the value of the JCS parameter in rough discontinuities is crucial when the applied stress levels are low (as in most rock engineering projects). On the other hand, he noted that discontinuities with lower degrees of roughness are progressively less affected by the value of JCS.

2.3.6 Filling material

In rough discontinuities where no filling material exists between the rock walls of a discontinuity, the derivation of shear strength is controlled entirely by the friction angle of the rock material. However, it is common in the field that the discontinuities contain an infilling which affects their mechanical behaviour.

According to Goodman (1970), the effect of infilling on shear strength depends on both the thickness and strength properties of the filling material. In more detail, if the thickness of the filling material covers more than 25-50% of the thickness of the discontinuity, then the shear strength is dictated by the properties of the infilling. Therefore, in engineering practice, it is of high importance to identify and assess the filling material (if it exists) as it is a factor with a significant effect on the stability of rock engineering structures.

2.3.7 Stiffness

The deformability of a discontinuity subjected to mechanical loading is controlled by its normal k_n and shear k_s stiffness (Goodman, 1968). Normal stiffness k_n, was defined to describe the rate of change of normal stress σ_n with respect to normal displacement (closure) u_n. On the other hand, with the definition of shear stiffness k_s, the rate of change of shear stress τ with respect to shear displacement u_s is described. A schematic representation of the stiffness components is given in Figure 2.9.

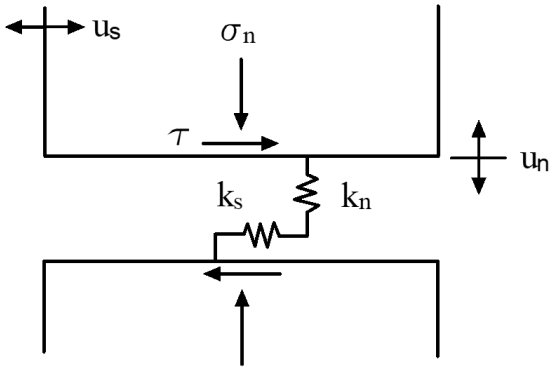

Figure 2.9: Schematic representation of normal stiffness k_n, shear stiffness k_s (modified after Olsson, 1998)

2.4 Constitutive Models of rock discontinuities

This section aims to introduce some of the most well-known constitutive models in the field of discontinuity modelling found in the literature. A constitutive model is considered a complete

model which can be used to simulate the mechanical behaviour of a discontinuity when it clearly defines the formulation of the strength criterion based on which the shear strength of a discontinuity is calculated, as well as the formulations of both normal and shear stiffness which control the evolution of stress-deformation relationship under normal and shear loading respectively. Therefore, the selected constitutive models will be described by highlighting the formulation of these three main components and by mentioning their main advantages and limitations. Note that in this chapter, normal stress is conventionally positive in compression.

2.4.1 Coulomb's model

The most well-known and simplest model to simulate the mechanical behaviour of a discontinuity is Coulomb's model. The considered model uses Coulomb's strength criterion, one of the simplest linear shear failure criteria through which the peak shear strength of a rock fracture can be determined. The failure envelope of this criterion is expressed as follows:

$$\tau_{peak} = c + \sigma_n' tan\varphi_{peak} \tag{2.2}$$

where c is the cohesion, σ_n' denotes the effective normal while the φ_{peak} indicates the value of friction angle at peak shear stress.
When the peak shear strength is exceeded, the shear strength reaches its residual value which is calculated by replacing in Equation (2.2) c and φ_{peak} with their residual values, c_{res} and φ_{res} respectively:

$$\tau_{res} = c_{res} + \sigma_n' tan\varphi_{res} \tag{2.3}$$

Discontinuities often have very small or nil tensile strength σ_T, namely the normal stress is bounded to $\sigma_n' > -\sigma_T$. Figure 2.10 illustrates Coulomb's shear failure criterion.

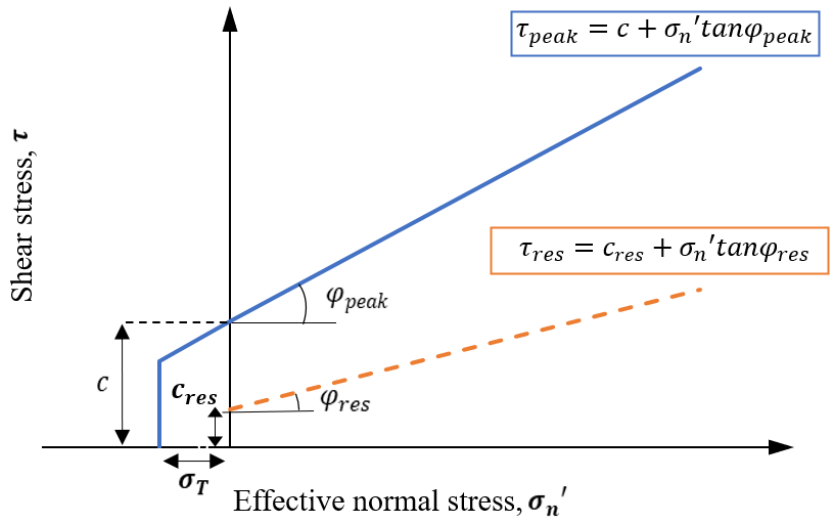

Figure 2.10: Coulomb's shear failure criterion

Due to its simplicity, this model has been widely used for practical engineering applications, generally associated with constant values for both the normal and shear stiffnesses. Furthermore, the shear behaviour of discontinuities at very high levels of normal stress (under which the asperities of the discontinuity walls are sheared-off) or at very low stresses can be captured with adequate accuracy adopting Coulomb's model considering that the friction angle is constant at the examined stress range. In rock engineering applications where no significant

fluctuations of the applied normal stress levels are expected the friction angle is also considered as constant. Therefore, Coulomb's model despite its simplicity and its weakness which lies in that it overestimates the shear strength at low stresses, (Fardin, 2003), can provide rock engineers with reliable results when the expected stress range is considered and the friction angle in this range is constant.

Improvements for the simulations of the discontinuity behaviour through Coulmb's model have been also proposed through the use of non-linear functions for the stiffnesses. An example is the Non-linear joint model by Itasca (2019) where power-law functions are employed. These simple mathematical functions are in fact the first empirical formulations carried out from the early investigation by several authors (Nassir, 2013).

Another example of the improvement in the adoption of the Coulomb model is the use of peak/residual behaviour through either a brittle behaviour (e.g. Bentley, 2023) or linear softening behaviour (e.g. Itasca, 2019).

The simple linear formulation of this strength criterion in combination with the small number of the required and easy-to-determine parameters, render it applicable in practice and one of the most well-known shear failure criteria.

2.4.2 Goodman's model

Goodman (1976) introduced the first comprehensive constitutive model for the description of the evolution of stress and deformation characteristics of discontinuities. Goodman's model is an empirical approach for 2D fractures which has been formulated in total stresses and displacements, based on experimental data of shear tests under constant normal stress conditions conducted on rock discontinuities (Jing and Stephansson, 2007).

Goodman based his constitutive model on the strength criterion suggested by Ladanyi and Archambault (1969). In more detail, Ladanyi and Archambault (1969) developed a peak shear strength criterion for rock fractures by combining the contributions of friction, roughness and shearing through the asperities. The peak shear strength is defined by the following equation:

$$\tau_{peak} = \frac{\sigma_n(1 - a_s)\left(\dot{u}_n + \tan(\varphi_\mu)\right) + a_s s_R}{1 - (1 - a_s)\dot{u}_n + \tan(\varphi_f)} \tag{2.4}$$

where a_s is the proportion of the joint area sheared through the asperities, $\dot{u}_n$ indicates the rate of dilation at failure (secant dilatancy rate), φ_μ renders the friction angle of smooth surfaces without any asperities (as introduced by Patton, 1966), φ_f is the statistical mean friction angle when sliding occurs along the asperities and s_R denotes the shear strength of the rock composing the asperities which can be evaluated with the following formulation:

$$s_R = q_u \frac{\sqrt{1+n} - 1}{n} \left(1 + n\, \sigma_n / q_u\right)^{1/2} \tag{2.5}$$

where q_u is the unconfined compressive strength (σ_c) and n is the ratio of compressive to the tensile strength, of the rock comprising the asperities.

Furthermore, the difficulties in determining the remaining parameters of the criterion led to the following empirical relations (Ladanyi & Archambault, 1980):

$$a_s = 1 - \left(\frac{1 - \sigma_n}{\eta\sigma_t}\right)^L \tag{2.6}$$

$$\dot{u}_n = \left(1 - \frac{\sigma_n}{\eta\sigma_t}\right)^K \tan(i) \tag{2.7}$$

where σ_t is the transition pressure which can be further described as the normal stress at which the fracture ceases to be weaker than the rock itself and in the absence of sufficient data can be considered equal to the unconfined compressive strength. The terms L and K are dimensionless constants and their values were suggested by Ladanyi and Archambault (1969). More specifically, the suggested values of these parameters are 1.5 and 4 respectively. Furthermore, i denotes the average inclination of the intact irregularities (as introduced by Patton, 1966). Finally, the parameter η is called the degree of interlocking and is defined by the same authors as follows:

$$\eta = 1 - \frac{1 - \Delta_x}{\Delta_L} \tag{2.8}$$

where Δ_x denotes the shear displacement along the ascending asperity while L indicates the projection of the ascending part of the asperities (Figure 2.11):

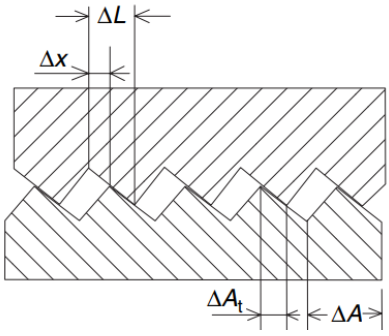

Figure 2.11: Definition of the interlocking term (modified after Ladanyi and Archambault, 1969)

In conclusion, Ladanyi and Archambault's strength criterion through its parameters and especially through a_s and $\dot{u}_n$ represents the effect of roughness of the discontinuities. During the deformation process the roughness of the discontinuity can only be decreased due to the accumulated damage of the asperities. However, the formulation of a_s and $\dot{u}_n$ proposed by the authors in Equations (2.7) and (2.8), denotes that the value of these two terms is reversible with respect to the normal stress. Thus, the introduced strength criterion is more suitable for discontinuities which are subjected to shear displacement under constant or monotonically increasing normal stress (Jing and Stephansson, 2007).

In addition, Goodman's model captures the non-linear closing behaviour by adopting a hyperbolic. In more detail, Goodman (1976) introduced his hyperbolic function based on two considerations concerning physical constraints on normal deformations (as stated also in Section 2.2.1). Firstly, an open joint has null tensile strength and secondly, he noted that there is a limit to the amount of compression which corresponds to the maximum possible closure, $u_{n_{max}}$. Based on experimental testing of an artificially created fracture in granodiorite sample, Goodman (1976) derived the following empirical relation for both mated and unmated discontinuities:

$$\frac{\sigma_n - \sigma_{n_{ini}}}{\sigma_{ni}} = A\left(\frac{u_n}{u_{n_{max}} - u_n}\right)^t \tag{2.9}$$

where $\sigma_{n_{ini}}$ denotes the normal stress at the initial reference stage while A and t are empirical constants.

Derivation of Equation (2.3) leads to the expression of normal stiffness k_n as follows:

$$k_n = \frac{t(\sigma_n - \sigma_{n_{ini}})}{u_{n_{max}}\left(1 - \frac{u_n}{u_{n_{max}}}\right)} \tag{2.10}$$

The model assumes a zero normal stiffness when the initial normal stress is zero.

The last property which is used from Goodman's model to describe the mechanical behaviour of a discontinuity and especially the evolution of the shear stress-shear deformation relationship is the shear stiffness k_s. Goodman (1976) introduced two models which can be adopted during the study of the mechanical behaviour of a discontinuity under shearing. The first model considers the shear stiffness constant (Figure 2.12, graph a) while the second one considers the shear stiffness as a function of the shear strength τ_{peak} and the amount of the shear displacement which is required to reach the peak shear strength, $u_{s_{peak}}$ (Figure *2.12*, graph b) In this case, the value of shear stiffness is calculated as follows:

$$k_s = \frac{\tau_{peak}}{u_{s_{peak}}} \tag{2.11}$$

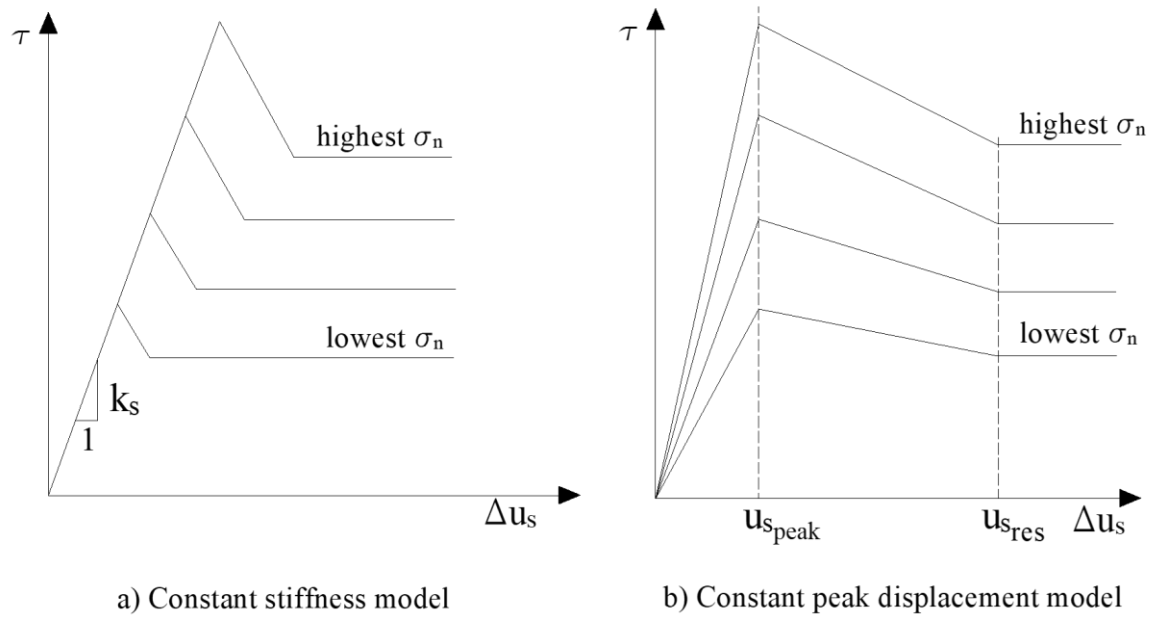

Figure 2.12: Shear deformations models (modified after Goodman 1976)

Goodman based on the above-introduced formulations of the shear strength criterion of Ladanyi and Archambault (1970) and shear stiffness, formulate the following constitutive relationships that describe the mechanical behaviour of a discontinuity subjecting to shearing:

I) $$\tau = -\tau_{res}, \quad for \ u_s \leq u_s^{res(-)} \tag{2.12}$$

II) $\tau = -\tau_{peak} + \frac{\tau_{peak}-\tau_{res}}{u_{s_{peak}}-u_{s_{res}}} u_s - u_{s_{peak(-)}},\ for\ u_{s_{res(-)}} < u_s < u_{s_{peak(-)}}$ (2.13)

III) $\tau = k_s u_s + \tau_o,\ for\ u_{s_{peak(-)}} < u_s < u_{s_{peak(+)}}$ (2.14)

IV) $\tau = -\tau_{peak} + \frac{\tau_{peak}-\tau_{res}}{u_{s_{peak}}-u_{s_{res}}} u_s - u_{s_{peak(+)}},\ for\ u_{s_{peak(+)}} < u_s < u_{s_{res(+)}}$ (2.15)

V) $\tau = -\tau_{res},\ \ for\ u_s \geq u_{s_{res(+)}}$ (2.16)

where τ_o is the initial shear stress, $u_s^{peak(-)}$ and $u_s^{peak(+)}$denote the shear displacements which correspond to the peak shear stress and $u_s^{res(-)}$ and $u_s^{res(+)}$ indicate the shear displacement which corresponds to the residual shear stress. The values of residual and peak shear displacement are determined based on the formulations suggested by Goodman (1976):

$$u_{s_{peak(+)}} = u_{s_{peak}} = \frac{\tau_{peak} - \tau_o}{k_s} \quad (2.17)$$

$$u_{s_{res(+)}} = u_{s_{res}} = \frac{M(\tau_{peak} - \tau_o)}{k_s} \quad (2.18)$$

$$u_{s_{peak(-)}} = -u_{s_{peak}} - \frac{2\tau_o}{k_s} \quad (2.19)$$

$$u_{s_{res(-)}} = -u_{s_{res}} \frac{2\tau_o}{k_s} \quad (2.20)$$

Figure 2.13 illustrates the piecewise linear formulation of the stress-strain relationship in the shear direction based on the constitutive formulations proposed by Goodman:

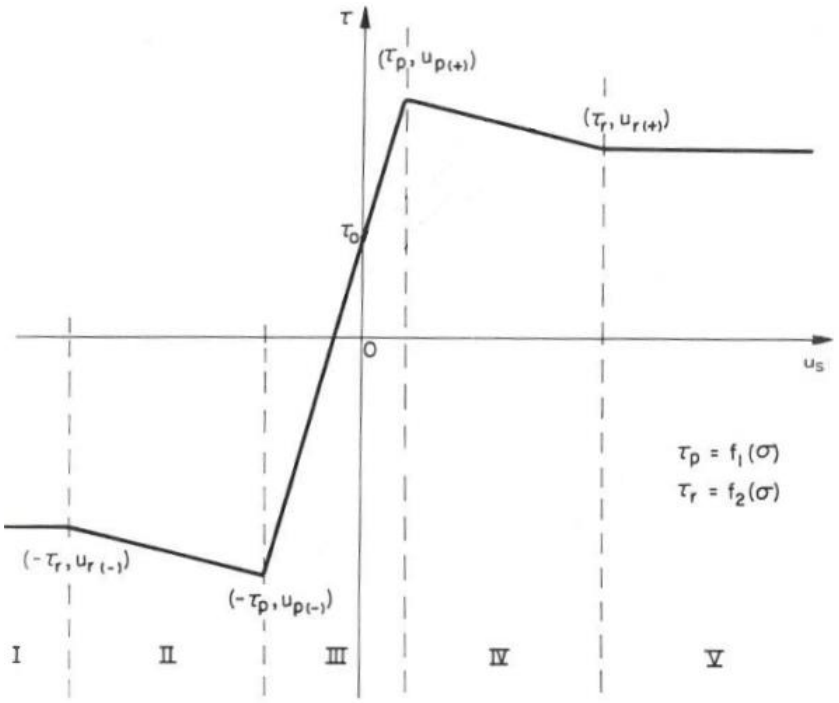

Figure 2.13: Goodman's constitutive law for shear deformation (modified after, Goodman 1976)

Furthermore, Goodman (1976) introduced the following formulations to capture the occurred increment of normal displacement (dilatancy) during the shearing (Jing and Stephansson, 2007):

$$du_n = -\frac{d_{peak}}{u_{s_{peak}}}\left(|u_s| - \left|\frac{\tau_o}{k_s}\right|\right), for\ \ u_s^{res(-)} < u_s < u_s^{res(+)} \tag{2.21}$$

$$du_n = -\frac{d_{peak}}{u_{s_{peak}}}\left(u_s^{res(+)} + \left|\frac{\tau_o}{k_s}\right|\right), for\ \ u_s \geq u_s^{res} \tag{2.22}$$

where d_{peak} is the dilatancy of the fracture at u_s^{peak}.

Goodman's model was a pioneer constitutive law that can represent the post-peak softening phenomenon (but in a simplified way). Moreover, this model in contrast to the simple elastoplastic models can capture that dilation occurs much earlier before shear displacement reaches the peak shear displacement. However, it must be noted that in contrast to the experimental results discussed in Section 2.2.2 that denote that dilation onsets approximately after an amount of shear displacement which is equal to 1% of the discontinuity length this model considers that dilation starts once the shearing process begins.

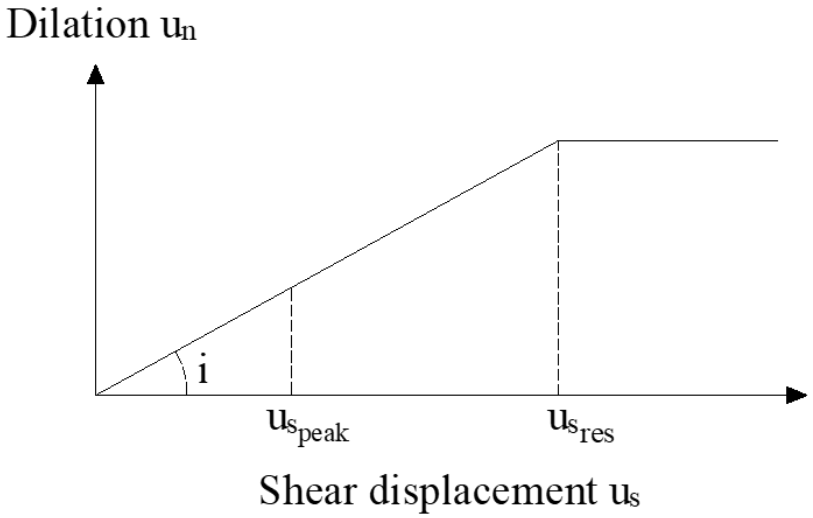

Figure 2.14: Idealised shear displacement vs normal displacement evolution according to Goodman's model (1976)

Furthermore, important factors for the adequate description of the mechanical behaviour of discontinuities such as scale surface roughness and cyclic shear paths are not considered.

2.4.3 Barton-Bandis model

The Barton-Bandis model is an empirical model for rock fractures which was first introduced in 1981. Since then, the Barton-Bandis model has been well-tested against extensive laboratory measurements of different rock types and fracture types.

The peak shear strength in the Barton-Bandis model is calculated based on the well-known shear strength criterion (e.g. Barton, 1976; Barton and Choubey, 1977; Bandis et al., 1983; Barton et al., 1985). Barton introduced his strength criterion based on experimental results on artificial, rough discontinuities and has the same general form as Patton's criterion. More specifically, Patton (1966) was the first researcher who tried to correlate the shear strength of a discontinuity with the roughness of the surface. The author conducted several shear tests on "saw-tooth" fractured replicas assuming that the asperities on the fracture surface have identical

shapes and angles of inclination i. Patton (1966) based on these tests developed his bi-linear strength criterion shown in Figure 2.15.

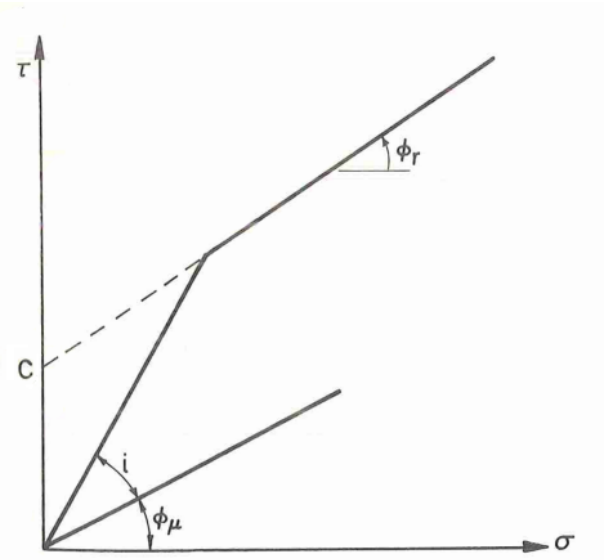

Figure 2.15: Patton's bi-linear failure envelope (Goodman, 1976)

By assuming that the asperities slide on each other at low normal stress, the strength criterion is formulated as follows:

$$\tau_{peak} = \sigma_n \tan(\varphi_\mu + i) \tag{2.23}$$

where φ_μ renders the friction angle of smooth surfaces without any asperities and i is the angle of inclination of the failure surface which in this case is equivalent to the dilation angle (Fardin, 2003). The value of i is determined as the statistical mean of the angles between the mean smooth reference surface and the first-order roughness along the whole fracture (Jing and Stephansson, 2007).

By increasing the applied normal stress, it is assumed that the asperities are sheared off and the dilatancy is constrained. Under this high value of normal stress, the strength is rewritten as follows:

$$\tau_{peak} = c + \sigma_n \tan(\varphi_r) \tag{2.24}$$

where c and φ_r denote the cohesion and the residual friction angle respectively.

The arduous calculation of the asperity angle in combination with the fact that Patton's criterion "overlooks" the scale effect and the roughness evolution/mobilisation during the deformation process summarise the main limitations of this peak shear strength criterion. However, despite its simplicity, this criterion is considered a conceptual breakthrough.

Having introduced briefly the Patton's shear strength criterion it can be noted that the main difference in the formulations of Patton's criterion in comparison with Barton's law is that the constant value of the dilation angle i in Patton's bilinear law is replaced by the following relation which denotes that in Barton's criterion the dilation angle varies as a function of the applied normal stress:

$$i = \log\left(\frac{JCS}{\sigma_n}\right) JRC \tag{2.25}$$

Thus, Barton's strength criterion is expressed as follows:

$$\tau_{peak} = \sigma_n \tan\left(JRC_{peak}\log_{10}\left(\frac{JCS}{\sigma_n}\right) + \varphi_r\right) \tag{2.26}$$

where τ_{peak} is the shear strength of the discontinuity, σ_n is the applied normal stress, φ_r is the residual friction angle while JRC is the peak value of roughness coefficient and JCS the joint wall compressive strength described in Sections 2.3.2 and 2.3.5 respectively. At peak shear stress the terms inside the brackets of the tangent correspond to the value of the peak friction angle:

$$\varphi_{peak} = JRC_{peak}\log_{10}\left(\frac{JCS}{\sigma_n}\right) + \varphi_r \tag{2.27}$$

According to Barton et al. (1985), peak shear strength is reached after the subjection of the fracture on a small shear displacement denoted by δ_{peak}. Barton and Bandis indicated that for the case of laboratory-size samples, the peak shear strength is reached when a shear displacement equal to 1% of the sample's length has been applied. In more detail, based on the obtained experimental results after 650 shear tests, they developed an empirical equation for the estimation of δ_{peak}:

$$\delta_{peak} = \frac{L_n}{500}\left[\frac{JRC_n}{L_n}\right]^{0.33} \tag{2.28}$$

The introduced parameters JRC and JCS are scale dependent. Therefore, Barton et al. (1985) proposed the following relations to determine their large-scale value using laboratory tests on small samples:

$$JRC_n = JRC_0\left(\frac{L_n}{L_0}\right)^{-0.02JRC_0} \tag{2.29}$$

$$JCS_n = JCS_0\left(\frac{L_n}{L_0}\right)^{-0.03JRC_0} \tag{2.30}$$

where JRC_n is the value of JRC for the field scale and JRC_0 is the value of JRC for the laboratory scale. Accordingly, JCS_n is the value of JCS for the field scale and JCS_0 is the value of JCS for the laboratory scale. Finally, L_n is the field scale of the examined fracture while L_o is the laboratory scale which according to Barton et al. (1985) the nominal length of a laboratory sample is equal to 100 mm.

It can be seen, that at a low stress level when the normal stress approaches zero, Equation (2.26) loses its meaning. According to Barton, the strength envelop is linearized when the secant friction angle (Equation 2.27) is higher than 70°. This means the friction angle is limited to 70°. On the other hand, Equation (2.26) also loses its meaning when the normal stress reaches JCS.

Barton and Choubey (1977) developed an empirical relation to estimate the value of residual friction angle based on the value of basic friction angle using the Schmidt hammer test. The hammer tests were executed on both unweathered, dry rock (rebound R) and on weathered saturated joint walls (rebound r) (Barton, 1985).

$$\varphi_r = (\varphi_b - 20) + 20\frac{r}{R} \tag{2.31}$$

Later, Barton (2013) reformulated the empirical relation for the calculation of residual friction angle as follows:

$$\varphi_r = (\varphi_b - 20) + 20\frac{JCS_0}{\sigma_c} \tag{2.32}$$

where σ_c is the uniaxial unconfined strength.

After the introduction of the strength criterion which is adopted by the Barton-Bandis model, the next important component of this model which must be defined is the formulation of normal stiffness. This constitutive model uses a hyperbolic function to describe the non-linear closing behaviour of a discontinuity subjected to normal stress. More specifically, Bandis et al. (1983), based on 65 interlocked jointed block samples which were subjected to a sequence of loading/unloading cycles, derived the following empirical formulations for the calculation of normal displacement u_n, and normal stiffness k_n:

$$u_n = \frac{\sigma_n u_{n_{max}}}{k_{n_{ini}} u_{n_{max}} + \sigma_n} \tag{2.33}$$

$$k_n = k_{n_{ini}}(1 - \frac{\sigma_n}{u_{n_{max}} k_{n_{ini}} - \sigma_n})^{-2} \tag{2.34}$$

where $k_{n_{ini}}$ is the initial normal stiffness, $u_{n_{max}}$ denotes the maximum amount of normal displacement that a discontinuity can sustain while σ_n indicates the applied stress level. Furthermore, in contrast to Goodman's model, this model assumes a non-zero normal stiffness when the normal displacement is nil.

As far as the shear stiffness is concerned, the authors of the model suggested adopting hyperbolic functions such as those derived by Kulhawy (1975):

$$k_s = k_j(\sigma_n)^{n_j}\left(1 - \frac{\tau R_f}{\tau_{peak}}\right)^2 \tag{2.35}$$

where k_j is the stiffness number while n_j denotes stiffness exponent and R_f is the failure ratio.

The Barton-Bandis model can capture a wide range of fracture closing behaviour including stiff fractures (whose stiffness has a high initial value and slowly increases with the increment of the applied normal stress) but also fractures that are highly compressible in low normal stress regimes but become very stiff when the value of the occurred closure is close to the value of max closure $u_{n_{max}}$ (compliant fractures).

The Barton-Bandis model describes the shear stress-shear displacement behaviour of fracture based on the concept of "mobilized roughness". In this way, this constitutive model can capture the displacement-dependent non-linear evolution of shear strength of a discontinuity during both pre- and post-peak shear phases. More specifically, at any given shear displacement, the calculation of the shear stress is calculated as follows:

$$\tau = \sigma_n \tan\left(JRC_{mob}\log_{10}\left(\frac{JCS_{mob}}{\sigma_n}\right) + \varphi_r\right) \tag{2.36}$$

where:

$$\varphi_{mob} = \left(JRC_{mob}\log_{10}\left(\frac{JCS_{mob}}{\sigma_n}\right) + \varphi_r\right) \tag{2.37}$$

In the formulation of mobilized friction angle Equation (2.37), JRC_{mob} the mobilized roughness coefficient of the fracture at the corresponding shear displacement, JCS_{mob} the mobilized uniaxial compressive strength of the rock material.

Barton et al. based on the concept of mobilized roughness used two dimensionless coordinates to facilitate the simulation of shear stress-shear displacement behaviour. These two coordinates are expressed as follows:

$$\frac{JRC_{mob}}{JRC_{peak}} = \frac{\varphi_{mob} - \varphi_r}{i_B} \tag{2.38}$$

where i_B according to Barton et al. (1985) is calculated as follows:

$$i_B = JRC_{peak}\log\left(\frac{JCS}{\sigma_n}\right) \tag{2.39}$$

the whole shear stress-shear displacement behaviour is divided into five key aspects (Barton et al. 1985):

1. The beginning of shearing is accompanied by the mobilisation of friction

2. Dilation occurs once the mobilisation of roughness begins. According to Barton, during the shearing of a rock discontinuity, recoverable strains are generated until the amount of the applied displacement becomes equal to 30% of the total amount of shearing. From this point and after the mobilisation of roughness begins and the phenomenon of dilations is observed. The calculation of generated dilation is calculated as follows:

$$du_n = \frac{1}{2}JRC_{mob}\log\left(\frac{JCS}{\sigma_n}\right) \tag{2.40}$$

3. Peak shear strength is reached a JRC_{mob}/JRC_{peak}=1 and δ/δ_{peak}=1. At peak shear displacement the dilatancy is given as:

$$du_{n_{peak}} = \frac{1}{2}JRC_{peak}\log\left(\frac{JCS}{\sigma_n}\right) \tag{2.41}$$

4. Both shear stress and dilatancy decrease with the further increment of the shear displacement

5. Dilation is eliminated once the residual stress is reached.

Figure 2.16 depicts, the key features that describe the evolution of JRC_{mob} of a rock fracture subjecting to shear displacement:

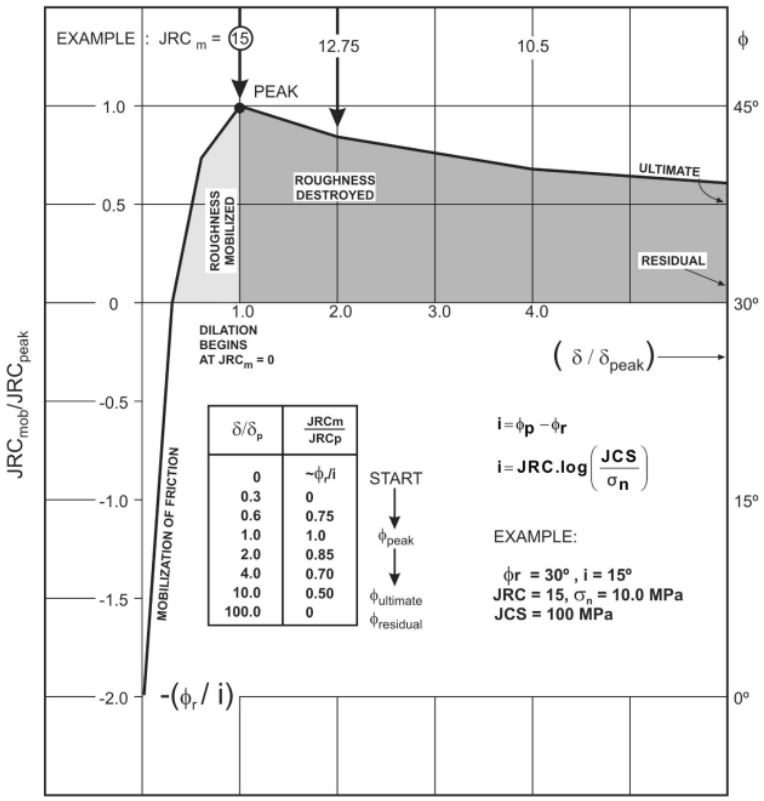

δ/δp	JRCm / JRCp
0	~φr/i
0.3	0
0.6	0.75
1.0	1.0
2.0	0.85
4.0	0.70
10.0	0.50
100.0	0

Figure 2.16: Dimensionless graph illustrating the evolution of JRC_{mob} during the shearing process (Barton et al., 1985)

Furthermore, Barton (1976), based on experimental results obtained after the conduction of direct shear tests on a variety of artificial discontinuities, noted that the shear strength of a discontinuity can be estimated with adequate accuracy under low levels of normal stress (0.08 kPa-0.2kPa) if an appropriate value of the JRC parameter is adopted. In addition, based also on experimental data of shear tests under very low normal stresses (lower than 0.05 kPa) he highlighted that for rough discontinuities a strength envelope having a vertical tangent at/close to the shear stress axis instead of a cohesion (as it is suggested by Coulomb) is inherently satisfying as limiting condition.

In conclusion, the Barton-Bandis model is a physically motivated empirical model for rock discontinuities which has been extensively used for a wide range of rock mechanics applications. Its popularity can be attributed to the fact that it can represent realistically, the mechanical behaviour of a rock fracture as this has been observed in laboratory experiments. More specifically, this model can reproduce the non-linear pre- and post-peak strength and dilation evolution considering the consequences of overriding and damaging the asperities during the shearing process. Moreover, the Barton-Bandis accurately captures the fundamentally essential behaviour which denotes that shear stress reaches its maximum value when the dilation also reaches its peak. Finally, as explained in Section 2.3.3.4 Barton considers the scale effects by estimating the values of JRC and JCS in several scales.

On the other hand, the strong non-linearity of the Barton-Bandis model represents a challenge for implementation in geomechanics simulations due to possible numerical convergence issues (Lei and Barton, 2022). In particular, the mathematical expressions are not valid over the entire stress zone, which makes the numerical implementation very challenging. This will be discussed in more detail in Chapter 3. Furthermore, because it is a highly empirical model some of the parameters which are used are difficult to be determined through standard laboratory

tests. In addition, according to Grasseli and Eager (2003), the estimated values of JRC provided by Barton have been acquired based on the analysis of only a single profile in the direction of shearing whereas it has been shown that shearing strictly depends on three-dimensional contact area location and distribution. Finally, even though the Barton-Bandis model is applied for monotonic shear paths of increasing (or constant) normal stresses with adequate flexibility, it presents theoretical difficulties for complex loading paths due to its empirical nature (Jing and Stephansson, 2007).

2.4.4 Gens's model

Gens et al. (1990), introduced an elastoplastic constitutive law to describe the three-dimensional mechanical behaviour of a rock discontinuity. The main objective of the authors of this constitutive law was to introduce a model for use in numerical analysis that can reproduce the mechanical behaviour of a discontinuity considering also the three-dimensional effects (anisotropy). For this reason, the suggested model was devised with a great degree of flexibility so that it can accommodate easily any observed laboratory or field test results.

Gens et al. (1990) adopted a hyperbolic function for the calculation of peak shear strength. In more detail, they proved that the following hyperbolic function extracts results that fit with sufficient accuracy the shear strength of natural and artificial discontinuities determined in both the laboratory and field:

$$\tau = B\sqrt{{\sigma_n}^2 + 2a\sigma_n} \tag{2.42}$$

where B is a constant which renders the slope of the asymptote when normal stress (σ_n) tends to infinity while a is a constant which denotes the distance between the origin and the point where the asymptote intercepts the axis of normal stress (Figure 2.17).

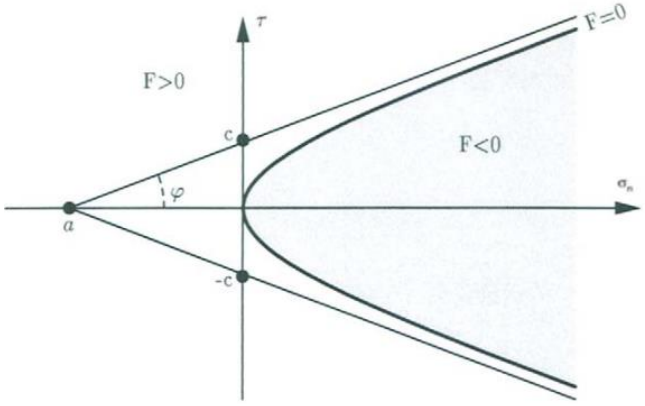

Figure 2.17: Hyperbolic strength criterion adopted in Gens et al. model (modified after Gens et al. 1995)

Furthermore, the normal stress-normal deformation relationship in Gens et al. (1990) model is described through a hyperbolic formulation which is a simplified version of the expression that Goodman suggested:

$$\sigma_n = m\frac{{u_n}^e}{u_{n_{max}} - {u_n}^e} \tag{2.43}$$

where ${u_n}^e$ is the elastic normal deformation while m is a constant. On unloading Equation (2.43) is modified as follows:

$$\sigma_n = m\frac{{u_n}^e - \eta}{u_{n_{m1}} - ({u_n}^e - \eta)} \tag{2.44}$$

Where $u_{n_{m1}}$ is a model parameter ($u_{n_{m1}} < u_{n_{max}}$) and η is the value of the normal displacement reached during the unloading process when the applied normal stress is nil. Upon reloading Equation (2.43) is reformulated as follows:

$$\sigma_n = m\frac{{u_n}^e - \eta}{u_{n_{max}} - {u_n}^e} \tag{2.45}$$

Thus, the value of the normal stiffness at each stage of loading cycles (loading, unloading, reloading) is calculated by differentiating the corresponding equation which describes the normal stress-normal deformation relationship. On the other hand, it must be noted that elastic shear stiffness in this model is considered constant.

Based on these considerations Gens et. al. (1990) introduced their elastoplastic constitutive model. For consistency with the strength criterion that was described by Equation (2.42) the expression of the yield surface is described also by a non-linear hyperbolic (yield) function as follows:

$$F = {\tau_1}^2 + {\tau_2}^2 - tan^2\varphi({\sigma_n}^2 + 2a) \tag{2.46}$$

where τ_1 and τ_2 are the two components of shear stress while a and $tan\varphi$ are the hardening parameters.

The variation of hardening parameters with plastic strains, which denotes the ability of the created model to capture the hardening and softening behaviour of a discontinuity, is controlled by an internal variable ξ which is defined as follows:

$$d\xi = \sqrt{(du_{s_1}^p)^2 + (du_{s_2}^p)^2} \tag{2.47}$$

where $du_{s_1}^p$ and $du_{s_2}^p$ are the two components of plastic shear displacement. Figure 2.18 illustrates the variation of the hardening parameter a with ξ:

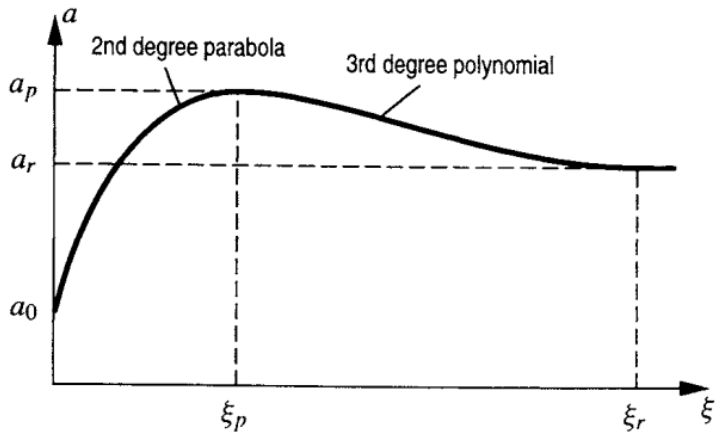

Figure 2.18: Variation of hardening parameter α with ξ

Observing Figure 2.18, it can be noted that the pre-peak variation of the a parameter is described by a second-degree parabola while the post-peak variation is described by a third-degree polynomial. The residual conditions are reached once the internal variable ξ is equal to its residual value (ξ_r). Gens et al. (1990) stated that the value of the second hardening parameter $tan\varphi$ but also the value of the dilation varies with the value of the internal variable ξ adopting the same variation as the variation of a. Regarding the calculation of the peak dilation angle, they introduced the following formulation:

$$tani_{peak} = tani_{peak}^{0}\left(1 - \frac{\sigma_n}{\sigma_c}\right)^4 \tag{2.48}$$

where i_{peak}^{0} is the peak dilation angle for zero applied normal stress

It must be pointed out that the formulation of the yield function corresponds to yield surfaces that are symmetrical with respect to the axis of normal stress (as indicated by Figure 2.17). This condition implies that the model can capture only isotropic because a possible change in the shearing direction will not affect the mechanical behaviour unless it involves a change from loading to unloading (Gens et al., 1990). Further improvement of the introduced model suggested a non-symmetrical formulation of the yield function making the model able to capture the anisotropic behaviour. In more detail, the new formulation of the yield function is written as follows:

$$F = {\tau_s}^2 + \sigma_n(|\sigma_n| + 2\alpha_s) \tag{2.49}$$

where:

$${\tau_s}^2 = \frac{{\tau_1}^2}{tan^2\varphi_1} + \frac{{\tau_2}^2}{tan^2\varphi_2} \tag{2.50}$$

$$\alpha_s = \alpha_1 \frac{{\tau_1}^2}{{\tau_1}^2 + {\tau_2}^2} + \alpha_2 \frac{{\tau_2}^2}{{\tau_1}^2 + {\tau_2}^2} \tag{2.51}$$

the superscripts 1 and 2 correspond to the two components of shear stress.

Concluding, the elastoplastic constitutive law introduced by Gens et al. (1990) can represent with adequate accuracy the three-dimensional mechanical behaviour of a discontinuity. Its ability to model the anisotropic behaviour of a discontinuity in combination with the high degree of flexibility of its formulation so that can accommodate different types of rock discontinuities summarise the main advantages of this model. On the other hand, even though this model is intended for use in numerical analysis, the numerical implementation of the model requires a complex integration procedure to consider all the modes of the behaviour of a discontinuity (Gens et al.,1990).

2.4.5 Saeb and Amadei model

Saeb and Amadei (1992) based on modifications that they did to Goodman's model (1976) (for the evolution of shear stress-shear strain behaviour) and the hyperbolic model of Barton et al. (1985) (for the evolution of normal stress-normal closure behaviour), they introduced a model which accounts not only for the effect of boundary conditions on the shear response of a rough

(dilatant) fracture but also for the fluctuation of its normal deformability as it undergoes shearing.

More specifically, the peak strength of a discontinuity in the developed model is calculated based on a re-examined version of the Ladanyi and Archambault strength criterion suggested by Saeb (1990). The new version of the strength criterion is written as follows:

$$\tau_{peak} = \sigma_n \tan(\varphi_\mu + i)(1 - a_s) + a_s s_R \tag{2.52}$$

The physical meaning and the formulations of the used parameters in Equation (2.52) are the same as the ones introduced in Section (2.4.2).

The Saeb and Amadei model relates the normal stress-strain behaviour of a discontinuity in the normal direction with its shear stress-strain and dilatant behaviour. According to this model, the rock joint deformability is described as a non-linear incremental formulation whose applicability was assessed using the experimental results of Leichnitz (1985):

$$\begin{bmatrix} d\sigma_n \\ d\tau \end{bmatrix} = \begin{bmatrix} k_{nn} & k_{ns} \\ k_{sn} & k_{ss} \end{bmatrix} \begin{bmatrix} du_n \\ du_s \end{bmatrix} \tag{2.53}$$

The (2 x 2) non-symmetrical matrix in Equation (2.53), is the material tangent stiffness. The terms k_{ns} and k_{sn} represent the coupling between the shear and normal strain. Saeb and Amadei introduced formulations for the calculation of all the elements of the stiffness matrix for both constant displacement and constant stiffness models suggested by Goodman(1976) for the description of the evolution of the shear stress-shear deformation relationship. The formulations of both models for the calculation of the stiffness terms are expressed as follows:

For both models the two normal stiffness terms are given from the following formulations:

$$k_{nn} = \frac{\partial \sigma_n}{\partial u_n} = \frac{1}{\frac{-u_s k_2}{\sigma_T}\left(1 - \frac{\sigma_n}{\sigma_T}\right)^{(k_2 - 1)} tani_0 + \frac{{V_m}^2 k_{ni}}{(V_m k_{ni} - \sigma_n)^2}} \tag{2.54}$$

$$k_{ns} = \frac{\partial \sigma_n}{\partial u_s} = \frac{-\left(1 - \frac{\sigma_n}{\sigma_T}\right)^{(k_2 - 1)} tani_0}{\frac{-u k_2}{\sigma_T}\left(1 - \frac{\sigma_n}{\sigma_T}\right)^{(k_2 - 1)} tani_0 + \frac{{V_m}^2 k_{ni}}{(V_m k_{ni} - \sigma_n)^2}} \tag{2.55}$$

Constant displacement model
Main diagonal:

$$k_{ss} = \frac{\partial \tau}{\partial u_s} = \frac{u_s}{u_{s_{peak}}} k_{ns} \frac{\partial \tau_{peak}}{\partial \sigma_n} + \frac{\tau_{peak}}{u_{s_{peak}}}, \text{if } u_s < u_{s_{peak}} \tag{2.56}$$

$$k_{ss} = \frac{\partial \tau}{\partial u_s} = \frac{\tau_{peak} - \tau_{res}}{u_{peak} - u_{res}} \left\{ \frac{\partial \tau_p}{\partial \sigma_n} (u_s - u_{res}) + (u_{peak} - u_s) \left[\frac{\partial \tau_{peak}}{\partial \sigma_n} \left(\text{Bo} + \frac{1 - Bo}{\sigma_t} \sigma_n \right) + \frac{\tau_{peak}}{\sigma_t} (1 - Bo) \right] \right\} \tag{2.57}$$

$$\text{if } u_{s_{peak}} < u_s < u_{s_{res}}$$

$$k_{ss} = \frac{\partial \tau}{\partial u_s} = 0, \text{if } u_s > u_{s_{res}} \tag{2.58}$$

Off-diagonal coupling terms:

$$k_{sn} = \frac{\partial \tau}{\partial u_n} = \frac{u_s}{u_{s_{peak}}} k_{nn} \frac{\partial \tau_{peak}}{\partial \sigma_n}, \text{if } u_s < u_{s_{peak}} \tag{2.59}$$

$$k_{sn} = \frac{\partial \tau}{\partial u_n} = \frac{k_{ns}}{u_p - u_{res}} \left\{ \frac{\partial \tau_p}{\partial \sigma_n} (u_s - u_{res}) + (u_{peak} \left[\frac{\partial \tau_{peak}}{\partial \sigma_n} \left(\text{Bo} + \frac{1 - Bo}{\sigma_t} \sigma_n \right) + \frac{\tau_{peak}}{\sigma_t} (1 - Bo) \right] \right\}, \tag{2.60}$$

$$\text{if } u_{s_{peak}} < u_s < u_{s_{res}}$$

$$k_{sn} = k_{nn} \left[\frac{\partial \tau_{peak}}{\partial \sigma_n} \left(\text{Bo} + \frac{1 - Bo}{\sigma_t} \sigma_n \right) + \frac{\tau_{peak}}{\sigma_t} (1 - Bo) \right], \text{if } u_s > u_{s_{res}} \tag{2.61}$$

Constant stiffness model

Main diagonal:

$$k_{ss} = \frac{\tau_{peak}}{u_{s_{peak}}}, \text{if } u_s < u_{s_{peak}} \tag{2.62}$$

$$k_{ss} = \frac{\partial \tau}{\partial u_s} = \frac{\tau_{peak} - \tau_{res}}{u_{peak} - u_{res}} + k_{ns} \frac{\partial \tau_{peak}}{\partial \sigma_n} \frac{1}{\tau_{peak}} \left(\frac{u_{peak} \tau_{res} - \tau_{peak} u_{res}}{u_{peak} - u_{res}} \right) \tag{2.63}$$

$$\text{if } u_{s_{peak}} < u_s < u_{s_{res}}$$

k_{ss} is given using the defined Equation (2.58), if $u_s > u_{s_{res}}$

Off-diagonal coupling terms:

$$k_{sn} = \frac{\partial \tau}{\partial u_n} = 0, \text{if } u_s < u_{s_{peak}} \tag{2.65}$$

$$k_{sn} = \frac{\partial \tau}{\partial u_s} = k_{nn} \frac{\partial \tau_{peak}}{\partial \sigma_n} \frac{1}{\tau_{peak}} \left(\frac{u_{peak} \tau_{res} - \tau_{peak} u_{res}}{u_{peak} - u_{res}} \right) \tag{2.66}$$

$$\text{if } u_{s_{peak}} < u_s < u_{s_{res}}$$

k_{sn} is given using the defined Equation (2.61), if $u_s > u_{s_{res}}$

In conclusion, Saeb and Amadei's model is considered a pioneer model because, in contrast with the existing models at that period, which were assuming that the normal stiffness is independent of the shear displacement (only valid for non-dilatant fractures), they proved that the normal stiffness of a rough discontinuity depends on both normal stress and shear displacement. Furthermore, Souley et al., (1995) presented a generalization of the Saeb and Amadei model to loading with changes in normal and shear loading directions (cyclic loading. On the other hand, Saeb and Amadei's model implicitly assumes that the shear strength of a discontinuity is independent of the stress path. This assumption may lead to incorrect results since depending on the stress path the contribution of shearing through asperities and sliding over asperities may vary with the stress path resulting in different joint surface damage.

2.4.6 Grasseli and Egger model

Grasselli and Egger (2003) introduced an empirical constitutive law for the description of the mechanical behaviour of a mated discontinuity subjected to shearing under CNL conditions. Based on observations on the experimental results of 45 shear tests on fresh tensile rough rock discontinuities, they derived an expression for the peak-shear strength that is valid for both natural rock discontinuities and mortar replicas. More specifically, observing the surfaces of sheared rock discontinuities they noted that the tensile strength is more important than compressive strength in quantifying the peak shear strength of matching rock discontinuities. Furthermore, in contrast to Barton-Bandis's strength criterion, which does not consider the three-dimensionalities of rock joints, they considered the morphology of the asperities concerning the shear direction.

Based on the assumption that the mechanical behaviour discontinuities can be properly reproduced though experiments on mortar replicas, their strength criterion is expressed as follows:

$$\tau_{peak} = \sigma_n tan\varphi_r^* \left(1 + e^{-(\theta_{max}^* B A_0 C)(\sigma_n/\sigma_c)}\right) \tag{2.68}$$

where σ_n expresses the applied normal stress, σ_c is the uniaxial compressive strength (of intact rock), φ_r^* is the residual friction angle measured after a shear displacement of 5mm, θ_{max}^* is the maximum apparent dip angle concerning to the shear direction (based on laboratory test on natural fractures the notes that has values in a range between 20° and 90°), B is a dimensionless fitting parameter (multiple least-squares regression using experimental results from 37 rock joint samples indicated that its value is equal to 9), A_0 is the maximum potential contact area for the specified shear direction and C is the roughness parameter.

The authors introduced the following empirical relationship for the calculation of the residual friction angle φ_r^*:

$$\varphi_r^* = \varphi_b + \left(\frac{\theta_{max}^*}{C}\right)^{1.18\cos a} \tag{2.69}$$

where φ_b is the basic friction angle, θ_{max}^* is the maximum apparent dip angle of the surface concerning the shear direction, C is the roughness parameter, and a is the angle between the schistosity plane and the normal to the joint. If the examined rock does not exhibit schistosity a is considered equal to zero. The value of the roughness parameter is calculated using a best-fit regression function (Grasseli, 2001).

Grasselli and Egger (2003) also observed from experimental results, that at the beginning of the shearing process, the discontinuity is not perfectly mated. Therefore, it was noted that a

small displacement occurs before the joint provides all its strength. Based on this observation they suggested that the displacement which corresponds to the peak shear strength of the joint is expressed as follows:

$$u_{peak} = u_m + \Delta u_{peak} \tag{2.70}$$

where u_m denotes the horizontal displacement necessary to mate the joint while the Δu_{peak} is the occurred horizontal displacement of the discontinuity before reaching its peak shear strength.

Moreover, through the observation of the experimental results Grasseli and Egger noted that as the discontinuity is mated, the shear stress-shear strain behaviour of a rock joint is almost linear till the peak shear stress. Thus, a linear relation is used to describe the shear stiffness of a rock discontinuity:

$$k_s = \frac{1}{\Delta u_{peak}} \frac{\tau_{peak}}{\sigma_n} \tag{2.71}$$

where τ_{peak} is the peak-shear strength, σ_n is the applied normal stress and Δu_{peak} is the occurred horizontal displacement of the discontinuity before reaching its peak shear strength

Furthermore, considering the characteristics of the experimentally observed shear stress-shear strain curves and based on the strength criterion that they introduced, they formulated a model able to capture the shear strength of a discontinuity subjected to shearing under CNL conditions:

$$\frac{\tau}{\sigma_n} = 0, \text{ if } 0 \le u_s \le u_m \tag{2.72}$$

$$\frac{\tau}{\sigma_n} = k_s(u_s - u_m) = \frac{1}{\Delta u_{peak}} \frac{\tau_p}{\sigma_n}(u_s - u_m), \text{ if } u_m \le u_s \le u_{peak} \tag{2.73}$$

$$\frac{\tau}{\sigma_n} = \frac{\tau_{res}}{\sigma_n} + \frac{\tau_{peak} - \tau_{res}}{\sigma_n} \frac{u_{peak}}{u_s}, \text{ if } u_s \ge u_{peak} \tag{2.74}$$

Concluding, Grasseli and Egger (2003) introduced a constitutive model which delineates with adequate accuracy experimental shear tests conducted both on replicas and fresh rock discontinuities. Additionally, the main pioneering characteristic of the created model is that can capture the anisotropy of the shear stress caused by the three-dimensional character of roughness (Grasselli, G., & Egger, P. (2003). In the created model, the contribution of roughness is not calculated based on single profiles (as Barton et.al (1985) suggested) but it captures parameters that are calculated on the entire fracture surface. Furthermore, experimental tests conducted by the same authors using their introduced strength criterion indicated the contribution of roughness in shear strength by proving that a rough joint provides much bigger shear strength than a smooth one.

On the other hand, the main limitations of the Grasseli and Egger model are that no attempt was made to investigate the influence of scale on shearing and that the model is based on the assumptions that the behaviour of replicas is the same as the behaviour of fresh rock fractures.

2.4.7 Overview table

In rock discontinuity modelling, a constitutive model is characterized as a "complete" model when it provides formulations which can be used to capture the stress-strain behaviour of a

discontinuity in both normal and/or shear direction. More specifically a complete constitutive model must provide the formulations of the strength criterion that is based on but also the formulation of shear and normal stiffness which it uses. The following table aims to denote the characteristics which are provided by each model which were described in the previous sections:

Table 2.1: Overview table of models' main characteristics

Models	Strength Criterion	Normal stiffness (k_n)	Shear stiffness (k_s)	Stress-strain relation	Characterization of model	Advantages	Disadvantages	Usage
Coulomb	Coulomb	Constant or stress dependent	Constant	Linear elastic perfectly plastic	Theoretical model	• Simple model • Easy-to-determine parameters • Easily extended using other laws	Can not represent accurately the non-linear experimentally observed mechanical behaviour	Highly used in industry and in research
Goodman	Landayi and Archamabault	Hyperbolic function	Constant or change with the amount of peak shear displacement	Non-linear in normal direction but piecewise linear in shear direction	Empirical model	Captures the softening behaviour of discontinuity during shearing (linear softening)	Dilation onsets once the shearing begins	Highly used in research
Barton-Bandis	Barton	Hyperbolic function	Not indicated or change with the amount of peak shear displacement	Non-linear	Empirical model	• Capture accurately the pre- and post-peak behaviour of a discontinuity under shearing • Fits well the experimental results	Strong non-linearity makes the implementation challenging	Highly used in industry and in research
Gens	Hyperbolic criterion (proposed by Gens et al.)	Hyperbolic function	Constant	Non-linear	Empirical model	• Captures anisotropy • High degree of flexibility	Complex integration procedure is required	Used in research
Saeb and Amadei	Modified Goodman	Hyperbolic function (Barton)	Constant or change with the amount of peak shear displacement	Non-linear	Theoretical model	Coupled stiffness terms	Assumes that the shear strength of a discontinuity is independent of the stress path	Used in research
Grasseli and Egger	Grasseli and Egger	Not indicated	Stress dependent	Non-linear	Empirical model	Captures anisotropy	No investigation of scale effects Assumes replicas behaviour same as natural discontinuities	Used in research

Table 2.1 provides an overview of the models which were found in the literature and described in the current chapter. Among the advanced models, the Barton-Bandis (BB) model is probably the most cited one, both in academic research and industry. However, in terms of practical adoption, Coulomb is the most adopted one due to its simplicity that is indicated by the adoption of one of the simplest linear shear failure criteria in combination with the small number and easy-to-determine required parameters. Furthermore, Coulomb's model can be "enhanced" by taking advantage of the linear softening trend that Goodman's model adopts. In this way, the post-peak behaviour of a discontinuity subjecting to shearing can be simulated using a simpler model with a simpler strength criterion than the one suggested by Landanyi and Archambault which is used by the original formulation of Goodman's model. Therefore, in the following, these two main families of models, based on Coulomb and BB models, will be investigated in detail. Concretely, in the next chapter, theoretical simulation will be carried out on these models for the modelling of laboratory tests.

3 Theoretical simulation of Constant Normal Load tests with different discontinuity constitutive models

3.1 Introduction

Theoretical simulations of a typical Constant Normal Load (CNL) test will be carried out in this chapter. To this end, incremental equations are formulated for each constitutive model within the framework of Plasticity theory and integrated using an explicit integration scheme. These equations are then implemented in a Python script to simulate a two-phased laboratory test using a monotonic loading path (e.g., a normal compression test followed by a direct shear test keeping the loading level in the normal direction reached at the end of the compression phase constant).

The objective of this simulation is multifold. First, it helps to enhance the understanding of the different constitutive models presented above. Second, the formulation of the incremental governing equations can serve as a base for the Finite Element (FE) numerical implementation presented in a later chapter. Finally, these theoretical simulations also serve as a reference solution for the verification of FE modelling.

In this chapter, as aforementioned, only two families of constitutive models are selected for this in-depth investigation. These models are selected based on both their theoretical consistency and practical values. All of them are formulated within the Plasticity theory, which has been proven to be convenient and rigorous for FE implementation. They are also widely accepted in both practical rock engineering and academic research. Concretely, the following models are considered:

1. Coulomb-based models, including different versions: elastic-perfectly plastic Coulomb model (original version), elasto-plastic model with strain softening, and elasto-plastic model with strain softening and nonlinear stiffnesses.
2. Barton-Bandis-based models, including different versions: modified BB model and elastic-perfectly plastic BB model with hyperbolic nonlinear stiffnesses.

In the following, the general equations of plasticity and an explicit integration scheme are presented. These equations will apply to each specific model for the simulation of CNL tests.

3.2 General constitutive equations in plasticity theory

The description of the mechanical behaviour of rock discontinuities is formulated through the following relations:

The stress vector is composed of its directional components:

$$\underline{d\sigma} = [d\sigma_n \quad d\tau]^T \tag{3.1}$$

where σ_n and τ represent the normal and shear stresses, respectively while d denotes the increment.

Similarly, the displacement vector can be represented as follows:

$$\underline{du} = [du_n \quad du_s]^T \tag{3.2}$$

where u_n and u_s are the normal and shear displacements, respectively.

Furthermore, elastoplastic modelling of rock discontinuities begins by postulating that the joint displacement can be additively decomposed into elastic and inelastic (plastic) parts (basic principle of elastoplasticity) as:

$$u = u^e + u^p \tag{3.3}$$

In Equation (3.3) the superscripts *e* and *p* denote the elastic and the plastic deformations, respectively. Accordingly, the normal and shear displacement of a rock discontinuity can be decomposed into their elastic and plastic components as follows:

$$du_n = du_n^e + du_n^p \tag{3.4}$$

$$du_s = du_s^e + du_s^p \tag{3.5}$$

Considering Hooke's law and the just introduced formulations, the deformability of a discontinuity (stress-strain relationship) can be described using the following differential formulation:

$$\begin{bmatrix} d\sigma_n \\ d\tau \end{bmatrix} = \begin{bmatrix} k_n & 0 \\ 0 & k_s \end{bmatrix} \begin{bmatrix} du_n^e \\ du_s^e \end{bmatrix} \tag{3.6}$$

In Equation (3.6), the stress vector is related to the strain vector based on the (2 x 2) non-symmetrical matrix of the material's tangent stiffness. Within the plasticity framework, the condition which defines the limit of elasticity and the beginning of plastic deformation under any combination of stresses is known as the yield condition or yield criterion. All the generated strains are recoverable in the elastic region once the applied stress is removed. However, once the yield criterion is reached, some of the generated deformations will be permanent and irrecoverable. This part of the deformation is also known as plastic deformation.

The yield criterion is represented by a surface in the stress space, known as the yield surface. Mathematically, the yield surface is expressed through a formulation which is called yield function. When the stress state is located within the boundaries of the yield surface, the behaviour of the material is characterized as elastic. Once the generated stress state is located on the yield surface, the generation of plastic deformations is initiated. Plastic deformations lead to the hardening of the material and the increase of its elastic limit. In other words, the yield surface will not be fixed in the stress space, but it will change its size (expand or shrink) based on the previous plastic deformation and loading history.

The expansion of the yield surface denotes the hardening of the material while the shrinking of the yield surface points out that the material is undergoing softening. The mathematical formulation of the yield function of the constitutive models which are capable of capturing the hardening and softening behaviour is often expressed as a function of the stress vector $\underline{\sigma}$ and of a so-called state parameter κ (the evolution of the state parameter itself is generally expressed as a function of the plastic displacement u^p) as follows:

$$F(\underline{\sigma}, \kappa) = 0 \tag{3.7}$$

On the other hand, the constitutive models which use simpler constitutive laws to describe the mechanical behaviour of discontinuities have been formulated within the framework of perfect plasticity. In this case, the size of the yield surface is fixed and does not fluctuate with stress history. The mathematical formulation of the yield function of these models is expressed only as a function of $\underline{\sigma}$ as follows:

$$F(\underline{\sigma}) = 0 \tag{3.8}$$

For each stress state, the value of the yield function is examined. If its value is below zero, the applied stress path is located within the yield contour and the generated strains remain elastic. On the contrary, if the yield function is reached the rate of plastic displacements is governed by a non-associative flow rule which requires the introduction of a plastic potential $G \neq F$. The rate of plastic displacements is calculated based on the so-called flow rule as follows:

$$d\underline{u^p} = d\lambda \frac{\partial G}{\partial \underline{\sigma}} \tag{3.9}$$

where the plastic multiplier λ defines the magnitude of the plastic deformations.

3.3 General incremental equations for an explicit integration scheme for CNL configuration

The aim of this section is to provide a general framework of constitutive relationships compatible with an explicit integration algorithm. It must be pointed out that in favour of generality, the incremental formulations have been written considering the yield function of a non-elastoplastic model (the state parameter is represented by the plastic shear displacement $u_s{}^p$).

The formulation of the relationship between stress rates and strain rates according to elastoplasticity theory starts from Hooke's law of elastic strains. Therefore, using the differential formulation for the deformability of rock discontinuities derived in Equation (3.6), the evolution of normal stress $d\sigma_n$ can thus be expressed as a function of normal stiffness k_n and elastic normal strain rates $du_n{}^e$:

$$d\sigma_n = k_n du_n{}^e \tag{3.10}$$

Equation (3.10) can be further detailed as follows:

$$u_{n_k}^e = \frac{(\sigma_{n_k} - \sigma_{n_{k-1}})}{k_n} + u_{n_{k-1}}^e \tag{3.11}$$

where k denotes the current calculation step of the integration scheme while $k-1$ indicates the previous calculation step.

Similarly, the evolution of shear stress can be expressed from the following equation:

$$d\tau = k_s du_s{}^e \tag{3.12}$$

Considering the basic principle of elastoplasticity introduced by Equation (3.5) and the flow rule expressed in Equation (3.9) the shear stress increment is further elaborated in the following relation:

$$d\tau = k_s(du_s - du_s{}^p) = k_s(du_s - d\lambda\frac{\partial G}{\partial \tau}) \tag{3.13}$$

By integrating this formula, the following relation is obtained:

$$\int_{\tau_{k-1}}^{\tau_k} d\tau = \int_{u_{s_{k-1}}}^{u_{s_k}} k_s du_s - \int_{u_{s_{k-1}}}^{u_{s_k}} k_s d\lambda\frac{\partial g}{\partial \tau} \tag{3.14}$$

Further, elaboration of equation (3.14) leads to the following formulation:

$$\tau_k = \tau_{k-1} + \int_{\tau_{k-1}}^{\tau_k} d\tau = \tau_{k-1} + \int_{u_{s_{k-1}}}^{u_{s_k}} k_s du_s - \int_{u_{s_{k-1}}}^{u_{s_k}} k_s d\lambda\frac{\partial G}{\partial \tau} \tag{3.15}$$

By setting

$$\tau^* = \tau_{k-1} + \int_{u_{s_{k-1}}}^{u_{s_k}} k_s du_s \tag{3.16}$$

and

$$d\tau^p = \int_{u_{s_{k-1}}}^{u_{s_k}} k_s d\lambda\frac{\partial G}{\partial \tau} \tag{3.17}$$

considering also the derived Equation (3.9), Equation (3.17) can be specified as follows:

$$d\tau^p = \int_{u_{s_{k-1}}}^{u_{s_k}} k_s du_s{}^p \tag{3.18}$$

thus Equation (3.15) can be rewritten as:

$$\tau_k = \tau^* - d\tau^p \tag{3.19}$$

where τ^* represents the so-called elastic trial.

Considering Equation (*3.18*), Equation (3.19) can be further modified as follows:

$$\tau^* - \tau_k = \int_{u_{s_{k-1}}}^{u_{s_k}} k_s du_s^p \tag{3.20}$$

Solving the integral of Equation (3.20) the following relation is obtained:

$$\tau^* - \tau_k = k_s(u_{s_k}^p - u_{s_{k-1}}^p) \tag{3.21}$$

Equation (3.19) indicates that the calculated value of shear stress of each calculation step is equal to the calculated value of τ^* when the generated strains are purely elastic (no plastic strains, therefore, $d\tau^p = 0$). In more detail, for each calculation step of the integration scheme the value of the elastic trial τ^* is calculated. Based on its value the yield function $F(\tau^*, \kappa)$ is calculated. If the calculated value of $F(\tau^*, \kappa)$ is lower than zero, then the occurred stress state is within the boundaries of the yield surface and the generated strains are elastic. In this case, the value of shear stress of the calculation step τ_k is equal to the calculated value of τ^*.

On the other hand, if the value of the yield function $F(\tau^*, \kappa)$ is larger than zero, then the trial stress state is located outside the yield surface and plastic strains are generated (plastic loading). As stress states cannot be outside the elastic region, a correction factor $d\tau^p$, expressed as a function of the plastic multiplier $d\lambda$, is applied to return the occurred stress state on the yield surface. The shear stress at step τ_k is obtained by subtracting the value of $d\tau^p$ to τ^*.

In addition, by further elaborating Equation (3.19), a general formulation for the calculation of the increment of the generated plastic shear displacements is obtained. We consider here a typical case where

$$\kappa = u_s^p \tag{3.22}$$

In this case, Equation (3.19) is further modified by applying the chain rule in partial differentiation as follows:

$$F\left(\tau^*, u_s^{p*}\right) - F\left(\tau_k, u_{s_k}^p\right) = \frac{\partial F}{\partial \tau}(\tau^* - \ \tau_k) + \frac{\partial F}{\partial u_s^p}\left(u_s^{p*} - u_{s_k}^p\right) \tag{3.23}$$

Assuming plastic conditions, the elastic trial of plastic shear strain u_s^{p*} is equal to the value of the generated plastic shear strain of the previous step of the integration scheme, $u_{s_{k-1}}^p$. Furthermore, also considering the derived Equation (3.21), Equation (3.23) can be further specialized as follows:

$$F\left(\tau^*, u_s^{p*}\right) - F\left(\tau_k, u_{s_k}^p\right) = \frac{\partial F}{\partial \tau} k_s (u_{s_k}^p - u_{s_{k-1}}^p) - \frac{\partial F}{\partial u_s^p}\left(\ u_{s_k}^p - u_{s_{k-1}}^p\right) \tag{3.24}$$

Reformulation of Equation (3.24) leads to the following equation through which the calculation of the generated plastic shear strain of each step of the integration scheme can be executed:

$$du_s^p = \frac{F(\tau^*, u_s^{p*}) - \ F\left(\tau_k, u_{s_k}^p\right)}{\frac{\partial F}{\partial \tau} k_s - \frac{\partial F}{\partial u_s^p}} \tag{3.25}$$

Moreover, considering that during plasticity the value of the yield function is equal to zero the value of the term $F(\tau_k, u_{s_k}^p)$ should be zero. Therefore, the reported Equation (3.25) is simplified as given below:

$$du_s^p = \frac{F(\tau^*, u_s^{p*})}{\frac{\partial F}{\partial \tau} k_s - \frac{\partial F}{\partial u_s^p}} \tag{3.26}$$

Finally, further elaboration on the Equation (3.26) using the derived equation (3.9) leads to the following expression of $d\lambda$:

$$d\lambda = \frac{F(\tau^*, u_s^{p*})}{\left(\frac{\partial F}{\partial \tau} k_s - \frac{\partial F}{\partial u_s^p}\right)\frac{\partial G}{\partial \sigma_n}} \tag{3.27}$$

Thus, the calculation of the increment of the occurred normal displacement during the shear loading is executed as follows:

$$du_n^p = d\lambda \frac{\partial G}{\partial \sigma_n} \tag{3.28}$$

Using a state parameter represented by the plastic shear displacement is a convenient choice in plasticity numerical implementation. However, constitutive models for discontinuities are often calibrated based on standard laboratory tests using the total shear displacements rather than the plastic ones. To be more in line with the existing models employing total shear displacement, which is easier to measure during lab tests, a new set of constitutive relationships using a special state variable is formulated hereafter.

In more detail, the state parameter κ for each step of the employed explicit scheme is defined as follows:

$$\kappa_k = \begin{cases} \kappa_{k-1} & if\ F(\tau^*, \kappa_{k-1}) < 0 \\ \kappa_{k-1} + du_s & if\ F(\tau^*, \kappa_{k-1}) \geq 0 \end{cases} \tag{3.29}$$

This amounts to saying that the state variable is the accumulated total displacement only during plastic loading. Mathematically, this state variable may be written as:

$$\kappa = \int du_s H(du_s^p) \tag{3.30}$$

With H represents the Heaviside step function. As explained, the state variable accumulates the total displacements only when plastic strain is generated.

In this way, the state variable can be updated based on the check of whether the loading step is plastic or elastic, based on the trial stress state τ^*. Applying the chain rule in partial differentiation in Equation (3.19) leads to the following expression:

$$F(\tau^*, \kappa_k) - F(\tau_k, \kappa_k) = \frac{\partial F}{\partial \tau}(\tau^* - \ \tau_k) \tag{3.31}$$

Assuming plastic conditions, the value of the yield function of the current integration step $F(\tau_k, \kappa_k)$ is equal to zero. Thus, the Equation is further modified as follows:

$$\tau_k = \tau^* - \frac{F(\tau^*, \kappa_k)}{\frac{\partial F}{\partial \tau}} \tag{3.32}$$

Finally, further elaboration on the Equation (3.26) leads to the following expression of $d\lambda$:

$$d\lambda = \frac{F(\tau^*, \kappa_k)}{\frac{\partial F}{\partial \tau} k_s \frac{\partial G}{\partial \sigma_n}} \tag{3.33}$$

The above equations can be written and simplified when applied to the specific configuration of the CNL test. During the normal compression stage, the normal stress is applied, and shear stress is kept at zero. The plastic strain is supposedly not generated, and we get:

$$d\sigma_n = k_n du_n \tag{3.34}$$

$$d\tau = 0;\ du_s = 0$$

During the shearing stage, a shear displacement is applied, while the normal stress is kept constant:

$$d\sigma_n = 0 \tag{3.35}$$

3.4 Enhanced Coulomb constitutive models

This section introduces the formulated incremental equations for each constitutive model. The derived equations for each model were implemented in a Python script to simulate a two-phased laboratory test using a monotonic loading path. The results of the considered laboratory test are reported by highlighting the main characteristics of each constitutive law. The mechanical response of a discontinuity in a limestone (γ = 25 kN/m^3) located at a 40m depth was selected to be theoretically simulated using the considered Python script.

3.4.1 Perfect elastoplastic Coulomb model

The first set of constitutive relationships considers the Coulomb strength criterion associated with linear formulations (constant) for both normal and shear stiffnesses. The Coulomb model is the most well-known linear elastic perfectly plastic model.

As previously mentioned (Section 3.2), the yield function of a constitutive relationship formulated in the framework of perfect plasticity is a function of the stress tensor only. The shear strength of a discontinuity using the Coulomb model is characterized by the following formulation of the yield function:

$$F(\tau) = \tau - \sigma_n tan\varphi + c \leq 0 \tag{3.36}$$

where φ indicates the friction angle.

Furthermore, the Coulomb model is described by a non-associated flow rule. Once the peak strength is reached the yield function turns to zero and the plastic potential is activated. The form of plastic potential is given by:

$$G(\tau) = \tau - \sigma_n tan\psi + c \tag{3.37}$$

where ψ represents the dilation angle.

The required parameters for the simulation of the two-phased laboratory test adopting the perfect elastoplastic Coulomb model and their values are illustrated in the table below:

Table 3.1: Required parameters for perfect elastoplastic Coulomb model

Parameters	Values
$\boldsymbol{c}$	0
$\boldsymbol{\varphi}$	30°
$\boldsymbol{\psi}$	15°
$\boldsymbol{k_n}$	18.8 MPa/mm
$\boldsymbol{k_s}$	10 MPa/mm

Simulation of normal compression test

For simulating the normal compression phase (no shearing occurs), a nil initial stress level has been assumed ($\sigma_{n_{ini}} = 0$) and a normal load equal to 1 MPa is incrementally applied for a specified number of calculation steps N.

Considering that the value of normal stiffness does not vary with the amount of the applied normal stress and that during the compression phase, the plastic strain is supposedly nil (as stated in Section 3.3), Equation (3.11) was employed.

Figure 3.1 shows the results obtained for this first phase of the simulated laboratory test for several selected calculation steps N.

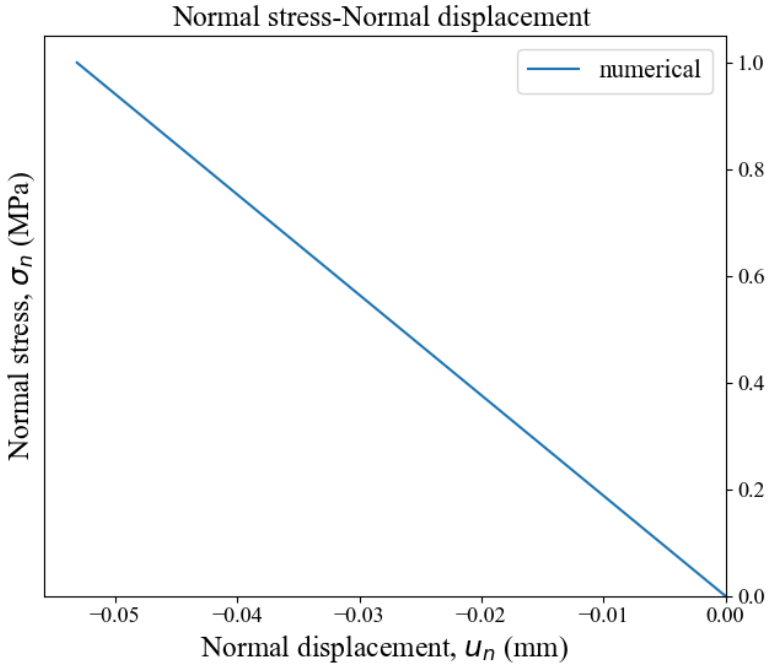

Figure 3.1: Normal Displacement vs Normal Stress using the perfect elastoplastic Coulomb model

Simulation of direct shear test under CNL conditions

The simulation of the direct shear test under CNL conditions assumes that the final compression level of the previous phase ($\sigma_n = 1\ MPa$) is now kept constant while a shear displacement $u_s = 10\ mm$ is incrementally applied. For the simulation of the direct shear test one thousand integration steps were considered.

The calculation of the applied shear stress was executed based on Equation (3.19). More specifically, the calculation of the elastic trial, τ^* was executed using the introduced Equation (3.16)

It must be noted that in contrast with the introduced equations which have been formulated within the general framework of hardening the considered model is based on the framework of perfect plasticity. Thus, the formulated equations were specialized within the framework of perfect plasticity by taking into account two main changes. Firstly, the yield function is expressed as a function of stress only (as stated in Section 3.2) while secondly due to the absence of the state parameter, the values of all the presented derivatives with respect to the state parameter are equal to zero.

Considering the noted changes and rearranging Equation (3.23) a formulation for the calculation of the correction factor $d\tau^p$ was obtained as follows:

$$d\tau^p = \frac{F(\tau^*) - F(\tau_k)}{\frac{\partial F}{\partial \tau}} \tag{3.38}$$

Accordingly, the value of the plastic multiplier was acquired by employing Equation (3.27). Having calculated the value of the plastic multiplier the value of the generated plastic normal deformation in each step of the integration step was obtained using Equation (3.28).

Finally, by taking into account the formulations of both yield function and plastic potential reported in Equations (3.36) and (3.37) respectively, the values of the presented derivatives in the introduced equations are calculated as follows:

$$\frac{\partial F}{\partial \tau} = \frac{\tau - \sigma_n tan\varphi + c}{\partial \tau} = 1 \tag{3.39}$$

and

$$\frac{\partial G}{\partial \tau} = \frac{\tau - \sigma_n tan\psi + c}{\partial \tau} = 1 \tag{3.40}$$

Figure 3.2 and Figure 3.3 show the results obtained for the direct shear test.

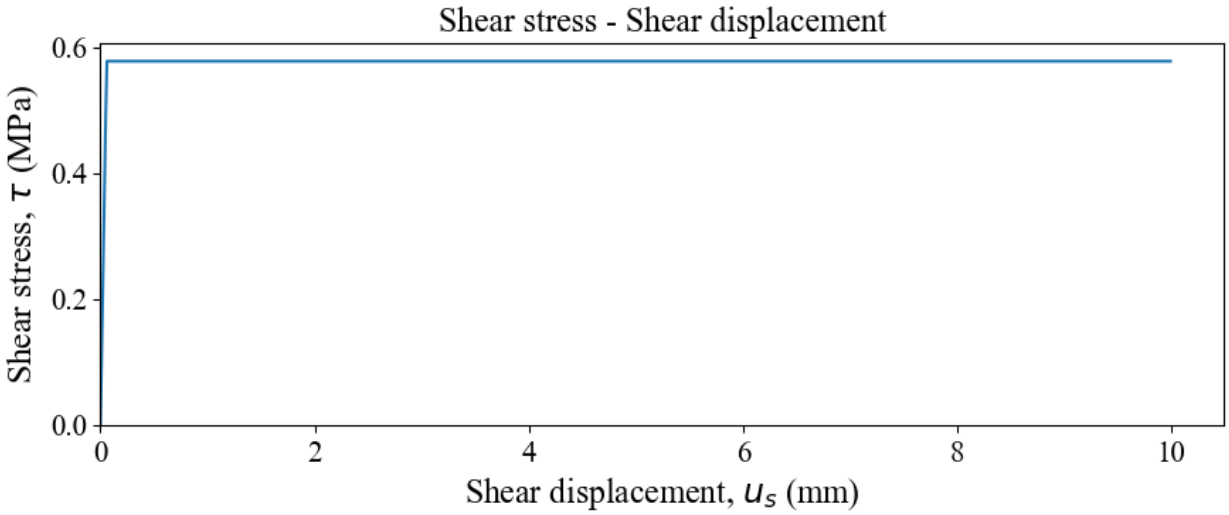

Figure 3.2: Shear displacement vs Shear stress using the perfect elasto-plastic Coulomb model

The reliability of the shear stress-displacements plot (Figure 3.2) is confirmed by verifying that the slope of the elastic phase corresponds to the introduced valued shear stiffness and that the shear stress once the peak is reached complies with the value obtained from the expression of the adopted constitutive relation:

$$\tau_{peak} = \sigma_n tan\varphi = 1 * tan30° = 0.58\ MPa$$

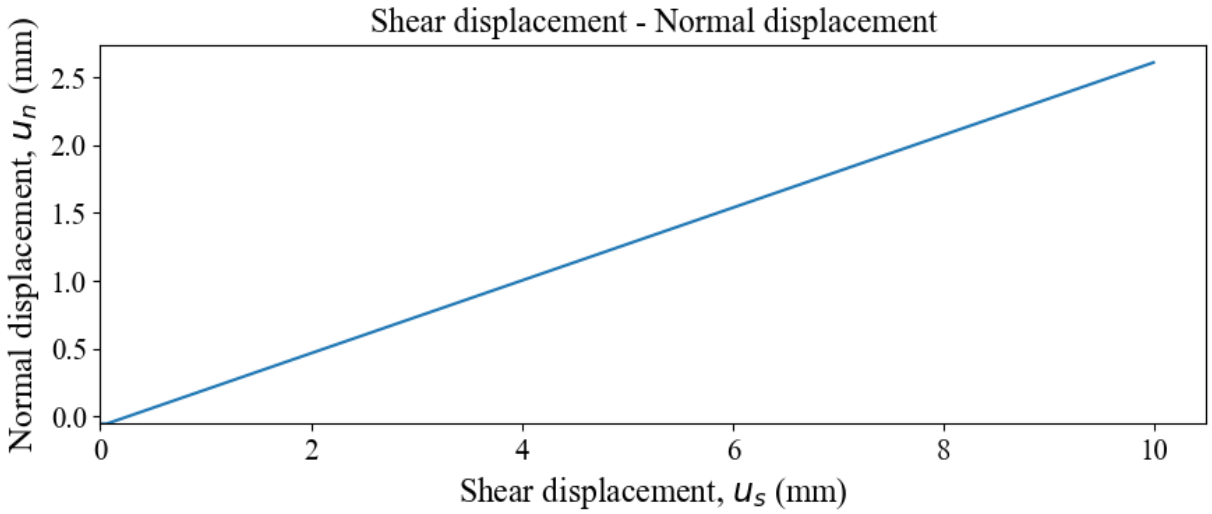

Figure 3.3: Shear displacement vs Normal displacement using the perfect elasto-plastic Mohr-Coulomb

The phenomenon of dilation which is associated with the mechanical behaviour of a discontinuity subjecting to shearing, is illustrated in Figure 3.3. As was stated in Section 3.1 the shearing phase under CNL conditions follows the compression phase which was described in the previous section. Considering this sequence, the observed (negative) value of normal displacement at the beginning of shearing corresponds to the maximum normal displacement (compression) which was noted during the first phase. In addition, it must be pointed out that the application of shear displacement makes the values of normal displacement increase (become less negative). This increment denotes the phenomenon of dilation.

The reliability of the obtained results was confirmed by verifying that the dilation onsets at the amount of shear displacement which corresponds to the amount of shearing that is required to

be applied to reach the peak shear stress. More specifically, once the peak shear stress has been reached, plastic deformations (dilation) are generated. Furthermore, the next feature which was employed for the assessment of the results was the value of the slope of the line which describes the evolution of the dilation, and which was verified to be equal to the value of the dilation angle as was expected.

3.4.2 Elastoplastic with linear softening Coulomb model

In contrast with the set of constitutive relationships introduced in the previous section which describes the mechanical behaviour of a discontinuity within the framework of perfect plasticity, the second set of constitutive relationships captures more accurately the post-peak mechanical behaviour of a discontinuity by considering the softening behaviour.

In more detail, the presented model of this section considers the Coulomb strength criterion in combination with the elastoplastic constitutive relationships with strain softening proposed by Goodman (1976). Modifying accordingly Goodman's constitutive relationships presented in Section 2.4.2, the calculation of the shear strength of a discontinuity was based on the amount of the generated plastic strains (state parameter) as follows:

$$\tau = \sigma_n tan\varphi + c, \quad for \ \kappa = 0 \tag{3.41}$$

$$\tau = \tau_{peak} - \left(\tau_{peak} - \tau_{res}\right)\frac{\kappa}{Dc}, \quad for \ 0 < \kappa < Dc \tag{3.42}$$

$$\tau = \sigma_n tan\varphi_{res} + c_{res}, \quad for \ \kappa > Dc \tag{3.43}$$

As can be observed from the reported constitutive relationships, the calculation of shear stress of each step of the integration scheme is based on the relationship between the value of the state parameter κ and the value of the Dc parameter. In more detail, Dc is called critical distance and denotes the difference between the amount of shear displacement which is required to reach the peak and the residual shear displacement ($Dc = u_{s_{res}} - u_{s_{peak}}$) . It must be pointed out that, the critical distance is considered an input parameter in the Coulomb with linear softening model.

As was stated in Section 3.2, the mathematical formulation of the yield function of the models which can capture the softening behaviour is expressed not only as a function of the stress tensor $\sigma_{ij,}$but also as a function of the state parameter**.** Considering the formulation of the state parameter introduced by Equation (3.29) and combining this characteristic of the considered model with the reported elastoplastic constitutive relationships with strain softening the general form of the yield function was written. More specifically, Equation (3.42) was further elaborated as follows:

$$F(\tau, \kappa) = \tau - \tau_{peak}\left(1 - \frac{\kappa}{Dc}\right) - \tau_{res}\left(\frac{\kappa}{Dc}\right) \leq 0 \tag{3.44}$$

Replacing in Equation (3.44) τ_{peak} and τ_{res} with their formulation based on the Coulomb strength criterion:

$$F(\tau, \kappa) = \tau - (\sigma_n tan\varphi + c)\left(1 - \frac{\kappa}{Dc}\right) - (\sigma_n tan\varphi_{res} + c_{res})\left(\frac{\kappa}{Dc}\right) \leq 0 \tag{3.45}$$

Furthermore, as it was stated in Section 3.4.1, a non-associated flow rule is considered to avoid the overestimation of dilation given by the associated flow rule. Therefore, once the peak strength is reached the yield function turns to zero and the plastic potential is activated. The form of plastic potential is given as follows:

$$G(\tau, \kappa) = \tau - (\sigma_n tan\psi + c)\left(1 - \frac{\kappa}{Dc}\right) - (\sigma_n tan\psi_{res} + c_{res})\left(\frac{\kappa}{Dc}\right) \quad (3.46)$$

Finally, in the second set of the constitutive relationships, the experimentally proven behaviour which denotes that the dilation is limited was considered. In more detail, according to Zhao et al. (2011), the accumulated dilation is generally limited either by a critical normal stress level or by a critical shear displacement. Based on that statement, during the simulation of the direct shear test under CNL conditions, a critical distance was adopted after which no further dilation is observed (dilation cut-off). It should be pointed out that the value of this parameter denotes the amount of shear displacement that is required to be added to the amount of shear displacement which corresponds to the peak shear strength to eliminate the dilation.

The required parameters for the simulation of the considered two-phased laboratory test adopting the elastoplastic with linear softening Coulomb model and their values are illustrated in the table below:

Table 3.2: Required parameters for elastoplastic with linear softening Coulomb model

Parameters	Values
$\boldsymbol{c}$	0
$\boldsymbol{c_{res}}$	0
$\boldsymbol{\varphi}$	30°
$\boldsymbol{\varphi_{res}}$	20°
$\boldsymbol{\psi}$	15°
$\boldsymbol{\psi_{res}}$	10°
$\boldsymbol{k_n}$	18.8 MPa/mm
$\boldsymbol{k_s}$	10 MPa/mm
$\boldsymbol{Dc}$	2 mm
dilation cut-off	8.95 mm

Simulation of normal compression test

The new set of constitutive relationships presented in this chapter significantly affects the evolution of the mechanical behaviour of a discontinuity only during the application of shear displacement. Thus, considering also that the current model adopts a constant value of normal stiffness the compression phase of this section is the same as the one presented in Section 3.4.1.

Simulation of direct shear test under CNL conditions

Similarly, to the previous section, the simulation of the direct shear test under CNL conditions assumes that the final compression level of the previous phase ($\sigma_n = 1\ MPa$) is now kept constant while a shear displacement $u_s = 10\ mm$ is incrementally applied. For the simulation of the direct shear test ten thousand integration steps were considered.

The process followed for the calculation of the evolution of shear stress during shearing for each step of the implemented explicit scheme is illustrated in detail in the following flowchart:

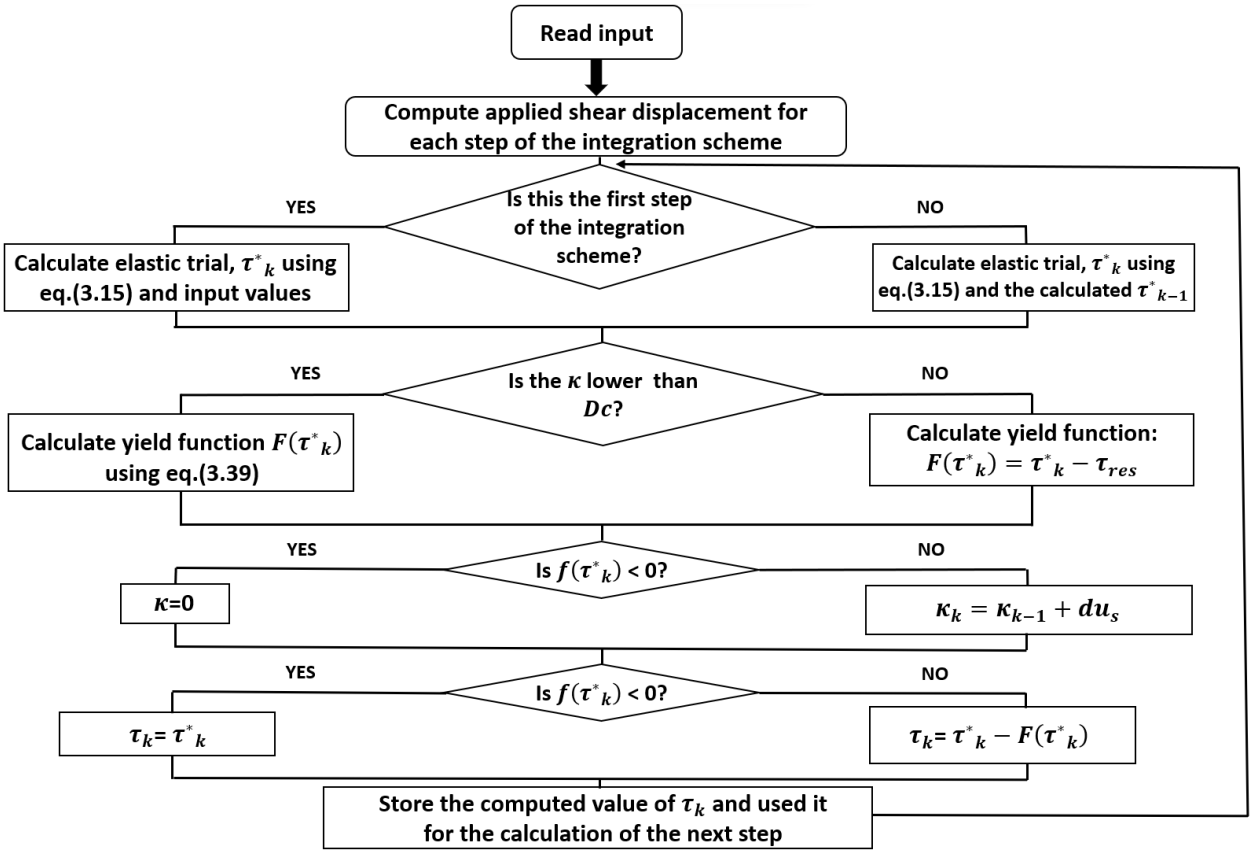

Figure 3.4: Flowchart for the calculation of shear stress using the Coulomb model with linear softening model

In addition, considering also the general formulations of the yield function and plastic potential reported in Equations (3.45) and (3.46) the values of the presented derivatives were calculated as follows:

$$\frac{\partial F}{\partial \tau} = 1 \tag{3.47}$$

$$\frac{\partial F}{\partial u_s^p} = \frac{\tau_{peak} - \tau_{res}}{u_s^{peak} - u_s^{res}} \tag{3.48}$$

$$\frac{\partial G}{\partial \sigma_n} = \tan\psi \tag{3.49}$$

Finally, the occurred normal displacements (dilation) were calculated, using the derived Equation (3.28).

Figure 3.5 and Figure 3.6 show the results obtained for the direct shear test.

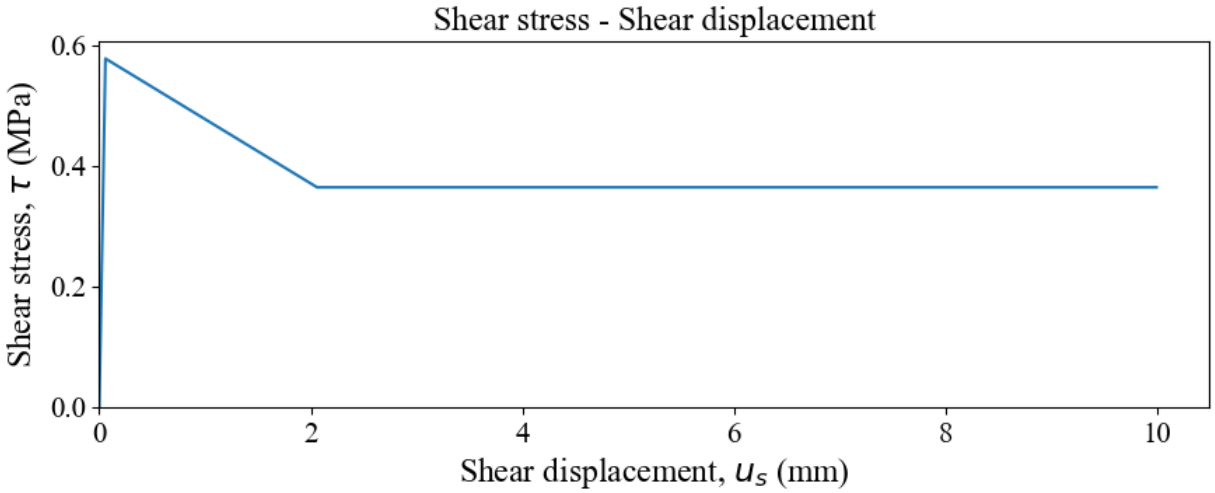

Figure 3.5: Shear displacement vs Shear stress using the Coulomb with linear softening model

As in the previous section, so in this chapter also, the reliability of the shear stress-displacements plot (Figure 3.5) is confirmed by verifying that the slope of the elastic phase corresponds to the introduced valued shear stiffness and that the shear stress once the peak is reached while also once the residual condition is reached complies with the value obtained from the expressions of the adopted constitutive relations:

$$\tau_{peak} = \sigma_n tan\varphi = 1 * tan30° = 0.58\, MPa$$

$$\tau_{res} = \sigma_n tan\varphi_{res} = 1 * tan20° = 0.36\, MPa$$

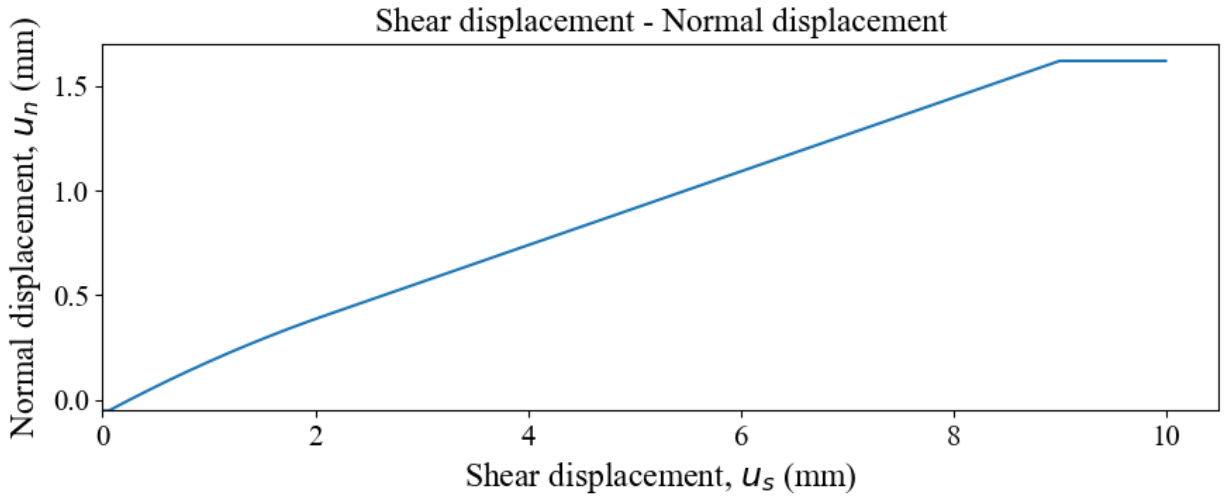

Figure 3.6: Shear displacement vs Normal displacement using the Coulomb with linear softening model

Figure 3.6, denotes that the created model can simulate adequately the phenomenon of dilation during the shearing process. The obtained peak value of dilation is equal to 1.62 mm. The first feature, which was used for the verification of the correctness of the results was the amount of shear displacement which is required for the generation of plastic strains. More specifically, similar to the previous shearing simulation the generation of dilation starts once the peak shear stress is reached. Additionally, it must be noted that the reliability of the results is verified by verifying that the slope of the dilation angle is as expected. More specifically, it can be observed that once the dilation starts the inclination of the line which describes its evolution changes.

Once the dilation starts the inclination of the line which describes the evolution dilation is equal to the value of the dilation angle ψ as was expected. However as denoted from Figure 3.6 after the further application of 2 mm of shear displacement the strength of the discontinuity obtains its residual values, and the inclination of the observed line is equal to the value of the residual dilation angle ψ_{res} (as it was also expected). Finally, the last feature that verifies the correctness of the extracted result is that the dilation reaches a plateau when an amount of shear displacement is equal to the value of the set critical distance (8.95 mm) applied once the peak shear strength is reached.

3.4.3 Elastoplastic with linear softening and non-linear stiffness Coulomb model

3.4.3.1 Power law

The third set of constitutive relationships considers the Coulomb strength criterion associated with nonlinear stiffnesses (stress-dependent) complying with a power law for both normal and shear stiffnesses:

$$k_n = k_{n_{ini}}(\sigma_n)^{e_n} \tag{3.50}$$

$$k_s = k_{s_{ini}}(\sigma_n)^{e_s} \tag{3.51}$$

where k_n and k_s denotes the stiffness values for the considered calculation step and are obtained based on their initial values ($k_{n_{ini}}$ and $k_{s_{ini}}$) and the so-called stiffness exponents (e_n and e_s). Both normal and shear stiffnesses depend on the current normal stress level (σ_n) which varies during the loading path.

Furthermore, the formulations of the yield function and the plastic potential have been reported by Equations (3.36) and (3.37) respectively.

The required parameters for the simulation of the considered two-phased laboratory test adopting the elastoplastic with linear softening Coulomb model and their values are illustrated in the table below:

Table 3.3: Required parameters for elastoplastic Coulomb model with linear softening and power non-linear stiffnesses

Parameters	Values
$\boldsymbol{c}$	0
$\boldsymbol{c_{res}}$	0
$\boldsymbol{\varphi}$	30°
$\boldsymbol{\varphi_{res}}$	25°
$\boldsymbol{\psi}$	15°
$\boldsymbol{\psi_{res}}$	10°
$\boldsymbol{k_{n_{ini}}}$	18.8 MPa/mm
$\boldsymbol{k_{s_{ini}}}$	10 MPa/mm
$\boldsymbol{e_n}$	1.1
$\boldsymbol{e_s}$	1.1
$\boldsymbol{Dc}$	2 mm
dilation cut-off	8.95 mm

Simulation of normal compression test

Accordingly, to the previous sections for simulating the normal compression phase (no shearing occurs), a nil initial stress level has been assumed ($\sigma_{n_{ini}} = 0$) and a normal load equal to 1 MPa is incrementally applied for a specified number of calculation steps N.

Considering that during the compression phase, the plastic strain is supposedly nil (as stated in Section 3.3), the formulation of k_n reported in Equation (3.50) was employed to specialised Equation (3.11) through which the occurred normal deformation of each integration step was calculated.

Figure 3.7 shows the results obtained for this first phase of the simulated laboratory test for several selected calculation steps N.

To assess the reliability of this model, the obtained results are compared with the concerning analytical solution which formulation can be obtained through the integration of Equation (3.10):

$$\int_{u_{n_{ini}}}^{u_{n_{fin}}} du_n{}^e = \int_{\sigma_{n_{ini}}}^{\sigma_{n_{fin}}} \frac{d\sigma_n}{k_n} \tag{3.52}$$

and further specialised by replacing k_n from Equation (3.11):

$$u_{n_{fin}}^e - u_{n_{ini}}^e = \int_{\sigma_{n_{ini}}}^{\sigma_{n_{fin}}} \frac{d\sigma_n}{k_n \sigma n^{e_n}} \tag{3.53}$$

Considering that the initial condition corresponds to nil normal displacement ($u_{n_{ini}}^e = 0$) and solving the integral of Equation (3.29), the formulation of the analytical solution of the adopted model is obtained:

$$u_{n_{fin}}^e = \frac{1}{k_n}\left(\frac{\sigma_{n_{fin}}{}^{-e_n+1} - \sigma_{n_{ini}}{}^{-e_n+1}}{-e_n+1}\right) \tag{3.54}$$

In this equation the exponent $-e_n + 1$ has a value lower than 0 (in general $e_n > 1$). This has required setting the value of the initial stress level ($\sigma_{n_{ini}}$) slightly higher than zero. A value equal to 0.1 KPa has been assumed.

The analytical loading curve is shown in Figure 3.7 together with the curves obtained from the implemented solution solved for different incremental steps N. The results confirm the reliability of the implementation. However, as expected (due to the adoption of an explicit integration scheme), the implemented solutions required a high number of steps (approximately N ≥ 20 M) to fit the analytical results.

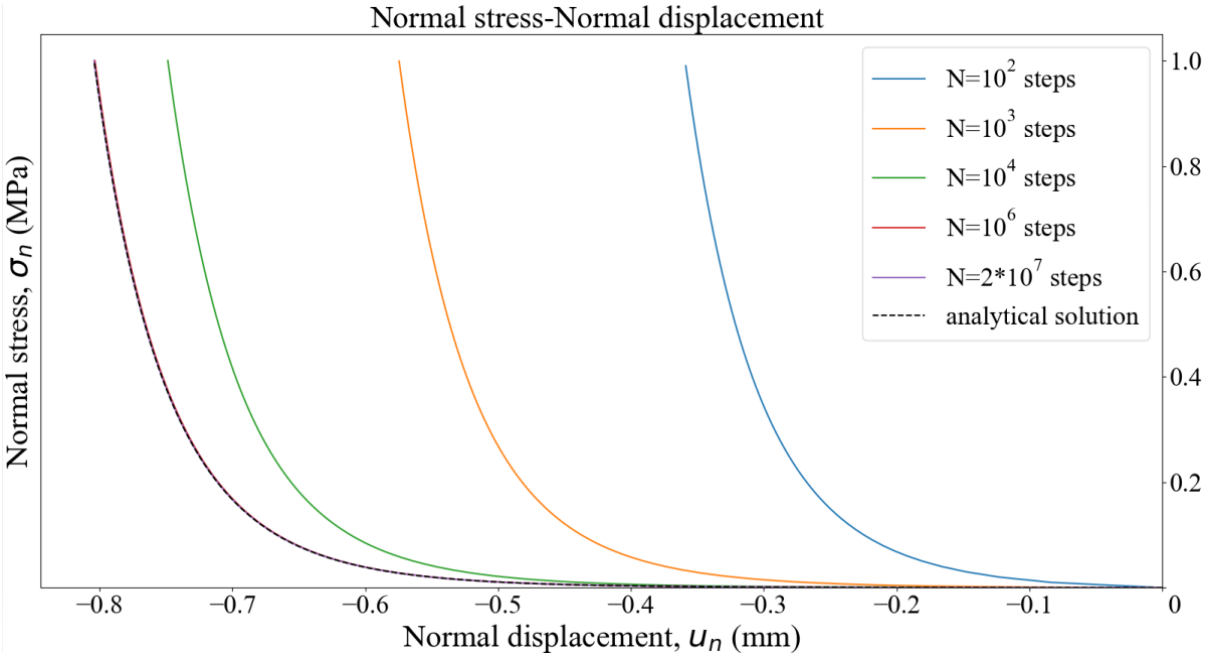

Figure 3.7: Normal Displacement vs Normal Stress for a different number of steps using the perfect elasto-plastic Coulomb with power nonlinear stiffnesses

Simulation of direct shear test under CNL conditions

Considering that the shearing phase is executed under CNL conditions and that the reported Equation (3.51) denotes that the shear stiffness is expressed as a function of the applied normal stress, it can be noted that the value of shear stiffness is constant. Thus, a constant value of shear stiffness equal to the selected value of the previous shear simulations was adopted. Therefore, the process followed as well as the obtained results of the simulation of the direct shear test under CNL conditions were the same as those presented in Section 3.4.2.

3.4.3.2 Hyperbolic function

Furthermore, as stated in Section 2.4, Barton suggested a hyperbolic formulation of shear stiffness derived by Kulhawy (1975) (Equation 2.35). However, the suggested hyperbolic function was not adopted by the presented model because of its complexity during the implementation phase of the FE algorithm. More specifically, the complexity of the implementation of this model using an implicit integration algorithm lies in the strong dependence of the value of shear stiffness, on the obtained value of shear stress (for each step of the used integration scheme). This dependency causes convergence issues in the FE algorithm. In addition, the parameters included in the formulation of shear stiffness presented in Equation (2.35) are strongly empirical and their values are difficult to be acquired using standard laboratory tests. Considering these limitations, a linear approximation for the formulation of shear stiffness was employed as follows:

$$k_s = \frac{\tau_{peak}}{u_{s_{peak}}} = \frac{\sigma_n tan\varphi + c}{u_{s_{peak}}} \tag{3.55}$$

Moreover, according to the previous section the considered behavioural model captures the softening behaviour in combination with the Coulomb strength criterion. For this reason, the formulations of the yield function and plastic potential presented in section 3.4.2 (Equations

(3.36) and (3.37)) are also eligible to be used during the formulation process of the required relationships to describe the mechanical behaviour of a discontinuity.

The required parameters for the simulation of the considered two-phased laboratory test adopting the presented constitutive law and their values are illustrated in the table below:

Table 3.4: Required parameters for elastoplastic Coulomb model with linear softening and hyperbolic non-linear stiffnesses

Parameters	Values
$\boldsymbol{c}$	0
$\boldsymbol{c_{res}}$	0
$\boldsymbol{\varphi}$	30°
$\boldsymbol{\varphi_{res}}$	25°
$\boldsymbol{\psi}$	15°
$\boldsymbol{\psi_{res}}$	10°
$\boldsymbol{k_{n_{ini}}}$	18.8 MPa/mm
$\boldsymbol{u_{n_{max}}}$	0.091 mm
$\boldsymbol{u_s^{peak}}$	3.46 mm
$\boldsymbol{Dc}$	2 mm
dilation cut-off	8.95 mm

Simulation of normal compression test

Considering the same conditions for the simulation of a normal compression test as described in Section 3.4.3.1, the formulation of k_n reported in Equation (3.50) was employed to specialised Equation (3.11) through which the occurred normal deformation of each integration step was calculated. Figure 3.8 illustrates the extracted results of this first phase of the simulated laboratory test for several selected calculation steps N.

$$u_{n_{fin}}^{e} - u_{n_{ini}}^{e} = \int_{\sigma_{n_{ini}}}^{\sigma_{n_{fin}}} \frac{d\sigma_n}{k_{n_{ini}}\left(1 - \frac{\sigma_n}{u_{n_{max}} k_{n_{ini}} + \sigma_n}\right)^{-2}} \tag{3.56}$$

The solution of this integral provides the formulation of the analytical solution of the adopted model:

$$u_{n_{fin}} = -u_{n_{max}}{}^{2} k_{ni} \left[(u_{n_{max}} k_{n_{ini}} + \sigma_{n_{kfin}})^{-1} - (u_{n_{max}} k_{n_{ini}} + \sigma_{n_{ini}})^{-1}\right] + u_{n_{ini}} \tag{3.57}$$

The analytical loading curve is shown in Figure 3.8 together with the curves obtained from the implemented solution solved for different incremental steps N. The results confirm the reliability of the implementation. However, as expected (due to the adoption of an explicit integration scheme), the implemented solutions required a relatively high number of steps (approximately N ≥ 1 thousand) for fitting the analytical results.

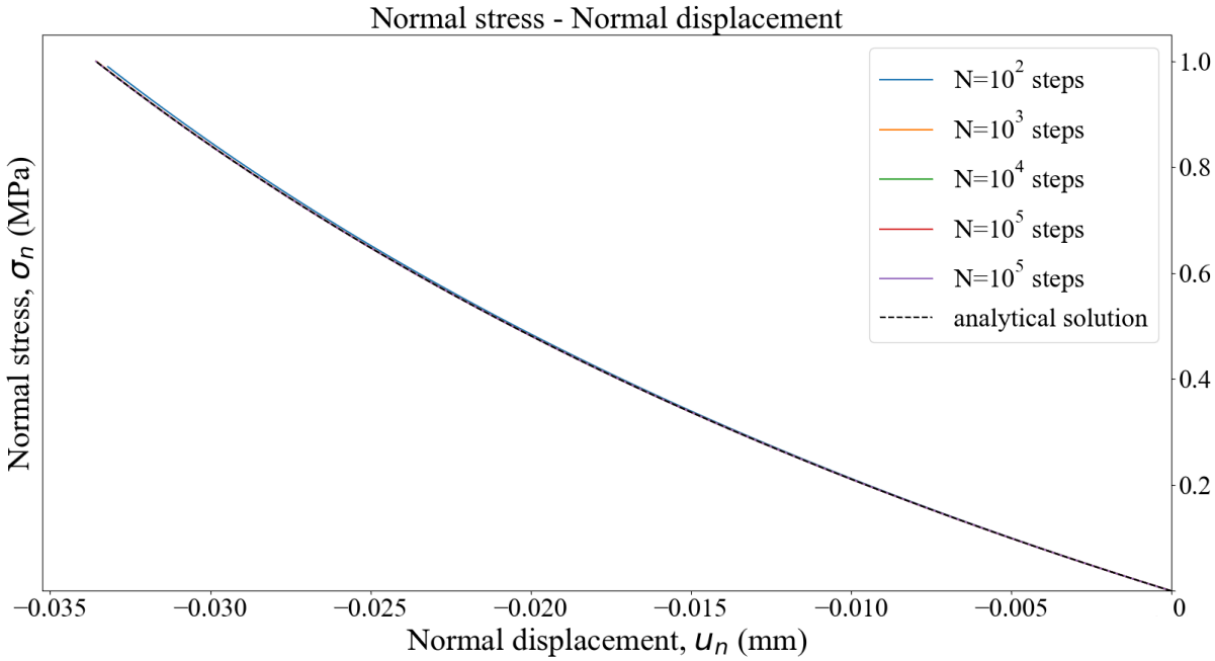

Figure 3.8: Normal Displacement vs Normal Stress for a different number of steps using the perfect elasto-plastic Mohr-Coulomb with hyperbolic nonlinear stiffnesses

Simulation of direct shear test under CNL conditions

It must be pointed out, that in this model also, the value of shear stiffness is constant during the application of shear loading. Moreover, the values of the required parameters are the same as those selected in the simulation of the direct shear test presented in Section 3.4.2. More specifically, the value of the adopted shear stiffness was estimated based on Equation (3.55) as follows:

$$k_s = \frac{\tau_{peak}}{u_{s_{peak}}} = \frac{0.58}{0.058} = 10\ MPa/mm$$

Therefore, the process followed as well as the obtained results of the simulation of direct shear test under CNL conditions were the same as the results presented in Section 3.4.2.

3.5 Modified Barton-Bandis constitutive model

Before the description of the constitutive laws which have been based on the Barton-Bandis model, the yield surface (in the $\tau - \sigma_n$ space) of the considered model must be discussed. Although the empirical BB strength criterion (introduced by Equation 2.26) fits well with experimental data, its numerical implementation requires some mathematical treatments to ensure theoretical rigorousness. It can be seen from Equation (2.26) that the equation loses its validity when σ_n approaches (and exceeds) JCS. The roughness angle i will become negative which is physically incorrect. Mathematically the overall secant friction angle $i + \varphi_r = JRC_{peak}\log_{10}\left(\frac{JCS}{\sigma_n}\right) + \varphi_r$ may be negative when $\sigma_n > JCS$ which is also invalid. Moreover, according to Barton (1973), the BB strength criterion has been suggested for applications in which the expected normal stress levels are within the range of:

$$0.01 < \frac{\sigma_n}{JCS} < 0.3$$

Therefore, in this research project, an open yield surface is adopted, assuming a constant tangent friction angle when $\frac{\sigma_n}{JCS} \geq 1$. This choice is motivated by mathematical validity and convexity of the yield function, as well as the lack of experimental evidence at high normal stress level.

In addition, Equation (2.26) loses its validity when σ_n approaches zero. It should be noted that Barton (1973) suggested that at low-stress levels the value of the friction angle $(\varphi_\mu + i)$, should be considered equal to 70°, and the strength envelop becomes linear without any cohesion in this zone. Although disregarding cohesion and tensile strength might be proven for many rock discontinuity types, it might be a bit too conservative and lead to numerical instability. To improve usage flexibility, the considered yield surface of this research project captures the tensile strength and cohesion of a discontinuity in the low-stress zone.

In more detail, considering the aspects introduced by Barton, the projection of the yield surface started by calculating the cohesion and the friction angle of the yield surface at a low-stress level. Concretely, the low-stress domain is governed by the typical Coulomb model described in Sections 2.4.1 and 3.4.1. This zone is characterized by a cohesion, a friction angle, a dilation angle and a tensile strength (Table 3.5). To ensure numerical stability, the values of these quantities are subject to the following theoretical restrictions.

Although Barton suggested an empirical value of the 'transition friction angle' of 70°, this transition value was defined as a parameter φ_{Tr}. Considering Equation (2.25) and that at low normal stress, the friction angle should be equal to φ_{Tr}:

$$JRC_{peak}\log_{10}\left(\frac{JCS}{\sigma_n}\right) + \varphi_r \leq \varphi_{Tr} \tag{3.58}$$

the value of the normal stress at the transition was calculated:

$$\sigma_{n,Tr} = 10^{(\log_{10}(JCS)-(\varphi_{Tr}-\varphi_r)/JRC_{peak})} \tag{3.59}$$

Moreover, the value of the shear stress which corresponds to the calculated normal stress was executed using the following relationship:

$$\tau_{Tr} = \sigma_{n,Tr} tan(\varphi_{Tr}) \tag{3.60}$$

Projecting this set of coordinates $(\tau - \sigma_n)$ on the yield surface of the Barton-Bandis model an intersection point was created. Using this point, a tangent line to the non-linear shear stress-normal stress behaviour was also projected. The intersection of this line with the axis of the shear stress denotes the value of the cohesion while its inclination indicates the friction angle.

More specifically, the inclination of the tangent line was calculated through the following derivative:

$$\frac{\partial \tau}{\partial \sigma_n} = tan\left(\varphi_r + JRC_{peak}\log_{10}\left(\frac{JCS}{\sigma_{n,Tr}}\right)\right) - \frac{\pi JRC_{peak}}{180 ln(10)}\left[tan^2\left(\varphi_r + JRC_{peak}\log_{10}\left(\frac{JCS}{\sigma_{n,Tr}}\right)\right) + 1\right] \tag{3.61}$$

The value of the tangent friction angle which corresponds to the calculated inclination was determined as follows:

$$\varphi_{tan,Tr} = arctan\left(\frac{\partial \tau}{\partial \sigma_n}\right) \tag{3.62}$$

Furthermore, considering the determined value of the tangent friction angle, the maximum cohesion can be determined to ensure convexity:

$$c_{max} = \tau_{Tr} - \sigma_{n,Tr}\varphi_{tan,Tr} \tag{3.63}$$

The friction angle in the low-stress zone is therefore not a parameter but calculated based on:

$$\varphi = \frac{(\tau_{Tr} - c)}{\sigma_{n,Tr}} \tag{3.64}$$

Finally, it is important to note that at high stress domain (the applied normal stress level is larger than the value of JCS) the original Barton's equation may be invalid as the secant friction angle is reducing. Considering that the yield surface remains open and convex, a tangent line which intersects the non-linear behaviour of shear stress-normal stress at the point which corresponds to a normal stress level equal to the value of JCS was projected. This line describes the shape of the yield surface in the high-stress zone. In this way, a convex yield surface which captures the mechanical behaviour of a discontinuity under both high and low stress levels was introduced.

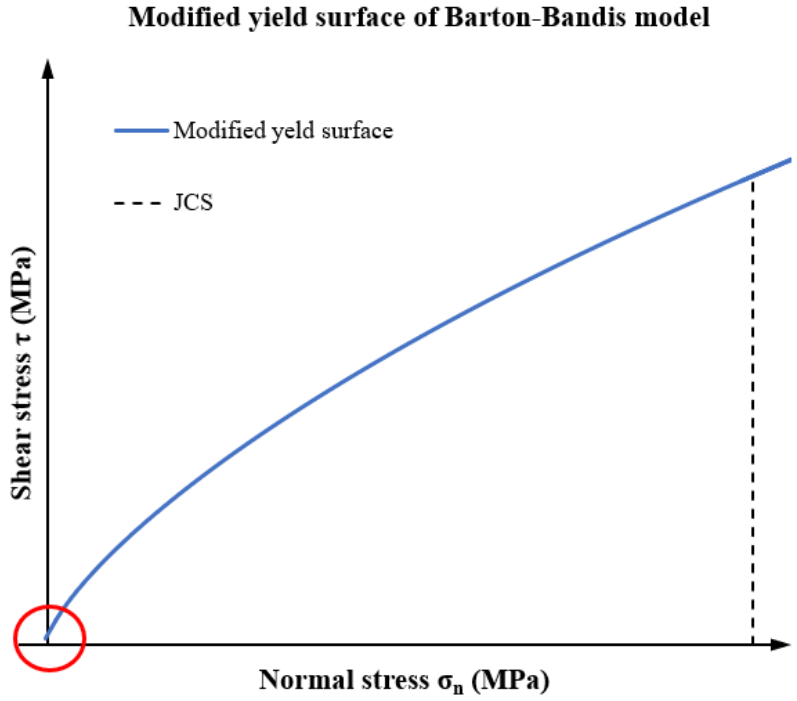

Figure 3.9: Modified yield surface of Barton-Bandis model

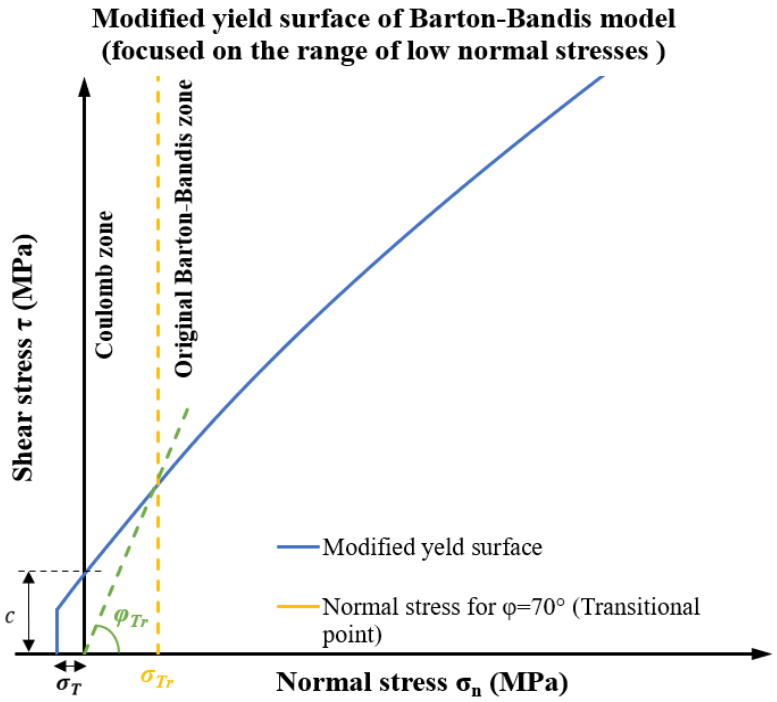

Figure 3.10: Modified yield surface of Barton-Bandis model (focused on low normal stress levels)

Finally, similarly to the previous Section 3.4, the mechanical response of a discontinuity in a limestone (γ = 25 kN/m^3) located at a 40m depth was selected to be theoretically simulated using the considered Python script.

3.5.1 Modified Barton-Bandis model

The fifth set of constitutive relationships describes the mechanical response of a discontinuity within the framework of strain softening. More specifically, the presented constitutive law of this section considers the Barton-Bandis strength criterion and the concept of mobilized roughness.

In more detail, as described in Section 2.4.3 Barton-Bandis model describes the evolution of the shear strength of a rock discontinuity considering that, once the amount of the applied displacement becomes equal to 30% of the total amount of shearing the mobilisation of roughness begins and the phenomenon of dilations is observed. This condition is described with the introduced empirical formulations by Barton (reported also in Section 2.4.3) which make his model highly non-linear and its implementation a challenging process. Therefore considering the high empiricism nature of the evolution of JRC_{mob}, the highly non-linear trend which dictates the mechanical response of a discontinuity and taking into account that the concept of the mobilized roughness is of great importance for the realistic simulation of the mechanical behaviour of a discontinuity under the application of shear displacement, the presented constitutive model considers a reduction factor to linearly reduce the value of the JRC_{peak}. More specifically, the value of the JRC_{peak} was set to be linearly reduced with the value of state parameter κ. However, it should be noted that considering that the value of shear strength is non-linearly dependent on the value of the JRC_{peak} the evolution of shear strength after the linear reduction of roughness should follow a non-linear trend as well. In addition, it must be pointed out that the adopted linear law could lead to a more conservative strength prediction in the post-peak domain compared to the original highly non-linear Barton-Bandis which consequently will lead to an earlier reach of the residual state. Finally, the applied

reduction factor is the same as the one used in Equation (3.44). Thus, in the presented constitutive model the calculation of the value of the mobilized roughness JRC_{mob} is carried out as follows:

$$JRC_{mob} = JRC_{peak}\left(1 - \frac{\kappa}{Dc}\right) \tag{3.65}$$

where κ is the state parameter as it has been introduced by Equation (3.29).

Considering the formulation of the Barton-Bandis strength criterion introduced by Equation (2.26), the modified relationship of the mobilized roughness and that the presented constitutive law is formulated within the framework of strain softening the mathematical formulation of the yield function was written:

$$F(\tau, \kappa) = \tau - \sigma_n \tan\left(JRC_{mob}\log_{10}\left(\frac{JCS}{\sigma_n}\right) + \varphi_r\right) \leq 0 \tag{3.66}$$

A non-associated flow rule is also considered to avoid the overestimation of dilation: once the peak strength is reached the yield function turns to zero and the plastic potential is activated. Thus, considering the formulation of the yield function reported in equation (3.66) and the introduced equation by Barton for the calculation of the peak dilation angle (Equation 2.41), the formulation of the plastic potential is expressed as follows:

$$G(\tau, \kappa) = \tau - \sigma_n \tan\left(\frac{1}{2}JRC_{mob}\log_{10}\left(\frac{JCS}{\sigma_n}\right)\right) \tag{3.67}$$

Considering the applied modifications regarding the shape of the yield surface of the Barton-Bandis model described in Section 3.5 and the introduced formulation of mobilized roughness which leads to the reduction of the strength of the discontinuity, the yield surface which captures the mechanical behaviour of a discontinuity at the residual state under both high and low-stress levels can be introduced as indicated by Figure 3.11 and Figure 3.12. More specifically, it should be pointed out that the shape of the yield surface at the residual state is governed by the same trend as the intact yield surface (at the peak strength). In this case the yield surface is always convex and remains open when the applied normal stress level is larger than the value of JCS. Moreover, in this research project considering the limitation of the Barton-Bandis strength criterion to describe the shear behaviour of a discontinuity at a high-stress level, it is assumed that the yield surface at a stress level higher than JCS stays unchanged during the softening process. This assumption at least allows for a convex yield surface in the entire stress zone at any residual state.

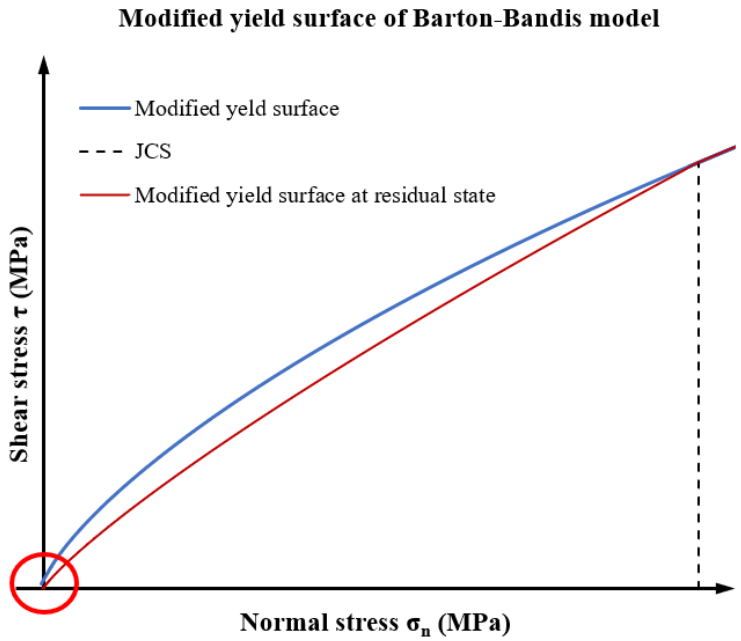

Figure 3.11: Modified yield surface of Barton-Bandis model at peak and residual state

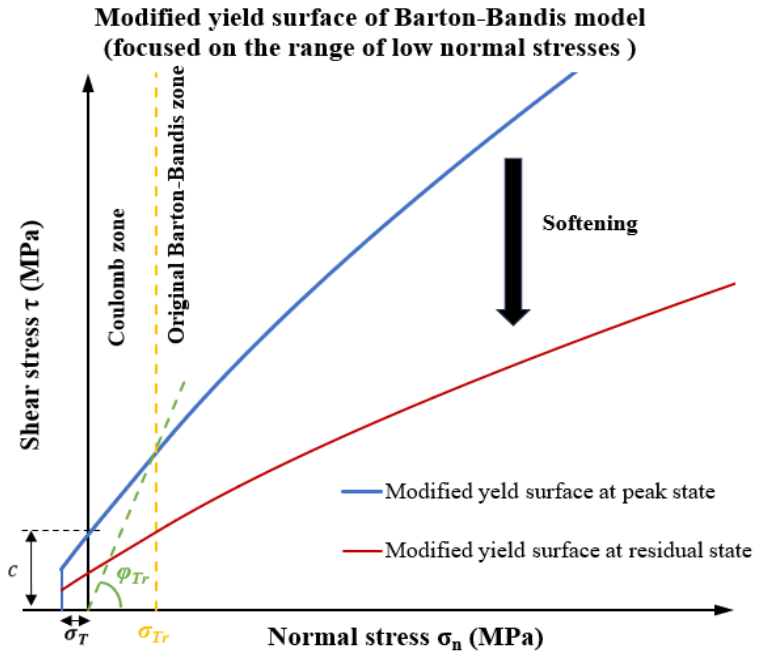

Figure 3.12: Modified yield surface of Barton-Bandis model at peak and residual state (focused on low normal stress levels)

In addition, considering the formulation of JRC_{mob} introduced by Equations (3.65), the evolution of the JRC_{mob} during the application of the shear displacement is calculated as follows:

$$JRC_{mob} = JRC_{peak}, \quad for \ \kappa = 0 \tag{3.68}$$

$$JRC_{mob} = JRC_{peak}\left(1 - \frac{\kappa}{Dc}\right), \quad for \ 0 < \kappa < Dc \tag{3.69}$$

$$JRC_{mob} = 0, \quad for \ \kappa > Dc \tag{3.70}$$

In parallel, the newly introduced cohesion and dilation in the low-stress zone is also reduced with the state variable:

$$c = c_{peak}, \quad for \ \kappa = 0 \tag{3.71}$$

$$c = c_{peak}\left(1 - \frac{\kappa}{Dc}\right), \quad for \ 0 < \kappa < Dc \tag{3.72}$$

$$c = c_{res}, \quad for \ \kappa > Dc \tag{3.73}$$

$$\psi = 0, \quad for \ \kappa = 0 \tag{3.74}$$

$$\psi = \psi_{peak}\left(1 - \frac{\kappa}{Dc}\right), \quad for \ 0 < \kappa < Dc \tag{3.75}$$

$$\psi = \psi_{res}, \quad for \ \kappa > Dc \tag{3.76}$$

In conclusion, it must be stated that the reported equation regarding the evolution of JRC_{mob} denotes that the value of the JRC_{mob} reaches its maximum value when the value of the state parameter is equal to zero. As the value of the state parameter κ, is further increased the value of the mobilized roughness JRC_{mob}, is decreasing which consequently leads to a reduction of the shear strength. Finally, Equation (3.70) renders that at the residual state, all the existing asperities have been sheared off ($JRC_{mob} = 0$) and the shear strength obtains its residual value.

Similar to the previous sections, the derived equations of the modified Barton-Bandis model were implemented in a Python script to simulate a direct shear test under CNL conditions. For the simulation of the considered laboratory test four new parameters must be introduced. In more detail, these four parameters are related to the modifications which were applied in the original version of the Barton-Bandis model regarding the shape of the yield function (described in section 3.5). More specifically, the newly added parameters concern the area of the yield surface which corresponds to low-stress levels. Table 3.5 indicates the four new parameters which were adjusted to the implemented version of the Barton-Bandis model:

Table 3.5: Four newly added parameters of the Barton-Bandis model with linear reduction of roughness

Parameters	Description
Transitional friction angle, φ_{Tr}	The value of friction angle at low-stress levels is equal to 70° as suggested by Barton (1973)
Cohesion, c	The value of cohesion at low-stress levels (calculated using derived Equation (3.63))
Dilation angle at low-stress levels, ψ_{LS}	The value of the dilation angle at low-stress levels (its value should be larger than the value which corresponds to a higher stress level)
Tensile strength, σ_T	The tensile strength of a discontinuity is very low or equal to zero

Having introduced the four new parameters of the Barton-Bandis model with linear reduction of roughness, the required parameters for the simulation of the considered two-phased laboratory test adopting the presented constitutive law and their values are illustrated in the table below:

Table 3.6: Required parameters for the Barton-Bandis model with linear reduction of roughness

Parameters	Values
$\boldsymbol{\varphi_{Tr}}$	70°
$\boldsymbol{c}$	20
$\boldsymbol{\psi_{LS}}$	30°
$\boldsymbol{\sigma_T}$	0
$\boldsymbol{\varphi_{res}}$	20°
$\boldsymbol{JRC}$	15
$\boldsymbol{JCS}$	100 MPa
$\boldsymbol{k_n}$	18.8 Mpa/mm
$\boldsymbol{k_s}$	10 Mpa/mm
$\boldsymbol{Dc}$	9 mm
dilation cut-off	0 mm

The final feature of the considered model which should be discussed is related to the dilation cut-off. As it can be observed in Table 3.6 the value of this parameter has been set equal to zero. The reason behind this selection lies in the fact that according to the Barton-Bandis model, the dilation is eliminated once the existing asperities within the walls of the discontinuity have been sheared off. As was stated before the entire degradation of the asperities is completed at the residual state (after the application of 9 mm of shear displacement) in which the value of the mobilized roughness JRC_{mob}, is equal to zero.

Simulation of normal compression test

Considering that in this model also, the normal stiffness has been employed as a constant parameter and the same values of the required parameters have been adopted as those in the model presented in Section 3.4.1, identical results to those shown in Figure 3.1 are obtained for the simulation of the normal compression test.

Simulation of direct shear test under CNL conditions

Similarly, to the previous sections, the simulation of the direct shear test under CNL conditions assumes that the final compression level of the previous phase ($\sigma_n = 1\ MPa$) is now kept constant while a shear displacement $u_s = 10\ mm$ is incrementally applied. For the simulation of the direct shear test ten thousand integration steps were considered.

Moreover, accordingly, with the perfect elastoplastic Coulomb model presented in Section 2, the calculation of applied shear stress was executed based on Equation (3.19) while for the calculation of the correction factor $d\tau^p$ the derived Equation (3.24) was used. In addition, the values of both plastic multiplier and generated plastic normal deformations were obtained through Equations (3.27) and (3.28) respectively.

However, considering that in this model the formulations of both yield function and plastic potential have been changed compared to the introduced model in Section 2 the values of the values of the presented derivatives in the introduced equations were recalculated as follows:

$$\frac{\partial F}{\partial \tau} = \frac{\tau - \sigma_n tan\left(\varphi_r + JRC_{mob}\log_{10}\left(\frac{JCS}{\sigma_n}\right)\right)}{\partial \tau} = 1 \tag{3.77}$$

$$\frac{\partial G}{\partial \tau} = \frac{\tau - \sigma_n \tan\left(\frac{1}{2}JRC_{mob}\log_{10}\left(\frac{JCS}{\sigma_n}\right)\right)}{\partial \tau} = 1 \tag{3.78}$$

$$\frac{\partial G}{\partial \sigma_n} = \tan\psi \Rightarrow$$

$$\frac{\partial G}{\partial \sigma_n} = \tan\left(\frac{1}{2}JRC_{mob}\log_{10}\left(\frac{JCS}{\sigma_n}\right)\right) \tag{3.79}$$

Figure 3.13 and Figure 3.14 show the results obtained from the simulation of the direct shear test.

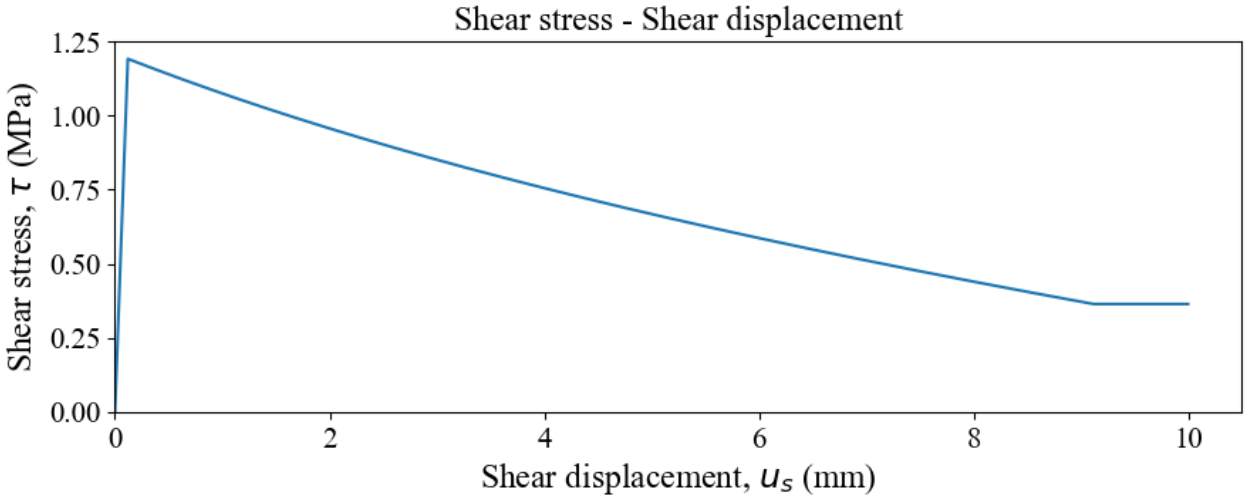

Figure 3.13: Shear displacement vs Shear stress using the modified Barton-Bandis model

Similarly, to the previous sections, the reliability of the exported result presented in Figure 3.13 is assessed by verifying the shear stress once the peak is reached complies with the value obtained from the expression of the adopted constitutive relation:

$$\tau_{peak} = \sigma_n tan\left(JRC_{peak} log_{10}\left(\frac{JCS}{\sigma_n}\right) + \varphi_r\right) =$$

$$1\tan\left(15\log_{10}\left(\frac{100}{1}\right) + 20°\right) = 1.19 \text{ MPa}$$

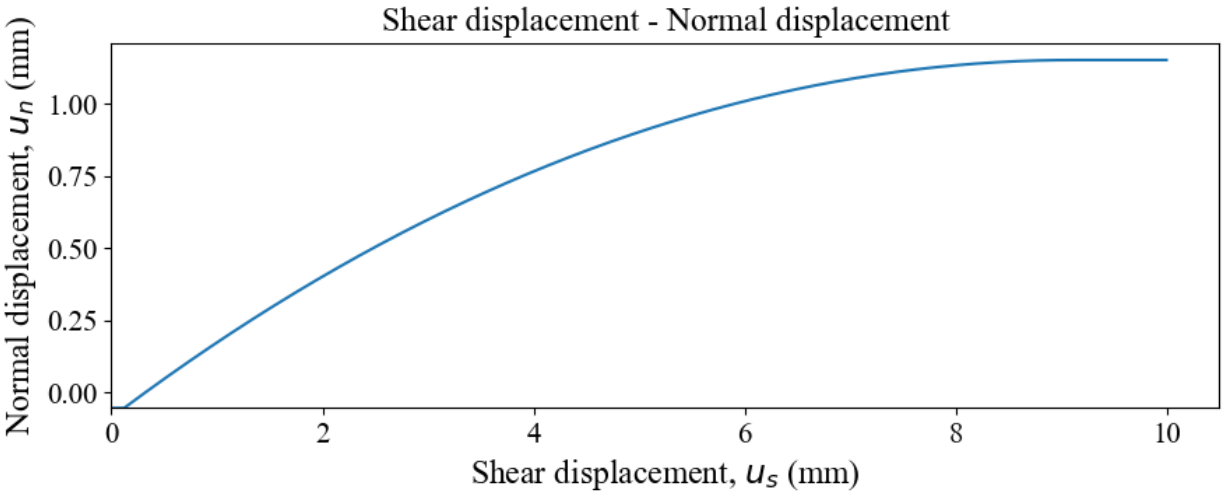

Figure 3.14: Shear displacement vs Normal displacement using the modified Barton-Bandis model

The phenomenon of dilation which is associated with the mechanical behaviour of a discontinuity subjecting to shearing, is illustrated in Figure 3.14. The obtained peak value of dilation is equal to 1.15 mm. Accordingly, to the previous shear simulations, two key features were used to confirm the reliability of the extracted results. Firstly, it is verified that the dilation onsets once the peak shear stress has been reached (at the same amount of shear displacement). Finally, the next feature that was employed for the assessment of the results was the amount of shear displacement further which no dilation is observed. The obtained results illustrated in Figure 3.14 indicate that the dilation is eliminated once the residual state is reached. More specifically as denoted by the exported results the dilation reaches a plateau when the value of the applied shear displacement is equal to 9 mm.

3.5.2 Perfect elastoplastic Barton-Bandis model with hyperbolic stiffness

The last set of constitutive relationships considers the Barton-Bandis strength criterion associated with a hyperbolic function to describe the normal stiffness. On the other hand, the shear stiffness was considered to be dependent on the peak shear stress and the amount of shear displacement that is required to be applied to reach this peak (as described by introduced Equation (3.55).

Considering that this model also adopts the Barton-Bandis strength criterion, the formulation of both the yield function and plastic potential is obtained by the reported Equations (3.66) and (3.67) respectively. The required parameters for the simulation of the considered two-phased laboratory test adopting the presented constitutive law and their values are illustrated in the table below:

Table 3.7: Required parameters for the perfect elastoplastic Barton-Bandis model with hyperbolic stiffness

Parameters	Values
$\boldsymbol{c}$	0
$\boldsymbol{\varphi_r}$	30°
$\boldsymbol{JRC_{peak}}$	15
$\boldsymbol{JCS}$	100 MPa
$\boldsymbol{k_n}$	18.8 MPa/mm
$\boldsymbol{k_s}$	10 MPa/mm
$\boldsymbol{u_{n_{max}}}$	0.091 mm
$\boldsymbol{u_s^{peak}}$	0.058 mm
dilation cut-off	8.95 mm

Simulation of normal compression test

Because the same hyperbolic normal stiffness adopted in the constitutive configuration described in the previous Section 3.4.3.2 is employed here (with the same values for the required parameters), identical results to those shown in Section 3.4.3.2 are obtained for this scenario.

Simulation of direct shear test under CNL conditions

The formulations introduced in Section 2.5 were adopted by the presented behavioural model by just specialized them by replacing the constant value of shear stiffness with the formulation reported by Equation (3.55). Considering that the value of the required amount of shear displacement to reach the peak shear stress, u_s^{peak}, was set equal to 0.058 mm the value of shear stiffness was calculated as follows:

$$k_s = \frac{\tau_{peak}}{u_{s_{peak}}} = \frac{0.58}{0.058} = 10\ MPa/mm$$

Thus, observing also Table 3.6 and Table 3.7 it can be noted that the adopted behavioural model has the same values of the required parameters as the perfect elastoplastic Barton-Badis model presented in Section 2.5. For this reason and considering that because of CNL conditions the difference in the formulations of normal stiffness was not affecting the mechanical response, identical results to those shown in Section 2.5 were also obtained for this simulation.

4 Discontinuity network generation tool for PLAXIS 2D

4.1 Introduction

Finite element methods can be successfully used for advanced numerical analysis involving fractured rock masses. However, the manual creation of a discontinuity network may be a complex and time-consuming task which limits the usage of numerical modelling in practical rock engineering. For this reason, a tool that allows for the automatic generation of realistic discontinuity patterns has been developed for PLAXIS 2D, by means of the PLAXIS Python scripting API. In more detail, the tool can automatically generate multiple discontinuity sets of both persistent and non-persistent discontinuities.

The developments have started during prior research activities. Both the existing and newly developed functionalities will be described in this chapter. The tool is then applied in the case of a FE model of an underground excavation in a fractured rock mass.

4.2 Geometrical characteristics of a discontinuity

The study of a discontinuity in an observed outcrop on the field contains some major measurements. The discontinuity planes in space are mainly characterised by two parameters:

1) Dip: angle between the studied discontinuity plane and the horizontal plane (from 0 to 90 degrees)

2) Dip Direction or Azimuth: angle between the studied plane and the true North (measuring clockwise from the north)

Both Dip and Dip Direction are referring to the line of the steepest declination in the plane of the discontinuity. These two angles are very useful for understanding how the discontinuity planes are distributed in 3D space. However, when representing the discontinuities in 2D, the plane of each discontinuity is represented by its trace. Therefore, five geometrical characteristics must be considered for the representation of a discontinuity in 2D space.

1) Trace Length (TL): length of the discontinuity projected on a representative two-dimensional plane (e.g., as inferred in an outcrop).

2) Plunge: the inclination of the feature relative to the horizontal plane for the projection of discontinuity in the 2D space. If the plunge is measured downward then it takes positive values while if it is measured upward (counter-clockwise) it takes negative values.

3) Persistence Ratio (PR): calculated as a function of the trace length of the single discontinuity, TL, i, and the rock bridge, RB (described below) according to the following formula:

$$PR = \frac{TL,i}{TL,i + RB,i} \tag{4.1}$$

It should be noted that when the value of the Persistence Ratio is equal to one, a fully persistent discontinuity is considered along the rock mass while, as its value becomes lower than one, the persistence starts to decrease. According to many researchers in the field of rock mechanics, discontinuity persistence is one of the most significant rock mass properties but at the same

time is one the most difficult to determine. The persistence of discontinuities has a major influence on the shear strength developed in the plane of the discontinuity.

4) Rock Bridge (RB): portion of intact rock (in units of length) which separates two in-plane discontinuity traces. Rock bridges occur at a number of different scales. It is important to underline the fact that the less the value of the rock bridge the more persistent the studied discontinuity is. The calculation of the value of Rock Bridge can be performed using the formula below:

$$RB = \frac{TL * (1 - PR)}{PR} \tag{4.2}$$

5) Discontinuity trace pole: point in the middle of the trace length. Based on its coordinates and knowing also the trace length and the orientation of the considered discontinuity, it is possible to project easily each trace for the whole domain.

The above-mentioned parameters for the representation of discontinuities in 2D space are depicted clearly in Figure 4.1:

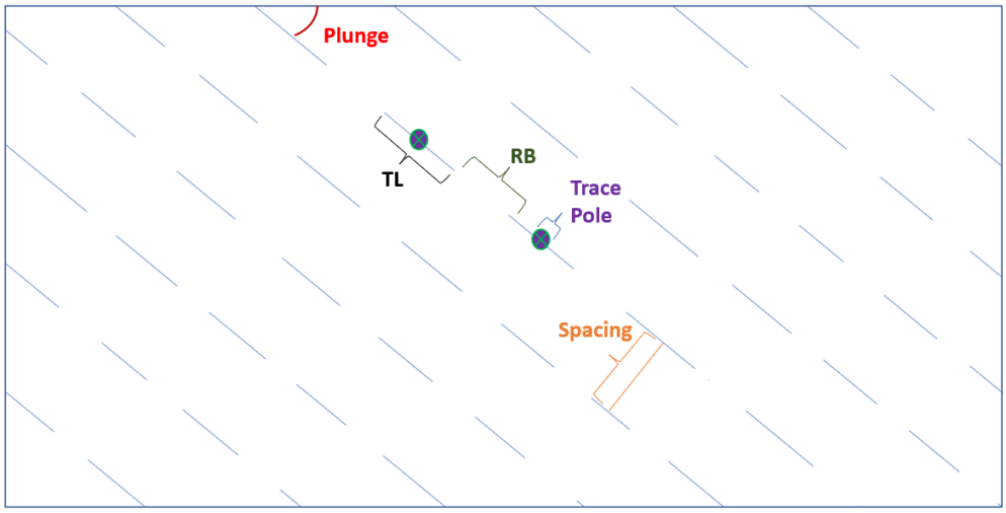

Figure 4.1: Illustration of the required parameters for the projection of the traces (depicted on a randomly generated domain)

4.3 A tool for the generation of discontinuity networks

The tool has been developed in Python and generates one or multiple sets of discontinuities based on the user input.

First, the remote scripting server must be activated by going to the Expert menu and selecting the Configure remote scripting server option. The corresponding window pops up and the server can be started on an available port (Figure 4.2).

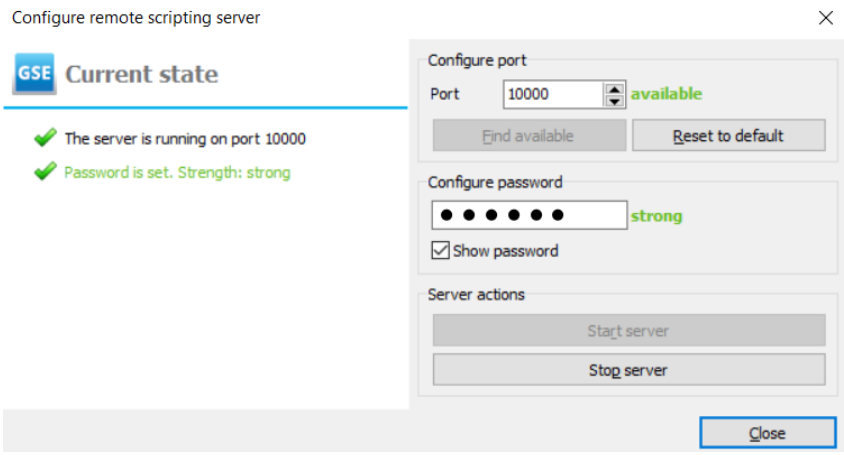

Figure 4.2: Window of Configure remote scripting server option in PLAXIS 2D

It is possible to either assign the coordinates of a rectangular polygon to be drawn in PLAXIS 2D or to load an existing project and indicate the name of the polygon inside which the discontinuity sets will be generated. Each discontinuity set is described by a certain number of input parameters. A summary of the modelling choices available in the tool is presented in Table 4.1:

Table 4.1: Functionalities of the tool for the automatic generation of discontinuity networks

	Persistent discontinuity sets		**Non-persistent discontinuity sets**	
Parameters	Constant spacing	Variable spacing	Constant trace length	Variable trace length
Plunge	**X**	**X**	**X**	**X**
Trace length	**X**	**X**	**X**	**X**
Spacing	**X**	**X**	**X**	**X**
Spacing variation	**-**	**X**	**-**	**-**
PR ratio	**-**	**-**	**X**	**X**
Trace variation	**-**	**-**	**-**	**X**

Multiple sets of discontinuities can be assigned to the same polygon. Table 4.2 presents the required parameters for the projection of two persistent discontinuity sets while the extracted results are illustrated in Figure 4.3.

Table 4.2: Required parameters for the projection of two persistent discontinuity sets

Discontinuity set	**1st set**	**2nd set**
Plunge	30°	-45°
Trace length	40 m	40 m
Spacing	2 m	1.5 m
Spacing Variation	0.5	0.5

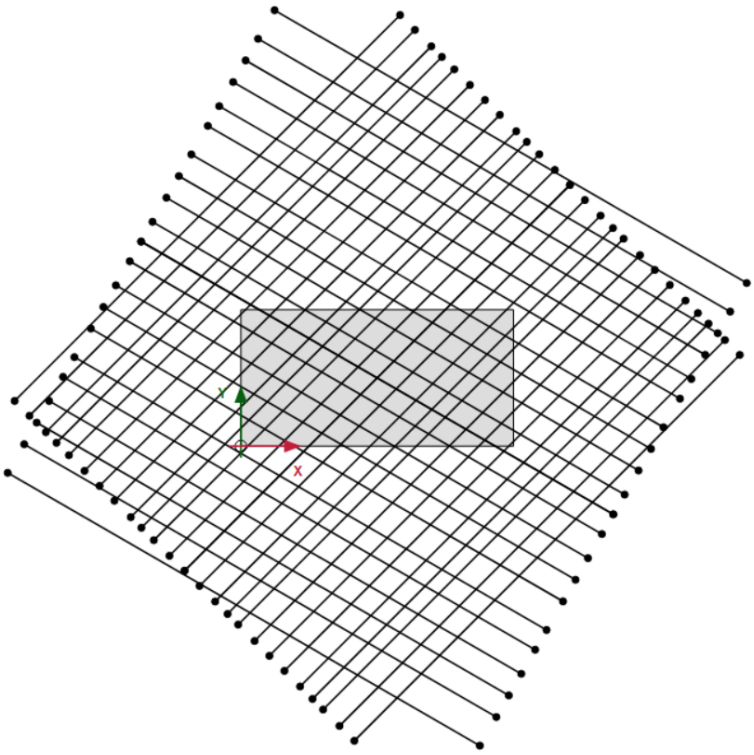

Figure 4.3: Modelling of two persistent discontinuity sets

Table 4.3 presents the required parameters for the projection of a discontinuity network consisting of two non-persistent discontinuity sets. It must be pointed out, that in contrast to the previous example in which the spacing between the discontinuity traces was varying, in the considered network the length of the traces of both sets was selected to be varied. Furthermore, considering that the projected discontinuity sets are non-persistent a value which describes the Persistence Ratio of the considered sets was introduced as an input. The obtained results are illustrated in Table 4.3.

Table 4.3: Required parameters for the projection of two non-persistent discontinuity sets

Discontinuity set	1st set	2nd set
Plunge	15°	-45°
Mean trace length	4 m	3 m
Trace length variation	0.5	0.3
Spacing	1.5 m	2 m
PR	0.5	0.7

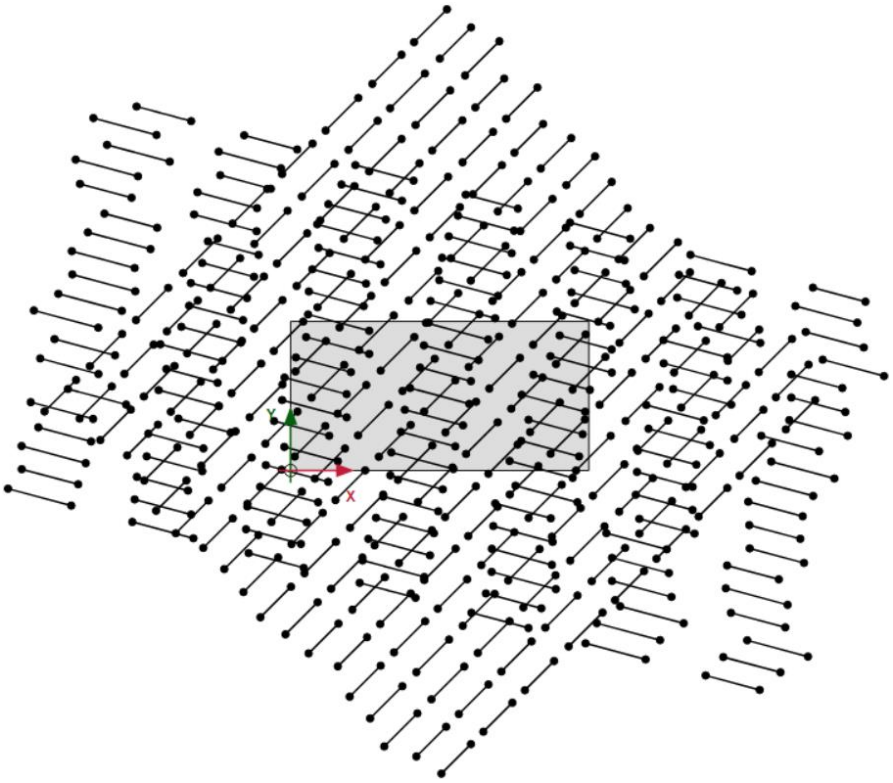

Figure 4.4: Modelling of two non-persistent discontinuity sets

The results (Figure 4.4 and Figure 4.4) show that the tool can project automatically and consistently both persistent and non-persistent discontinuity networks. However, many discontinuities lie either completely outside of the domain or cross the polygon boundary. In the first case, the reason is related to the fact that the number of the generated traces is hard coded and set to an arbitrarily high value to ensure that the domain of interest is fully covered. This means that more time is required to complete the projection process and that, manual work is necessary at the end to delete the numerous traces which are located outside of the boundaries of the considered polygon. In the other case, the user needs to manually generate an intersection point between the discontinuity line and the polygon boundary, delete the original line and the point outside the domain and draw a new one between the two remaining points. This is also a very time-consuming process, especially in the case of large and complex domains.

Further work during this research aimed at improving the efficiency of the tool and automating as much as possible the processes of discontinuity generation and intersection.

4.4 Extended version of the tool for the generation of discontinuity networks

Considering the limitations of the existing version of the tool for the generation of discontinuity networks described in the previous section, improvements were introduced and adjusted to the tool to enhance its efficiency.

The first step consists in estimating the number of traces required to cover the area of the selected polygon. The calculation of the number of the required traces is based on the length of the main diagonal of the considered polygon and the input values of spacing and spacing variation if specified. Note that only polygons with a rectangular or squared shape are considered and that the starting point for the generation of the discontinuities is in the center of

the polygon. Therefore, the number of discontinuities (for each side with respect to the initial point) is automatically calculated as indicated in Equation (4.3):

$$required\ number\ of\ discontinuities = \frac{(length\ of\ main\ diagonal/2)}{(spacing + spacing\ variation)} \qquad (4.3)$$

After generating the set, all the discontinuities that are completely outside of the domain are deleted, while the ones that are partially outside are automatically trimmed. In fact, the tool intersects each line with the polygon and, when no points are generated, the script files a command to delete the line, otherwise it deletes the line and regenerates a new one based on the input values of the required parameters (plunge, spacing etc.) and the corresponding intersection point/s.

Figure 4.5 illustrates the obtained results considering the input values introduced by Table 4.2 and the new functionalities of the extended version of the discussed tool.

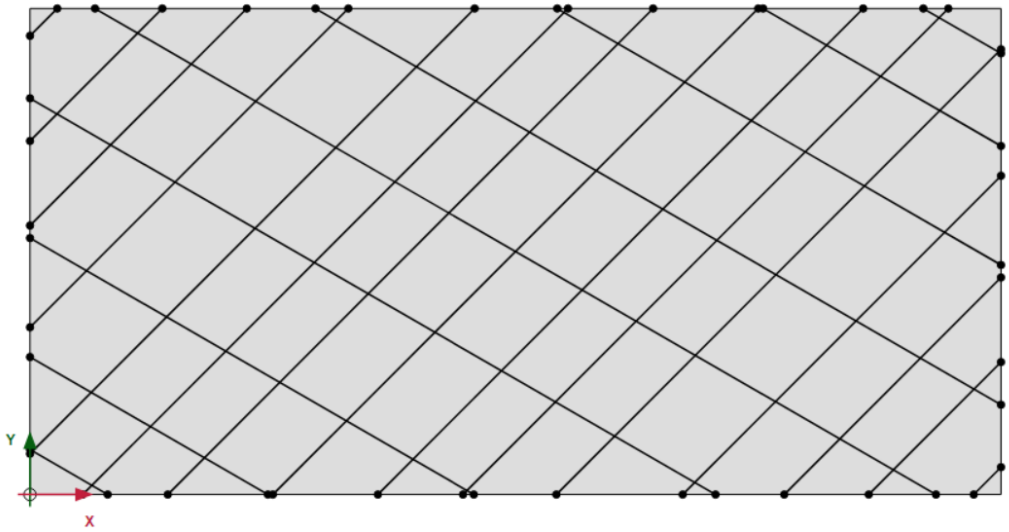

Figure 4.5: Modelling of two persistent discontinuity sets using the extended version of the tool

Finally, considering that in the last part of this research project the efficiency of the constitutive laws introduced in Chapter 3, will be tested in an underground excavation application in a fractured rock mass consisting of persistent discontinuity sets, the capabilities of the tool were verified by automatically projecting a discontinuity network of persistent discontinuities in the created FE model.

The properties of the generated discontinuity sets are the same as those presented in Table 4.2 with the only difference that a trace length equal to 100 m was adopted to ensure that the generated discontinuities have sufficient length to cover even the larger dimension of the considered polygon. Figure 4.6 presents the obtained results using the extended version of the tool.

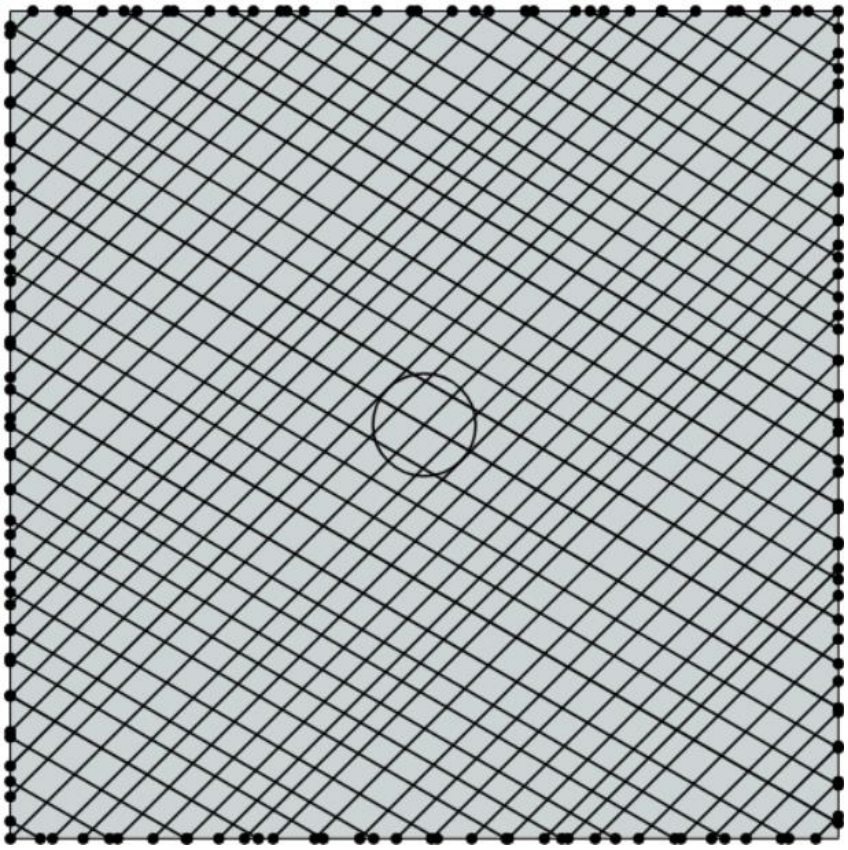

Figure 4.6: Example of the geometry of an underground excavation in a fractured rock mass

5 Verification of the implemented models: CNL test simulations

5.1 Introduction

The numerical implementations of the elastoplastic with linear softening Coulomb model and the modified Barton-Bandis model were carried out in the finite element software PLAXIS by members of the PLAXIS research team. Considering the complexity of the numerical implementation this project focused on the first step of the implementation which considers only linear shear and normal stiffness. Treatment of nonlinear stiffness models will be carried out in future work.

In this chapter, the finite element implementation is verified by simulating direct shear tests under CNL conditions using a simple numerical model in PLAXIS 2D. The simulations were carried out by employing the same sets of parameters used for the theoretical simulation of the mechanical response of a single discontinuity reported in Chapter 3. A comparison between the obtained numerical results and theoretical simulations (as described in Chapter 3) is conducted to verify the correctness of the numerical implementation. In some cases, where experimental results are also available for parameter calibration, comparisons are also made with experimental data to validate the accuracy of the implementation.

5.2 Simulation of Direct Shear test under CNL conditions in PLAXIS 2D

The validity of the numerical implementation of the considered constitutive laws was assessed by simulating in PLAXIS 2D the same two-phased laboratory test as the one described in Chapter 3 (a normal compression test followed by a direct shear test where the loading level in the normal direction reached at the end of the compression phase is kept constant).

Model configuration and material properties

The simulation of the considered laboratory test was performed using a simple numerical model of two rock blocks and a single discontinuity. The geometry of the created numerical model is shown in Figure 5.1.

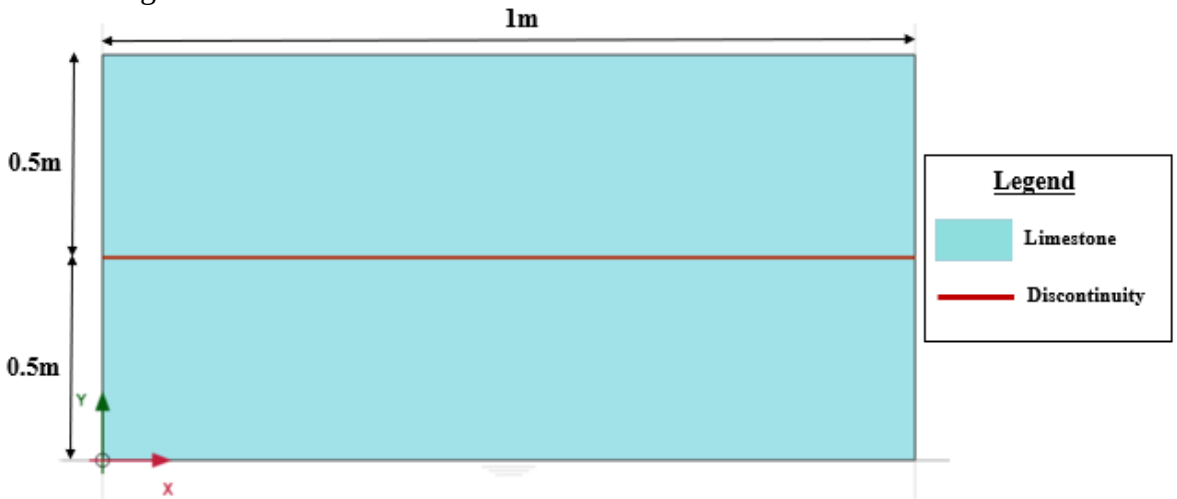

Figure 5.1: Created numerical model for the simulation of the two-phased laboratory test

Similarly, to the performed theoretical simulations (described in Chapter 3) the examined discontinuity was assumed to be located within the mass of a limestone. However, in the

framework of this simulation, two characteristics of great importance regarding the mechanical properties of the adopted rock material must be noted. Firstly, to ensure that during the simulation of the compression phase, the mechanical response of the discontinuity will not be affected by the mechanical behaviour of the rock blocks, the modelling of these two rock blocks was performed using the linear elastic model. In this way, the mechanical response of the two blocks was assumed to be purely elastic. Secondly, the rock material that was assigned to the two rock blocks was assumed to be zero-weight and very stiff with a value of Poisson's ratio equal to zero to ensure that during the simulation of the considered laboratory test only the mechanical behaviour of the discontinuity is examined. In this way, during the first phase of the laboratory test (compression phase) the upper rock block is deformed elastically by transferring the applied load to the existing discontinuity without having the possibility to deform laterally. Therefore, the generation of stresses at the lateral boundaries of the model which may lead to the misconception of the mechanical response of the discontinuity is avoided. The discussed properties of the adopted rock material are presented in Table 5.1.

Table 5.1: Properties of the rock blocks of the simulated laboratory test

Material	Soil model	E_{ref} (MPa)	Poisson's ratio, ν
Limestone	Linear Elastic	15E6	0

Mesh

In terms of element type and mesh, 15-node triangular elements were used for the simulation of the considered test with smaller elements being adopted in the zones of the model where larger strains were expected (i.e., along the discontinuity). On the other hand, a coarser mesh is adopted in the zones where the smaller strains are expected to develop. Furthermore, it should be stated that the discontinuity was modelled as a discrete zero-thickness 1D element. More specifically, the existing discontinuity element in PLAXIS was employed for the modelling of the created discontinuity. Figure 5.2 illustrates the mesh adopted in the present analysis:

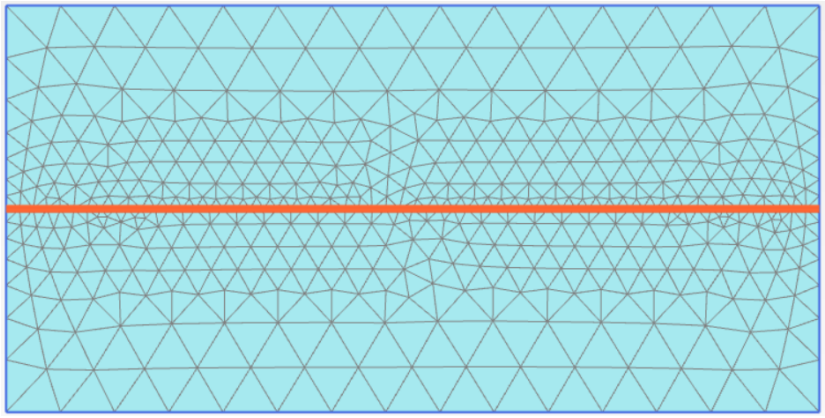

Figure 5.2: Generated mesh for the simulation of the two-phased laboratory test

Having generated the FE model of a direct shear test the corresponding boundary and loading or deformation conditions were applied to each phase as follows:

Compression phase

The test starts with the compression phase. The simulation of this phase was performed considering the lateral boundaries, as well as the lower boundary of the numerical model normally fixed. On the other hand, the upper boundary of the model was simulated as a free boundary on which a linearly distributed load is applied. Figure 5.3 illustrates an example of the deformed mesh at the end of a compression phase as well as the described boundary conditions.

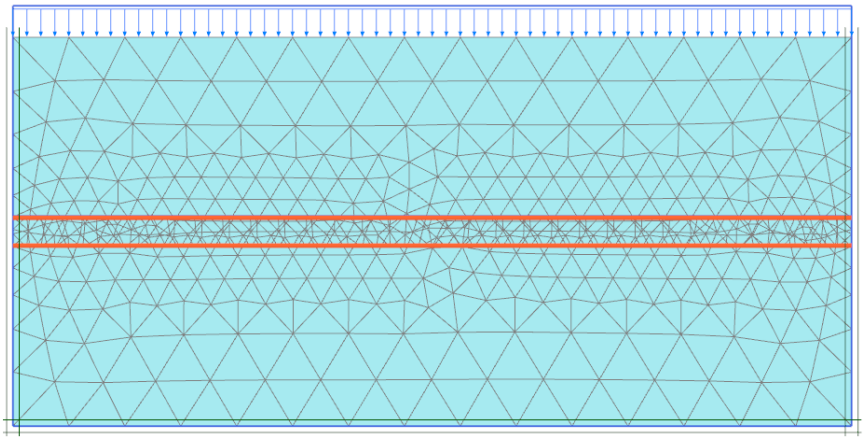

Figure 5.3: Boundary and loading conditions of the compression phase

Shearing phase under CNL conditions

Finally, the last phase of the considered two-phased laboratory test concerns the application of a shear displacement under CNL conditions. For the simulation of this phase, the fixity condition of the model had to be updated. More specifically, the shearing phase was carried out by applying fixities only to the lower boundary of the created model which was normally fixed and on the lateral boundaries which remained fixed to simulate that no lateral deformations of the block are allowed. Furthermore, it should be noted that in this phase the simulation of the CNL conditions was achieved by keeping activated the distributed load which was applied on the upper rock block during the compression phase. Additionally, in combination with the considered load, a uniform prescribed displacement was also applied on the lower block to simulate the application of the shear displacement. Figure 5.4 depicts an example of the deformed mesh at the end of a shearing phase under CNL conditions as well as the adopted boundary conditions.

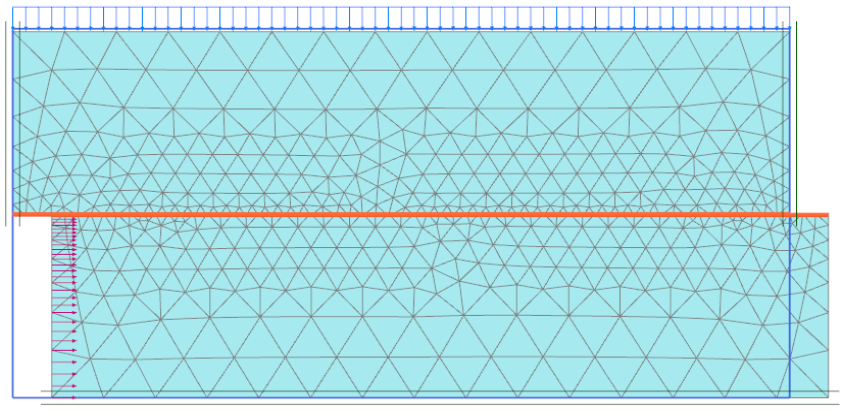

Figure 5.4: Boundary and loading conditions of the shearing phase under CNL conditions

5.3 *Elastoplastic with linear softening Coulomb model*

5.3.1 *Verification of the Elastoplastic with linear softening Coulomb model*

Having created the FE model in PLAXIS 2D, the simulation of the two-phased laboratory test was carried out using the elastoplastic with linear softening Coulomb model. Firstly, the same set of parameters, as those adopted during the theoretical simulation of the same test using the created Python script (presented in Chapter 3) was assigned to the discontinuity. The considered set of parameters is presented in Table 3.2.

The obtained results of the performed simulation using the implemented version of the elastoplastic with linear softening Coulomb model in PLAXIS were compared against the corresponding results of the theoretical simulation presented in Section 3.4.2. In Figure 5.5 and Figure 5.6, the obtained results of shear stress and normal displacement are plotted against the shear displacement.

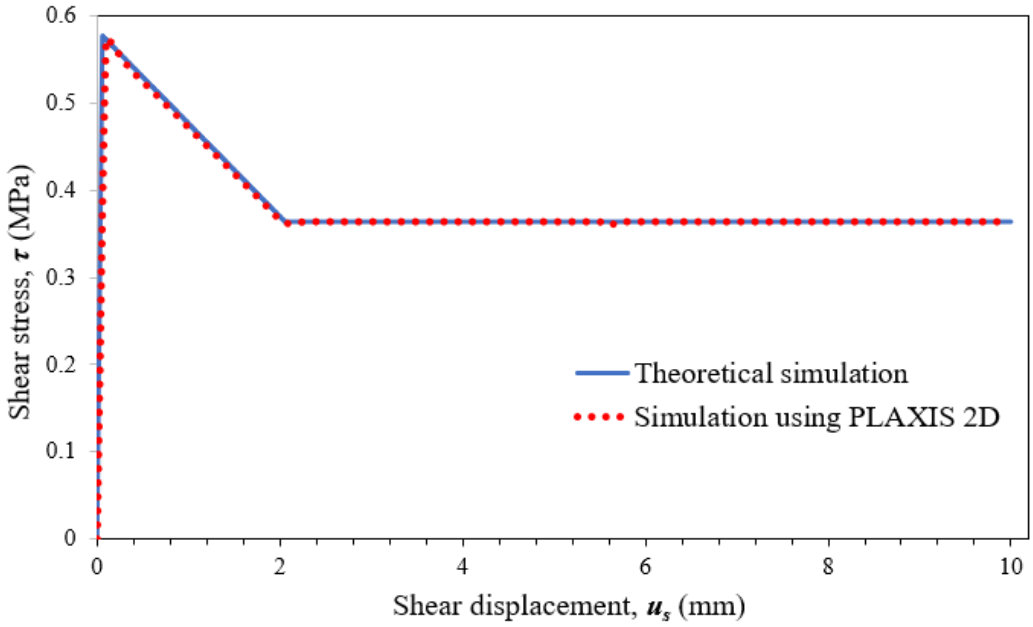

Figure 5.5: Shear displacement vs Shear stress response

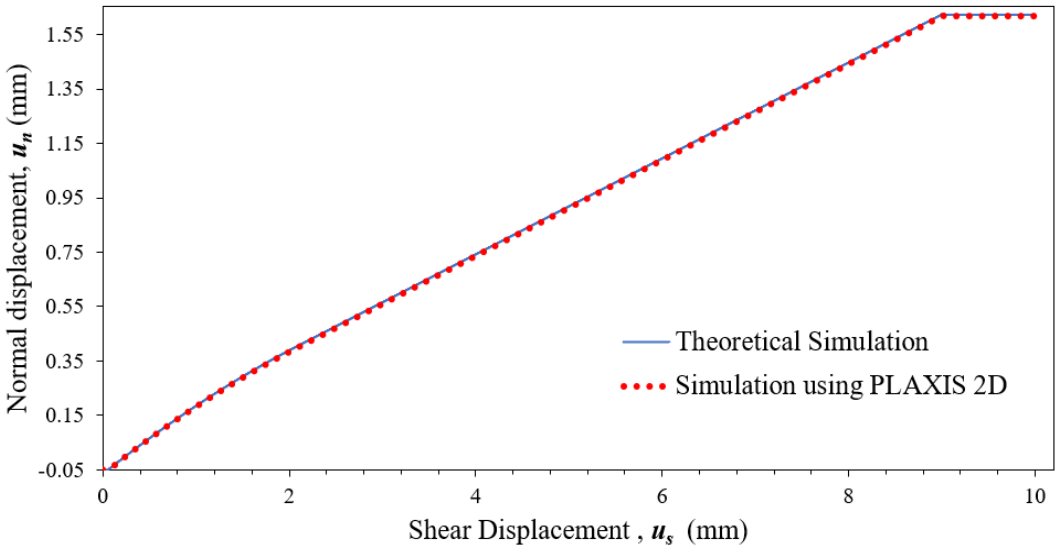

Figure 5.6: Shear displacement vs Normal displacement response

Figure 5.5 and Figure 5.6 confirm the reliability of the numerical implementation by indicating that the obtained results using the implemented version of the elastoplastic with linear softening Coulomb model in PLAXIS comply with the corresponding results of the theoretical simulation.

Having confirmed that the implemented constitutive law can reproduce theoretically the mechanical behaviour of a discontinuity subjecting to shearing under CNL conditions, the model was also verified based on the experimental results reported by Hencher and Richards (2015) who assessed the shear strength of rock discontinuities at the laboratory and field scales. In more detail, having obtained a rock core (andesite) with a tightly interlocking natural discontinuity they performed several direct shear tests under CNL conditions. More specifically, the reported experimental results indicate the evolution of both shear stress and normal deformation of the considered andesite sample under four different normal stress levels while a shear displacement equal to 10 mm is applied. However, considering that only for the normal stress levels of 150 kPa and 300 kPa the reported results indicate clearly all the important features of the mechanical response of the examined discontinuity, the calibration of the parameters of Coulomb with linear softening model was performed based only on the results which correspond to these two normal stress levels.

The experimental tests performed by Hencher and Richards (2015) were simulated employing the implemented version of the elastoplastic with linear softening Coulomb model in PLAXIS 2D. The model parameters and the adopted values are indicated in Table 5.2. Additionally, to further confirm the validity of the numerical implementation the same tests were also simulated theoretically, and the results were plotted. The obtained results are shown in Figure 5.7 and Figure 5.8.

Table 5.2: Parameters of elastoplastic with linear softening Coulomb model for interlocking natural andesite discontinuity

Parameters	Values
$\boldsymbol{c}$	0.005 MPa
$\boldsymbol{c_{res}}$	0.002 Mpa
$\boldsymbol{\varphi}$	60°
$\boldsymbol{\varphi_{res}}$	41°
$\boldsymbol{\psi}$	20°
$\boldsymbol{\psi_{res}}$	7°
$\boldsymbol{k_n}$	18.8 Mpa/mm
$\boldsymbol{k_s}$	0.5 Mpa/mm
$\boldsymbol{Dc}$	3.4 mm
dilation cut-off	4.5 mm

PLAXIS 2D simulation of a direct shear test on andesite discontinuity under CNL conditions (σ_n=150 kPa):

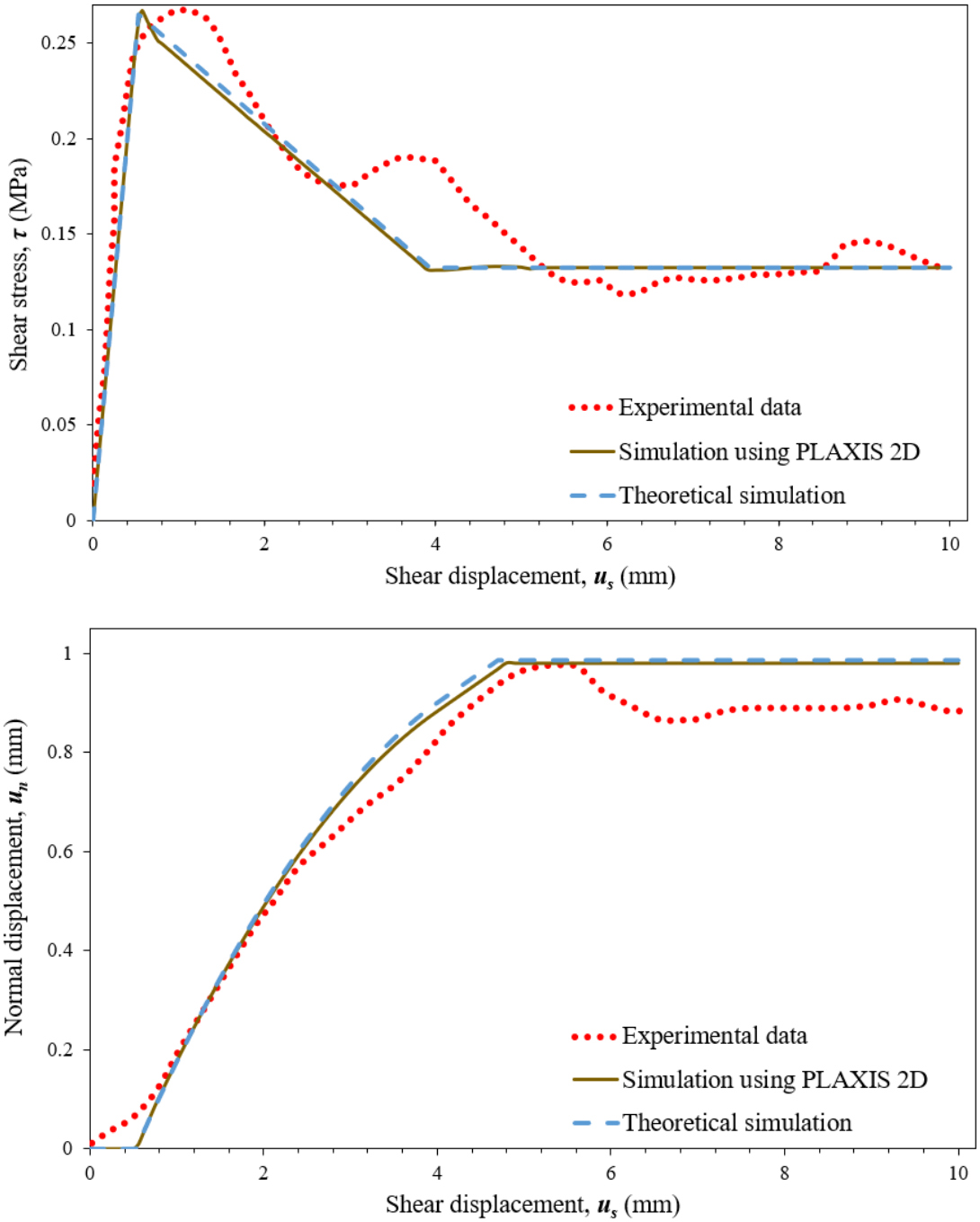

Figure 5.7: Simulation of direct shear test on natural interlocking basalt discontinuity under 150 kPa shear displacement-shear stress (upper) and shear displacement-normal displacement (below)

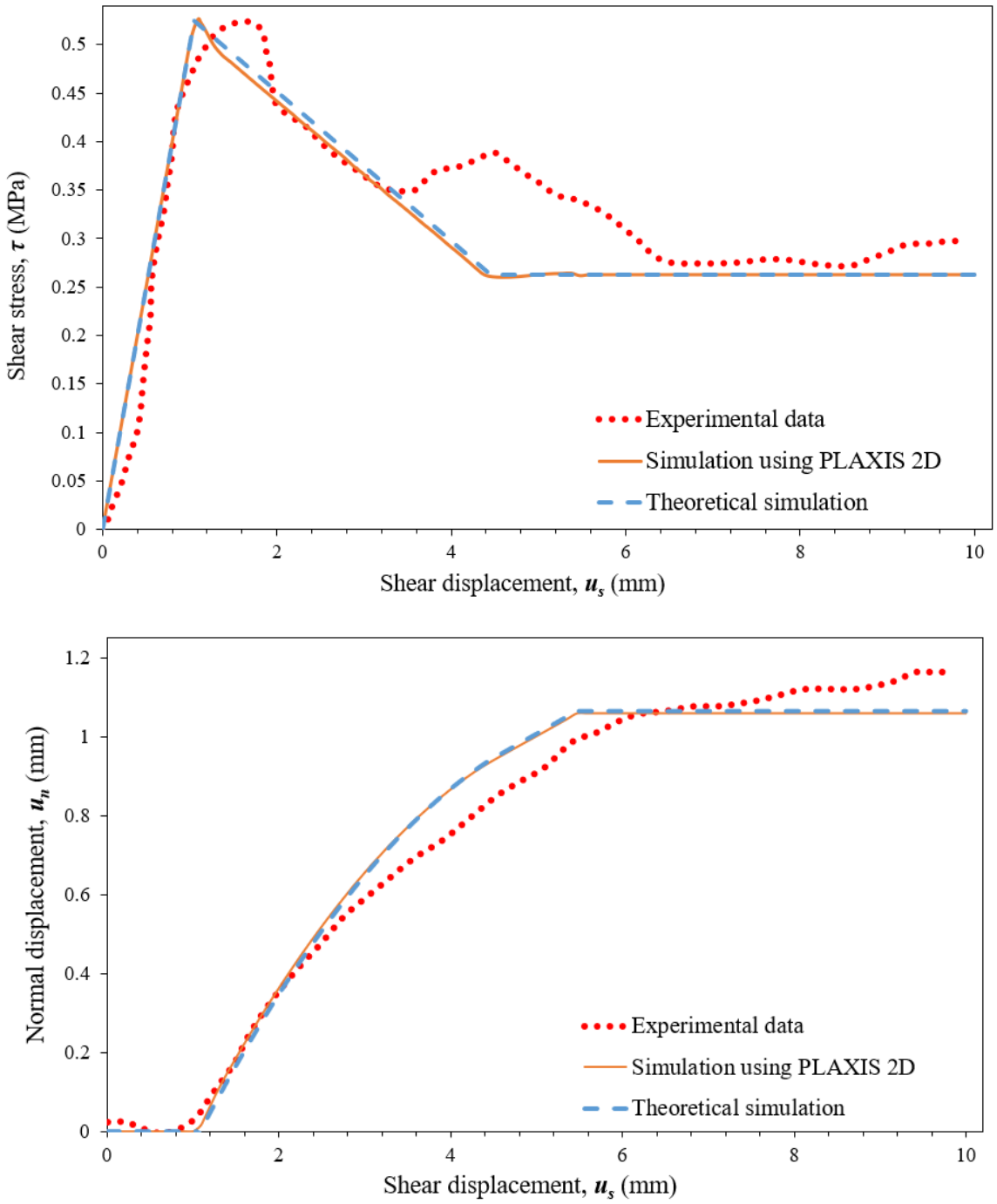

Figure 5.8: Simulation of direct shear test on natural interlocking basalt discontinuity under 300 kPa shear displacement-shear stress (upper) and shear displacement-normal displacement (below)

Figure 5.7 and Figure 5.8 show that the obtained results follow adequately the trend of the mechanical response obtained by Hencher and Richards (2015) by respecting some key features. In more detail, the implemented model represents accurately the peak and the residual strength while also the evolution of shear stiffness. Furthermore, it can be observed that the adopted linear softening provides a fair and safe approximation of the evolution of shear stress at the post-peak area considering that in contrast with the experimentally observed behaviour, the obtained results denote a slight underestimation of the strength after the peak. Additionally, it should be noted that the considered model can reproduce nicely the non-linear evolution of dilation by providing a reasonably accurate and safe estimation as well. Finally, the obtained

results indicate that as expected, the theoretical simulation complies with the response coming from the finite element implementation of the model. In conclusion, the above-mentioned observations suggest that the implementation of elastoplastic with linear softening Coulomb model in PLAXIS 2D has been successful.

5.4 Modified Barton-Bandis model

5.4.1 Verification of the modified Barton-Bandis model

Similarly to what was reported in the previous section, the validity of the numerical implementation of the modified Barton-Bandis was assessed by simulating in PLAXIS 2D the same two-phased laboratory test as the one described in Chapter 3.

The simulation of the considered test was performed using the same numerical model as the one described in section (3.5.1). In addition, the values of the required parameters are the same as those introduced in Table 3.6.

The obtained results of the performed simulation using the implemented version of the modified Barton-Bandis in PLAXIS 2D were compared against the corresponding results of the theoretical simulation presented in Section 3.5.1. Figure 5.9 and Figure 5.10 show the results obtained from the simulation of the direct shear test.

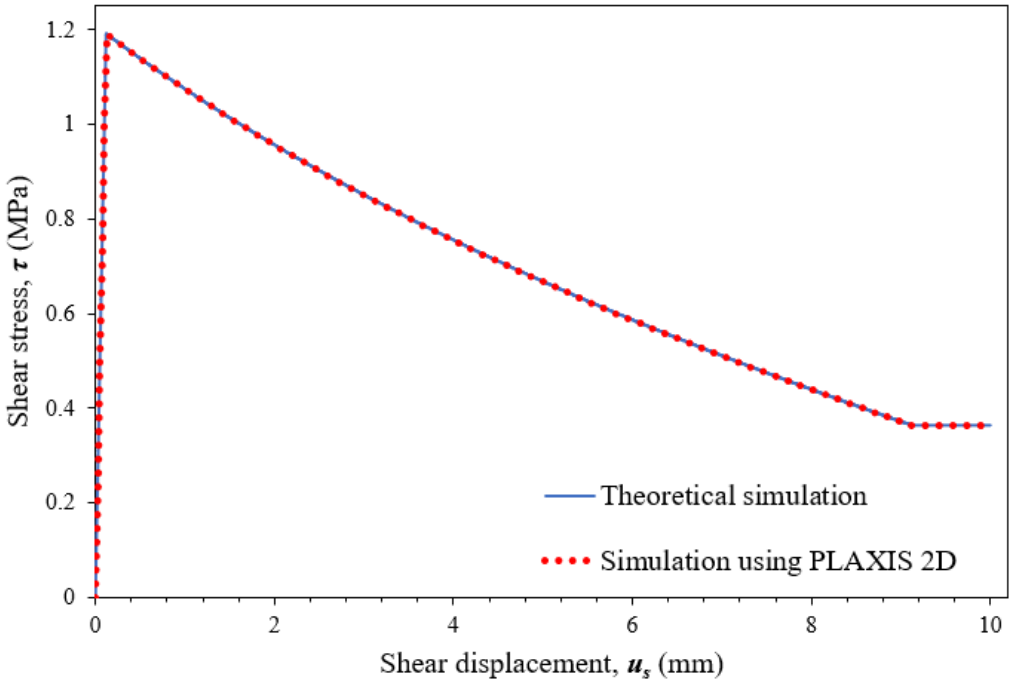

Figure 5.9: Shear displacement vs Shear stress response

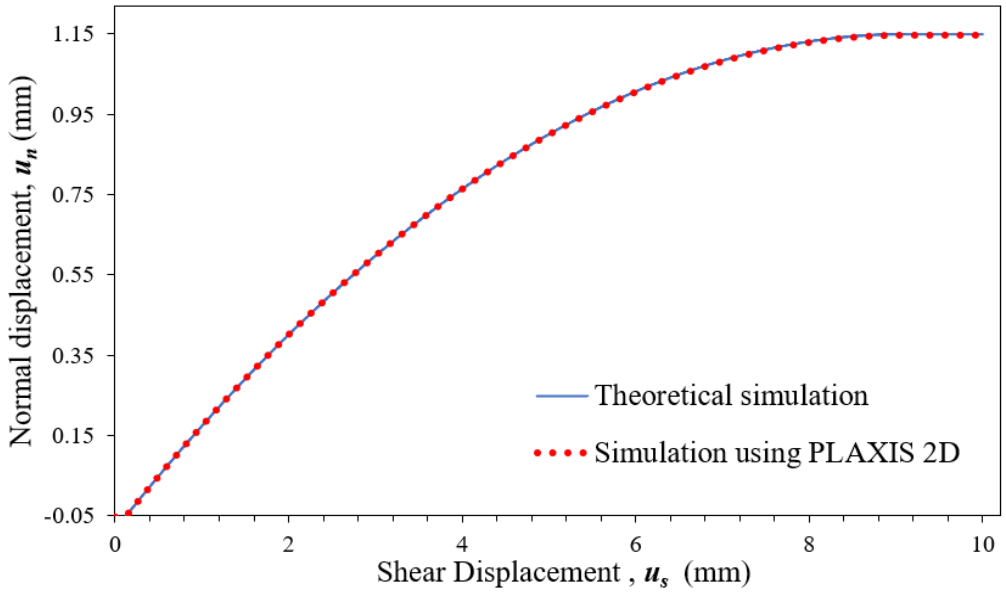

Figure 5.10: Shear displacement vs Normal displacement response

Figure 5.9 and Figure 5.10 confirm the reliability of the numerical implementation by indicating that the obtained results using the implemented version of the Barton-Bandis model in PLAXIS comply with the corresponding results of the theoretical simulation.

Finally, taking into account that both the theoretical simulation of the two-phased laboratory test and the simulation of the same test using the modified Barton-Bandis in PLAXIS 2D were performed considering a discontinuity in a limestone (γ = 25 kN/m^3) located at a 40m depth (as stated in Section 3.5) a normal load equal to 1 MPa was set to be applied on the discontinuity. Consequently, employing Equation (3.59), the value of the normal stress which corresponds to the transitional point between the low and high-stress level areas was determined. The calculated value was found to be equal to 0.046 Mpa which denotes that the set value of the applied normal stress was not lying within the area of the low-stress level. Therefore, considering also that the applied normal stress level remains constant during the shearing phase indicates that the current simulation was not affected by the selected values of cohesion and transitional friction angle.

Similarly, to the previous section, having confirmed that the implemented can reproduce theoretically the mechanical behaviour of a discontinuity subjecting to shearing under CNL conditions, the model was also verified based on the experimental results found in the literature. In more detail, the model was verified based on the experimental results reported by Skinas et al. (1990) who assessed the mechanical response of the rock discontinuities subjected to shear displacement under constant normal load conditions. The discontinuity surfaces studied by Skinas et al. (1990) were tilt-tested to measure the index of JRC. Four types of discontinuities of the same type of rock which are characterised by different values of JRC were tested with the following properties:

Table 5.3: Properties of the discontinuities studied by Skinas et al., (1990)

Parameters	Values
JRC	9, 12, 15 and 18
JCS	28 MPa
φ	37°

The mechanical response of the considered discontinuities under the application of 30 mm of shear displacement was examined for three different levels of applied normal stress. For the verification of the Barton-Bandis model with linear reduction of roughness, the reported results which correspond to the discontinuity characterized by a JRC equal to 9 were employed and the implemented version of the Barton-Bandis model in PLAXIS 2D was used for the simulation of the experimental test performed by Skinas et al. (1990). Similarly, to the previous section, to further confirm the validity of the numerical implementation the same tests were also simulated theoretically, and the results were plotted.

Table 5.4 presents the adopted parameters for the simulation of the considered experimental test using the modified Barton-Bandis.

Table 5.4: Adopted parameters of the modified Barton-Bandis model for the simulation of the mechanical response of the rock discontinuity studied by Skinas et al. (1990)

Parameters	Values
φ_{Tr}	70°
c	0.0035 MPa
ψ_{LS}	30°
σ_T	0
φ_{res}	37°
JRC	9
JCS	28 MPa
k_n	25 MPa/mm
k_s	2.5 MPa/mm
Dc	20 mm

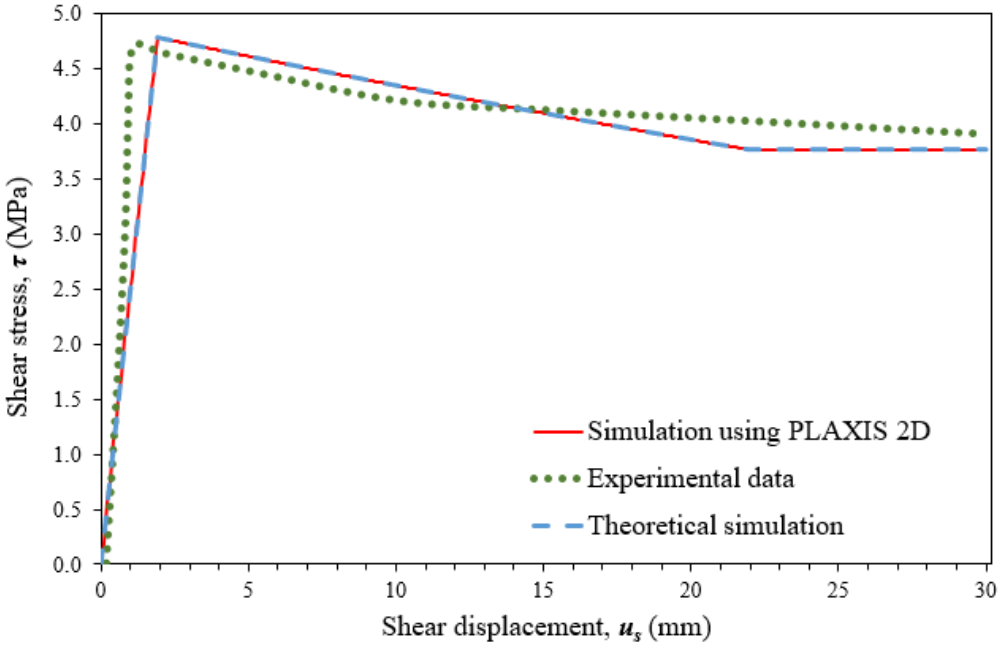

Figure 5.11: Simulation of shear stress-shear displacement response under σ_n=5 MPa

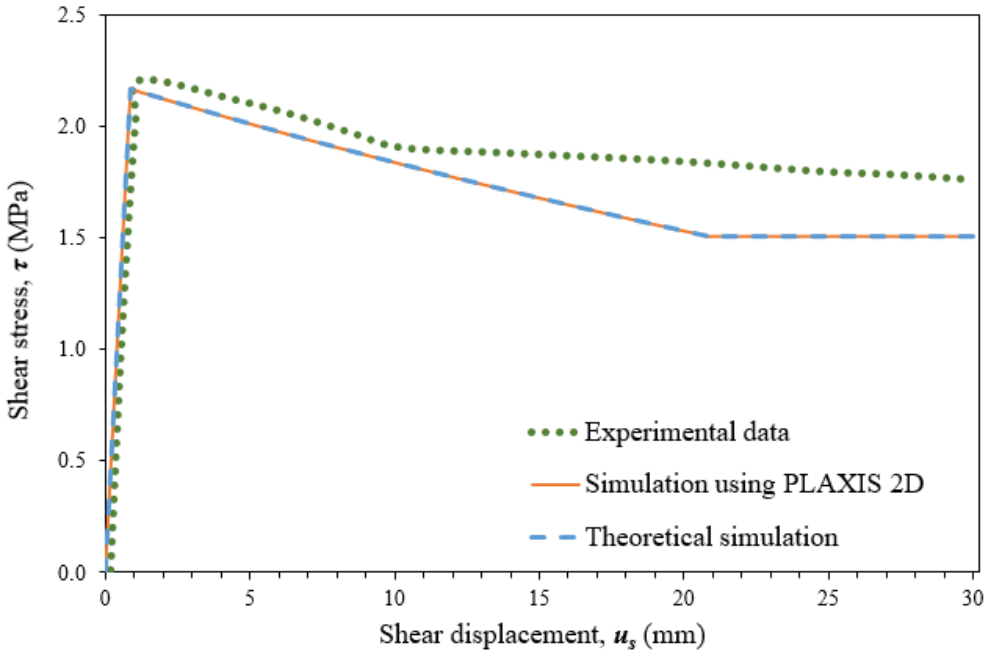

Figure 5.12: Simulation of shear stress-shear displacement response under σ_n=2 MPa

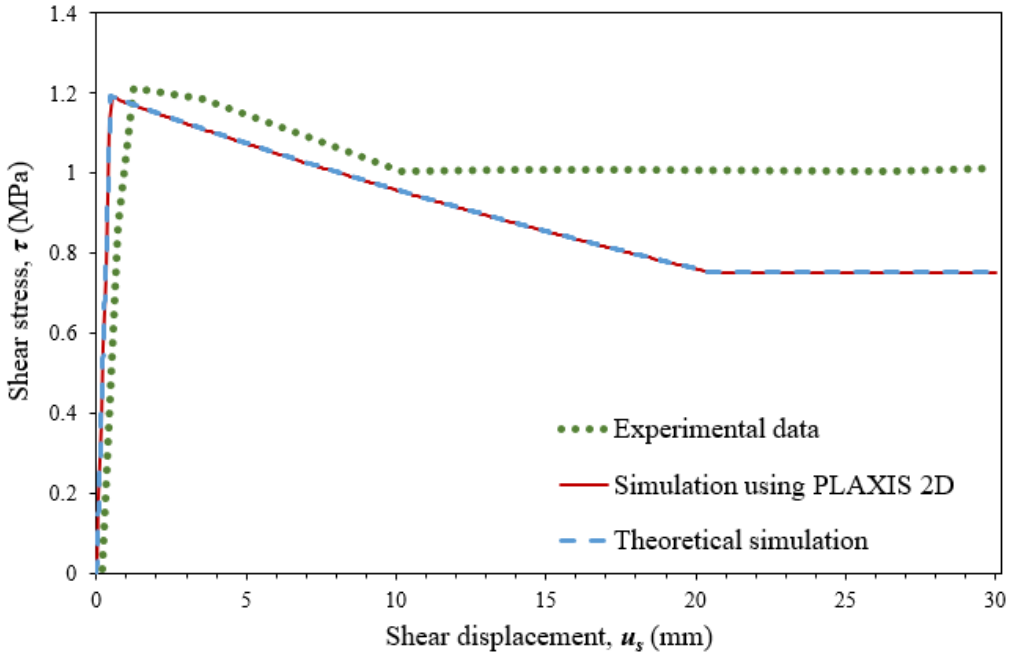

Figure 5.13: Simulation of shear stress-shear displacement response under σ_n=1 MPa

Considering that no experimental data were given by Skinas et al., (1990) for dilation at normal stress values of 5 MPa and 2 MPa only the exported results for a value of normal stress equal to 1 MPa were plotted against the experimental results.

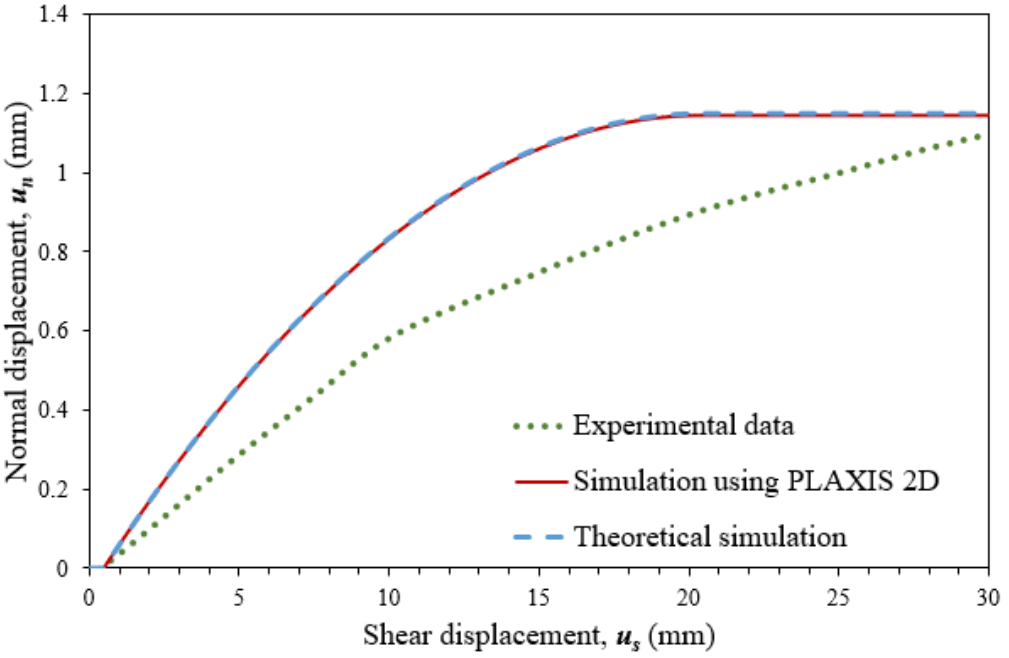

Figure 5.14: Simulation of normal displacement-shear displacement response under σ_n=1 MPa

Although no experimental data were given by Skinas et al., (1990) for the dilative behaviour at normal stress values of 5 MPa and 2 MPa, to further test the validity of the numerical implementation, the dilation was also numerically and theoretically simulated and plotted in Figure 5.15 and Figure 5.16. A perfect agreement between the finite element and theoretical results illustrates the correctness of the numerical implementation of the model in PLAXIS.

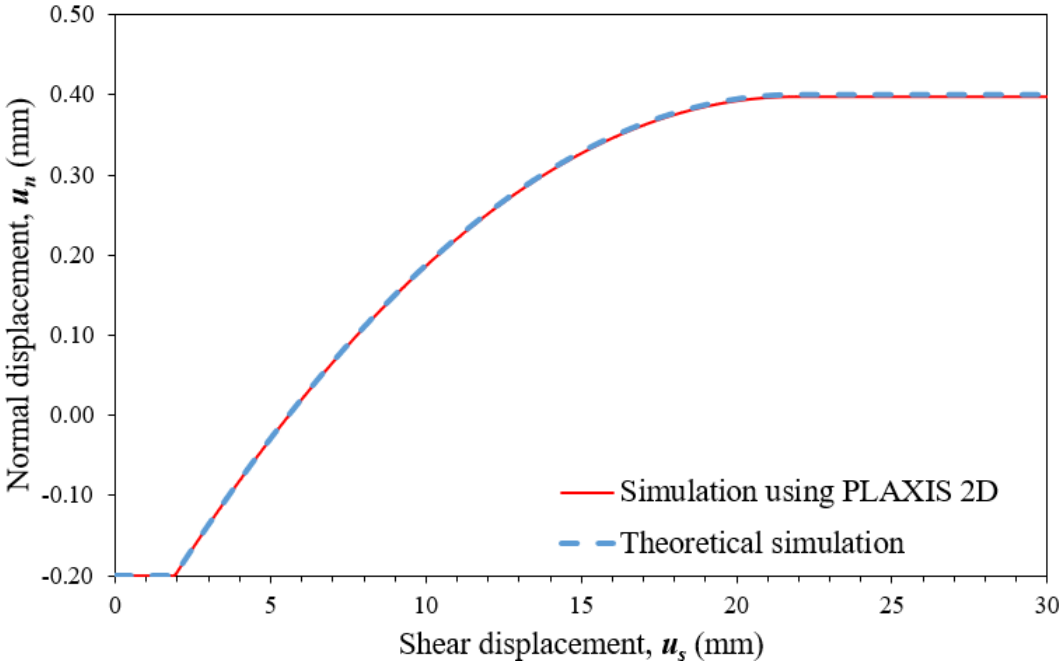

Figure 5.15: Simulation of normal displacement-shear displacement response under σ_n=5 MPa

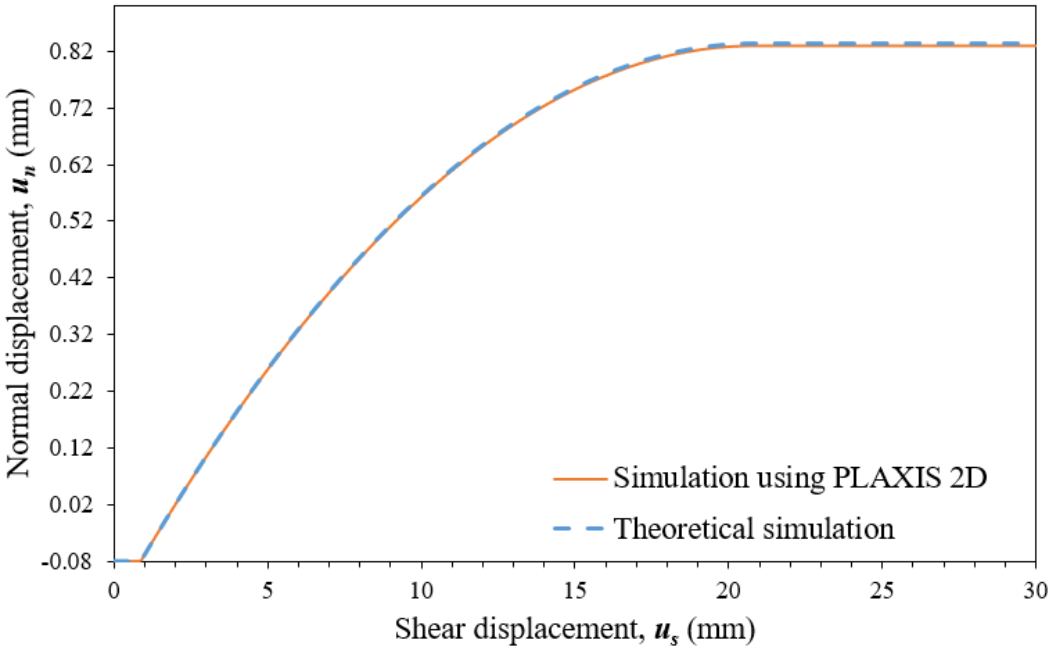

Figure 5.16: Simulation of normal displacement-shear displacement response under σ_n=2 MPa

Figure 5.11, Figure 5.12 and Figure 5.13 show that the implemented version of the modified Barton-Bandis in PLAXIS 2D can capture adequately the non-linear trend of the mechanical response of the discontinuity denoting that the evolution of shear stiffness and the value of the peak shear strength of the examined discontinuity can be reproduced accurately.

On the other hand, the results indicate that the considered model underestimates the post-peak mechanical shear strength. This underestimation can be explained considering the way through which the value of the JRC_{peak} parameter is decreased upon shearing. More specifically, as

described in 3.5.1 the linear decrease of JRC implies that the fully residual state is reached earlier than expected in the original Barton-Bandis model.

In addition, as it can be observed in Figure 5.14, even though the implemented constitutive law reproduces correctly the non-linear trend of the dilative behaviour of the discontinuity, the model overestimates dilation in this case. This might originate from the fact that Barton's dilation law is empirical and restrictive (there is no parameter to calibrate the initial dilation), which is not flexible enough to calibrate the dilation curve in this case.

In conclusion, regarding the residual state, it should be noted that in the range of shear displacement within the reported experimental results were performed, the discontinuity did not reach its residual strength, at least according to the definition of the Barton-Bandis model (residual state is defined when all the roughness is sheared-off and only the residual friction angle contributes to the shear strength). This definition is respected in the current implementation, i.e., the value of the ultimate residual strength is similar to what is predicted by the original Barton-Bandis model. However, the implemented simplified softening law might infer that the residual state is reached earlier than in the original model, leading to a more conservative strength prediction in the post-peak domain. Moreover, the empirical Barton-Bandis dilation law seems to be too restrictive to calibrate experimental data, as dilation is purely controlled by strength parameters.

6 Simulation of a deep excavation using the advanced implemented discontinuity models

6.1 Introduction

Having tested the validity of the numerical implementation of the selected constitutive laws for lab test simulations, these models are now tested in a large-scale rock engineering application, which consists of an underground tunnel excavation in a highly discontinuous rock mass. The tunnel is assumed to be long enough so that the excavation can be modelled by a 2D plane strain model.

The chosen network of discontinuities was generated using the extended version of the tool for the automatic projection of discontinuity networks (Chapter 4). For the generated system of discontinuities, the simulation of the considered engineering application was carried out employing four different constitutive laws. Concretely, the following models are considered:

1. Coulomb-based models: elastic-perfectly plastic Coulomb model (original version), elasto-plastic model with strain softening
2. Modified Barton-Bandis-based model

An investigation of the influence of the implemented laws on the stability of the jointed rock mass is executed by comparing qualitatively and quantitatively the exported results from the numerical analysis of the considered engineering application.

6.2 Model definition

6.2.1 Model configuration and meshing

A circular deep tunnel excavated in a layer consisting of homogeneous and highly discontinuous (weathered) limestone is modelled. The underground excavation was selected to be performed at a depth of 1 km. To practically model the considered application, only a block of 50m x 50m around the excavation is modelled. A thin fictitious layer of 1m thickness is introduced with its unit weight corresponding to the overburden pressure to represent the in-situ stresses. The limestone layer was assumed to be disrupted by two sets of fully persistent discontinuities The model shown in Figure 6.1 illustrates a two-dimensional plane strain representation of an excavated tunnel with a diameter equal to 5.5 m. Additionally, Figure 6.2 provides a closer representation of the distribution of the generated discontinuities around the excavated tunnel while also an indication of the blocks which are prone to instability mechanisms around the cavity. In more detail, it can be observed that the generation of the selected discontinuity network results in the creation of four wedges around the tunnel. In engineering practice, the stability of these blocks is examined closely considering that they are prone to failure under tensile stresses.

In addition, it should be noted that the discontinuity sets were projected using the extended version of the tool for the generation of discontinuity networks. The adopted geometrical properties for the projection of the considered discontinuity sets are illustrated in Table 6.1.

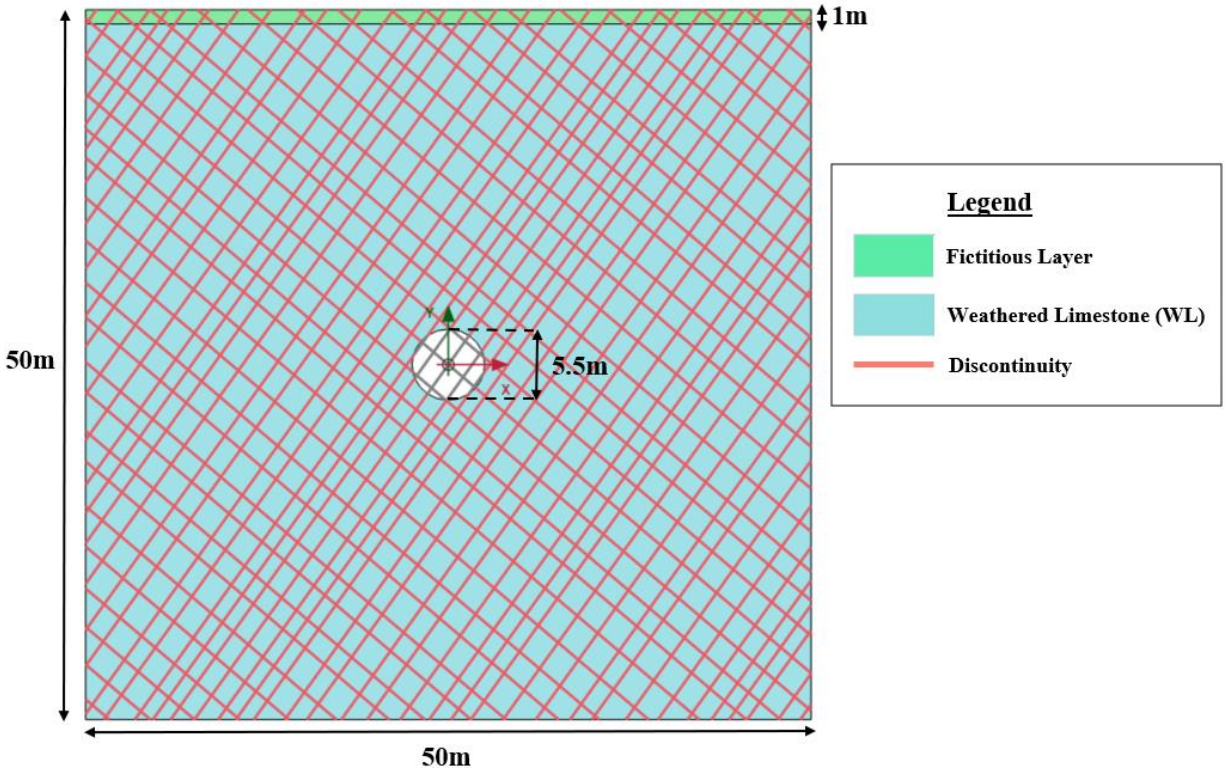

Figure 6.1: Geometry of the underground rock excavation model

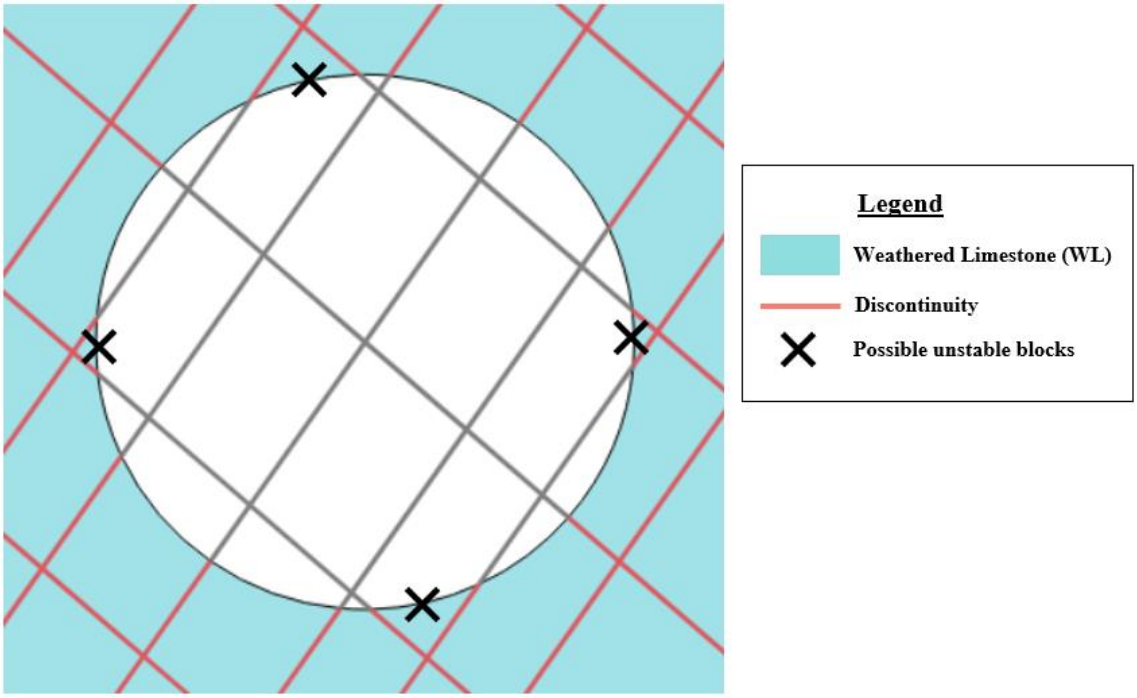

Figure 6.2: Closer presentation of the excavated tunnel and indication of possible unstable blocks

Table 6.1: Properties of the projected discontinuity sets

Component	Persistence	Plunge	Trace length (m)	Spacing (m)	Spacing Variation
1st Discontinuity set	Persistent	-55°	100	1.5	0.5
2nd Discontinuity set	Persistent	41°	100	2	0.5

Meshing

Similarly, to the created numerical model described in Section 5.2, 15-node triangular elements were used for the simulation of the considered engineering application with smaller elements being adopted in the zones of the model where larger strains were expected. Overall, a fine mesh was adopted within a square area (10m x 10m) around the tunnel. Within this area, a circular area with a radius equal to 5m from the centre of the tunnel was selected to be discretised with even finer mesh. On the other hand, a coarser mesh is adopted when the distance from the centre of the tunnel is larger than 10 m, considering that smaller strains are expected to develop. Figure 6.3 illustrates the generated mesh for the analysis of the considered underground rock excavation.

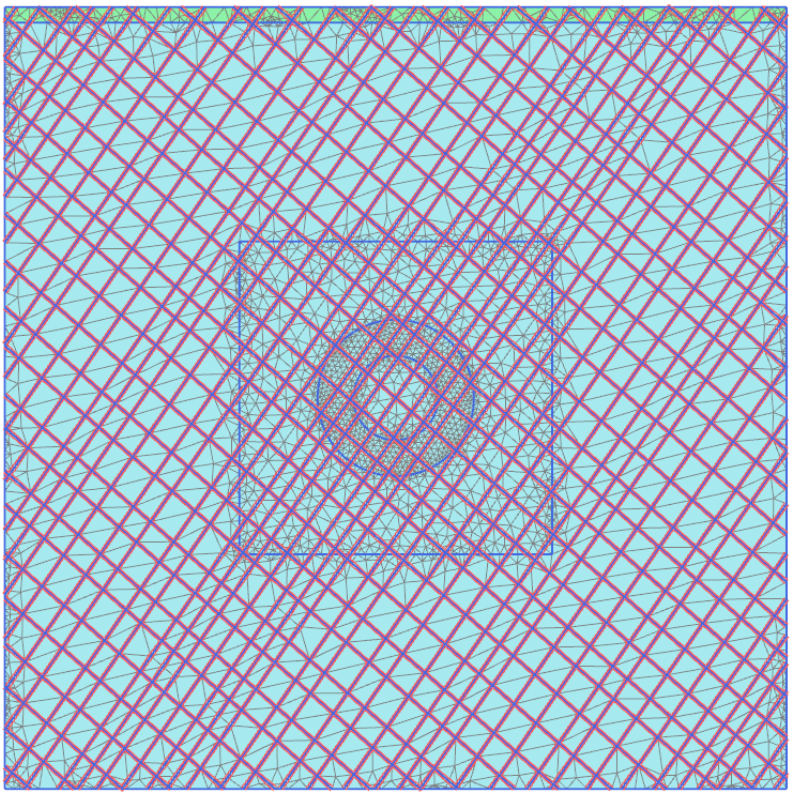

Figure 6.3: Generated mesh for the FE analysis of the underground excavation

6.2.2 Material parameters

The created model of the considered underground rock excavation model is divided into two main components. The first component concerns the properties of the adopted rock material and the fictitious layer as they are presented in Table 6.2. It must be pointed out that within the framework of the performed analysis, the intact rock blocks of both layers were modelled as linear-elastic and isotropic materials. In this way, it was ensured that the considered FE analysis is focused only on the mechanical behaviour of the discontinuities.

Table 6.2: Properties of the rock components of the underground excavation model

Component	Soil model	γ_{unsat} (kN/m^3)	γ_{sat} (kN/m^3)	E_{ref} (MPa)	Poisson's ratio, ν
Weathered Limestone	Linear Elastic	25	25	15E3	0.25
Fictitious Layer	Linear Elastic	20E6	20E6	15E3	0.25

Additionally, the second component concerns the properties of the adopted constitutive laws. As stated in Section 6.1, the simulation of the considered engineering application was carried out employing four constitutive laws. The derivation of the values of the required parameters for each constitutive law was based on the experimental results reported by Skinas et al. (1990) which were also used for the verification of the Barton-Bandis model with linear reduction of roughness. Skinas et al. (1990) studied the mechanical response of artificial discontinuities which have been cast from natural discontinuity surfaces using a brittle artificial material. The mechanical properties of the generated material are listed below:

Table 6.3: Mechanical properties of the artificial material used by Skinas et al. (1990)

σ_c (MPa)	E_{ref} (GPa)	Poisson's ratio, ν
25-30	3-3.5	0.2

The reported mechanical properties of the artificial material used by Skinas et al. (1990) lead to the implicit assumption that using the considered material the behaviour of a weathered limestone was simulated. In addition, considering that the influence of the constitutive laws will be investigated by simulating a deep rock excavation where high-stress levels are expected in combination with the limitation of the Barton-Bandis model, to perform in applications that are governed by stress levels higher than the value of the JCS, add the requirement of simulating the engineering application adopting a material with high value of uniaxial compressive strength, σ_c. Table 6.3 denotes that the examined material (limestone) has a considerably high value of σ_c which makes it suitable for the simulation of the considered application employing the implemented version of the Barton-Bandis model. Finally, the implicit assumption that the discussed replicas correspond to limestone can justify the generation of the dense discontinuity network considering that the assumed lithology is often found fractured on the field.

Concluding having verified the modified Barton-Bandis model as described in Section 5.4.1, the same experimental data reported by Skinas et al. (1990) were used for the calibration of the Coulomb-based models. Considering that all the Coulomb models are based on the Coulomb strength criterion in combination with the fact that the Coulomb with linear softening also requires the calibration of the Dc parameter, the calibration was performed using only the newly implemented version of Coulomb model with linear strain softening. The adopted values of required parameters for each law are summarized in Table 6.4 while the obtained results of the calibration were plotted against the shear displacement and are illustrated in the following figures (Figure 6.4-Figure 6.7). Finally, it should be noted that the adopted values of the parameters related to the implemented version of Barton-Bandis are the same as those presented in Table 5.4.

Table 6.4: Calibrated parameters of Coulomb-based models

Model	c (Mpa)	c_{res} (Mpa)	φ (°)	φ_{res} (°)	ψ (°)	ψ_{res} (°)	k_n (Mpa/mm)	k_s (Mpa/mm)	Dc (mm)	Dilation cut-off (mm)
Coulomb (original)	0.342	X	41	X	4	X	25	2.5	X	X
Coulomb with strain softening	0.342	0.27	41	36	4	1.55	25	2.5	16	29
Coulomb (brittle)	0.342	0.27	41	36	4	1.55	25	2.5	0	29

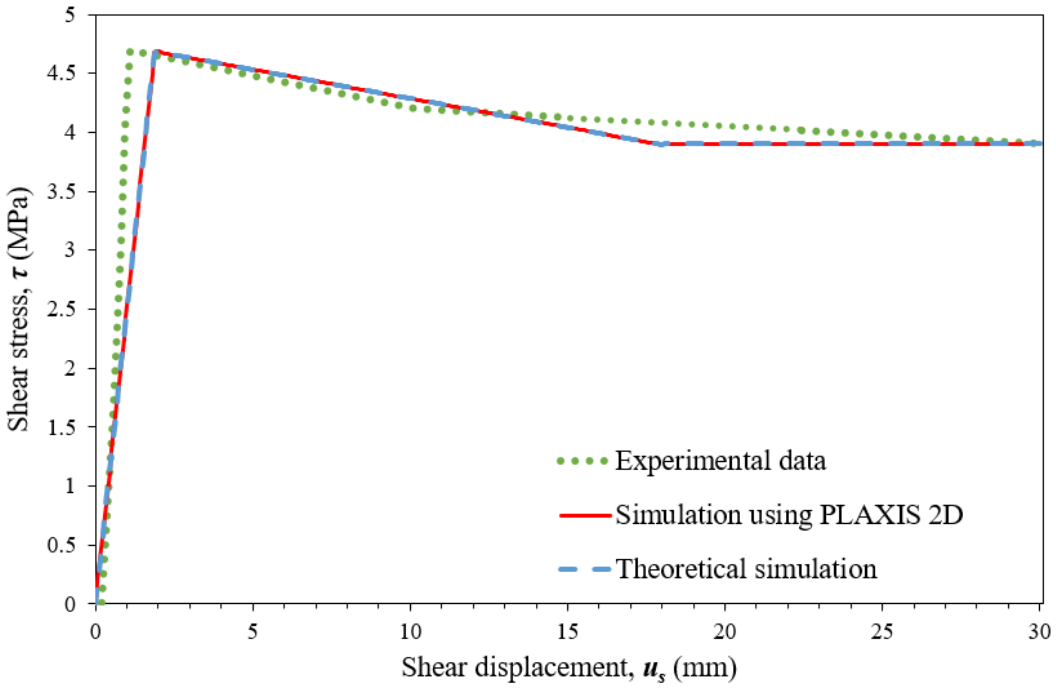

Figure 6.4: Simulation of shear stress-shear displacement response under σ_n=5 MPa

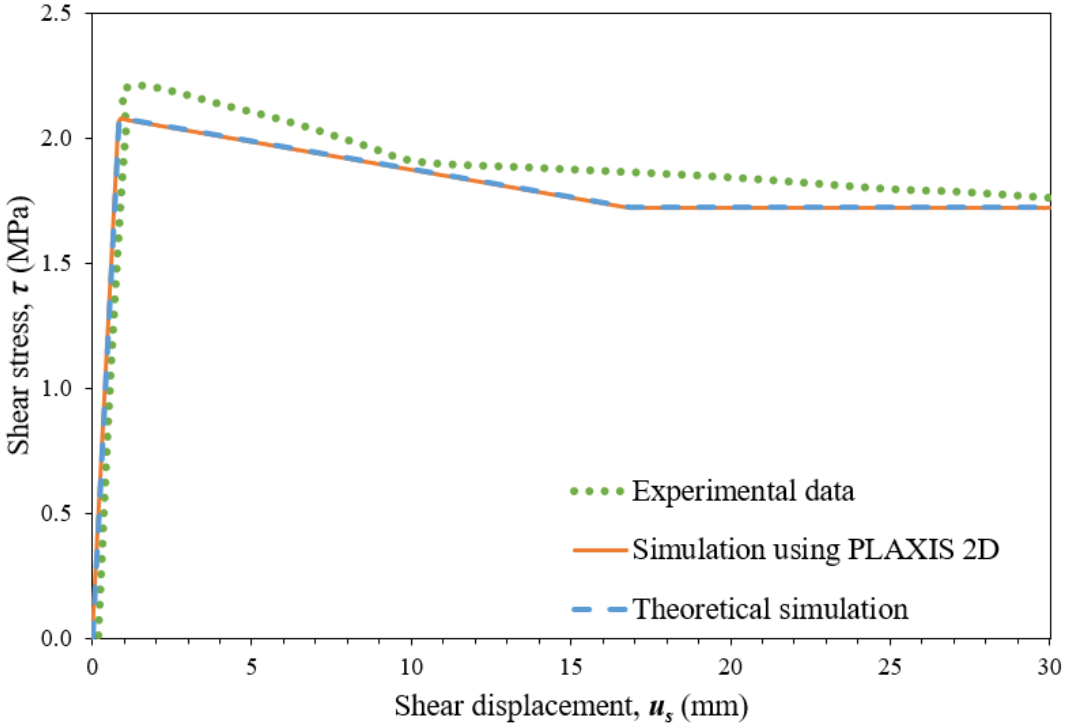

Figure 6.5: Simulation of shear stress-shear displacement response under σ_n=2 MPa

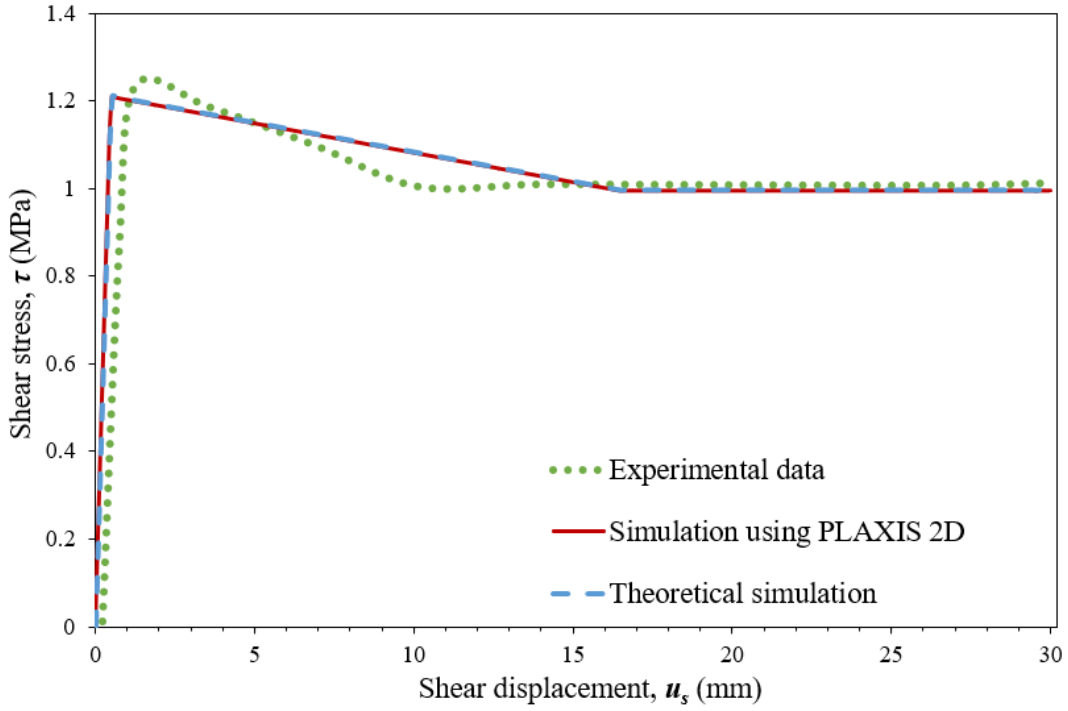

Figure 6.6: Simulation of shear stress-shear displacement response under σ_n=1 MPa

Similarly, to section 5.4.1, considering that Skinas et al. provided results regarding the dilative behaviour only when it is subjected to a normal stress level equal to 1 MPa only the exported results for a value of normal stress equal to 1 MPa were plotted against the experimental results.

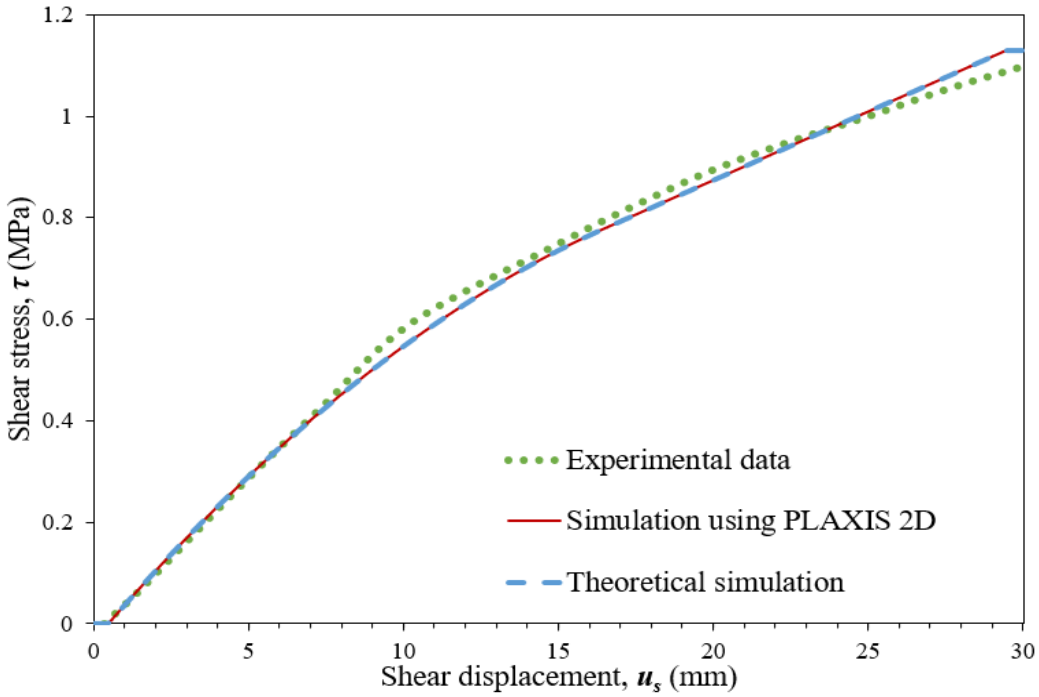

Figure 6.7: Simulation of normal displacement-shear displacement response under σ_n=1 MPa

The obtained results show that the Coulomb with linear softening model adopting the considered values can capture adequately the non-linear behaviour of a discontinuity subjected to shearing under CNL conditions indicating the peak and residual shear strength while also providing a fair approximation of the post-peak behaviour. Furthermore, the examined model matches very well the experimental results regarding the dilative behaviour of the discontinuity. This might be due to a higher number of parameters used in this model, which allows for a more flexible calibration from experimental data.

6.2.3 Initial, boundary conditions and staging

Geostatic stress initialization

The initial stress state of the created model was generated using a K_0 condition which requires the definition of the earth pressure coefficient at rest, K_0. In this research project, the value of K_0 was set equal to 0.3. Furthermore, considering that the overburden pressure is applied through the modelled fictitious layer whose unit weight is equal to 20 MN/m^3 and its thickness equal to 1m, the applied vertical stress varies linearly from the top to the bottom of the model. At the top of the model, the vertical stress is equal to:

$$\sigma_{v_{top}} = \gamma * z = 20 \frac{MN}{m^3} * 1m = 20\ MPa$$

While at the bottom of the generated model the vertical stress is equal to:

$$\sigma_{v_{bottom}} = \sigma_{v_{top}} + \gamma * z = 20\ MPa + 25 \frac{kN}{m^3} * 50m = 21.25\ MPa$$

Additionally, using the defined value of the earth pressure coefficient at rest the value of the in situ horizontal stress is calculated employing the K_0 condition. Similarly, to vertical stress horizontal stress varies with the same linear pattern. At the top of the model, the horizontal stress is equal to:

$$\sigma_{h_{top}} = K_0 * \sigma_{v_{top}} = 0.3 * 20\ MPa = 6\ MPa$$

While at the bottom of the model, the horizontal stress is equal to:

$$\sigma_{h_{bottom}} = K_0 * \sigma_{v_{bottom}} = 0.3 * 21.25\ MPa = 6.37\ MPa$$

Phases of the analysis

For each constitutive law, the modelling sequence was initiated with the generation of the in-situ stresses using the K_0 procedure. The second phase of the simulation concerns, the excavation of the tunnel. It must be pointed out that the excavation was performed in one phase and the tunnel was assumed to be self-supporting without the need for installation of any supporting measures (i.e. lining). The unbalance between the externally applied forces and the internal stresses in the rock layer due to the absence of the excavated material is solved using the FE software PLAXIS 2D.

Boundary conditions

Considering that the examined underground excavation is performed in a great depth, the deformations that will occur due to the removal of the excavated material will be limited to a considerably large area around the tunnel without having any effect on the ground surface. For this reason, it should be pointed out that all the boundaries of the generated model were modelled as fully fixed. Figure 6.8 illustrates the mesh adopted in the present analysis in combination with the applied boundary conditions:

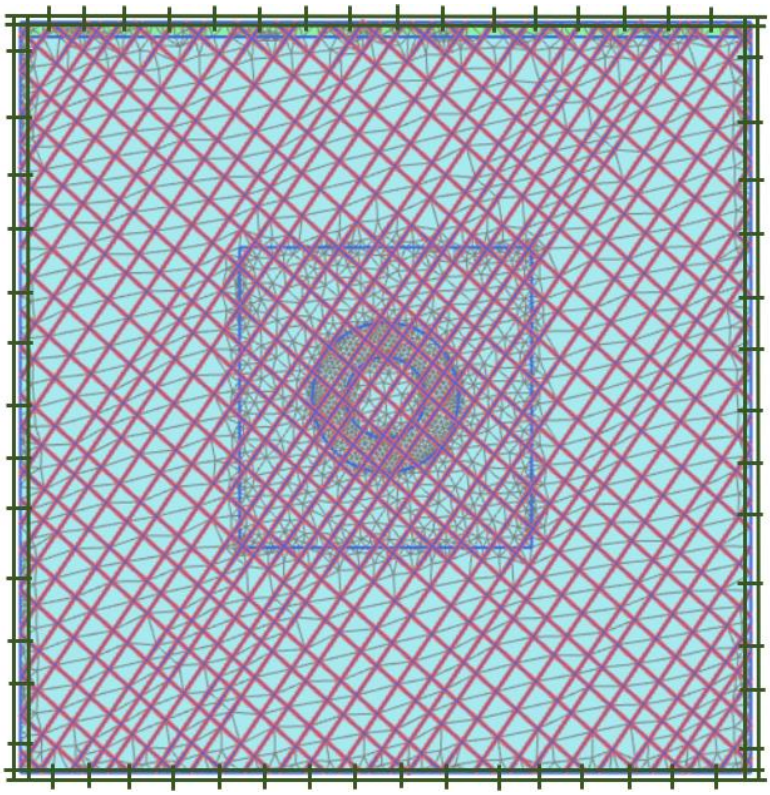

Figure 6.8: Adopted mesh and applied boundary conditions

6.3 *Analysis of the results*

The simulation of the underground excavation was performed employing the four selected constitutive laws. The exported results were analysed to highlight the differences between the considered laws. In this research work, the analysis of the exported results was mainly focused on two features:

- Stability and deformation around the tunnel
- Stress analyses of some critical discontinuities

6.3.1 *Stability and deformation around the tunnel*

Magnitude of total displacement around the tunnel

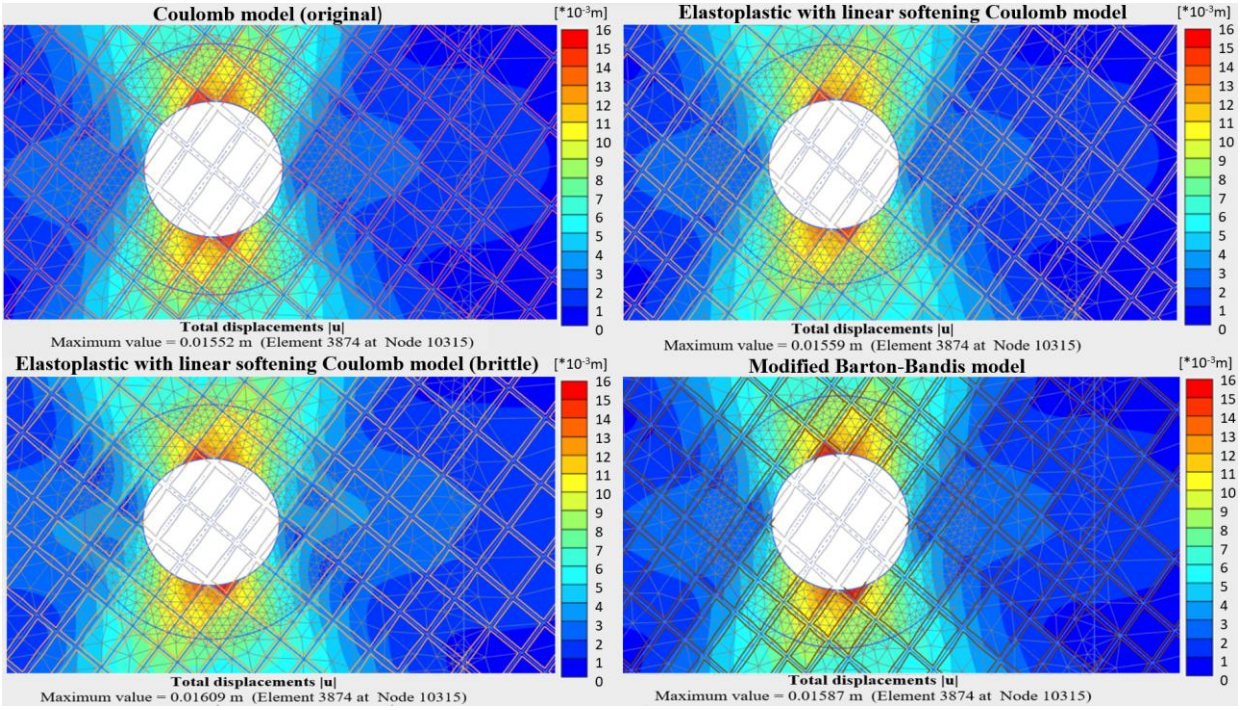

Figure 6.9: Total displacements employing each constitutive law

Observing Figure 6.9 it can be noted that the distribution of total displacements around the tunnel is similar for all the employed models. Furthermore, observing the obtained results in combination with the obtained deformed mesh at the end of the calculation phase presented in Figure 6.10, it can be noted that the displacements are concentrated on a zone which crosses the tunnel vertically. This deformation pattern can be justified considering the low value of K_0 which has been adopted to the model and results in the limitation of the effect of horizontal field stress. Additionally, from a quantitative point of view, all the selected models render a relatively small value of total displacements after the excavation of the simulated tunnel.

The total displacements obtained with the original Coulomb model do not deviate considerably from the obtained values using the implemented more advanced constitutive laws (around 16 mm). This might be explained by the fact that the rock mass is quite stiff and as a result, the shear displacements along the discontinuity are not high enough to create a big difference in the post-peak region between the perfect plastic and softening models. Moreover, in this case, differences between the Coulomb and Barton-Bandis strength envelopes are not significant (see

the experimental calibration in Section 6.2). To further explain, the Coulomb and modified Barton-Bandis yield surfaces are plotted in Figure 6.11 considering the adopted values of the required parameters reported in Table 5.4 and Table 6.4. In the zone of small normal stresses (less than 7 MPa), where most of the local failures happen, the difference between the two yield surfaces is not so significant.

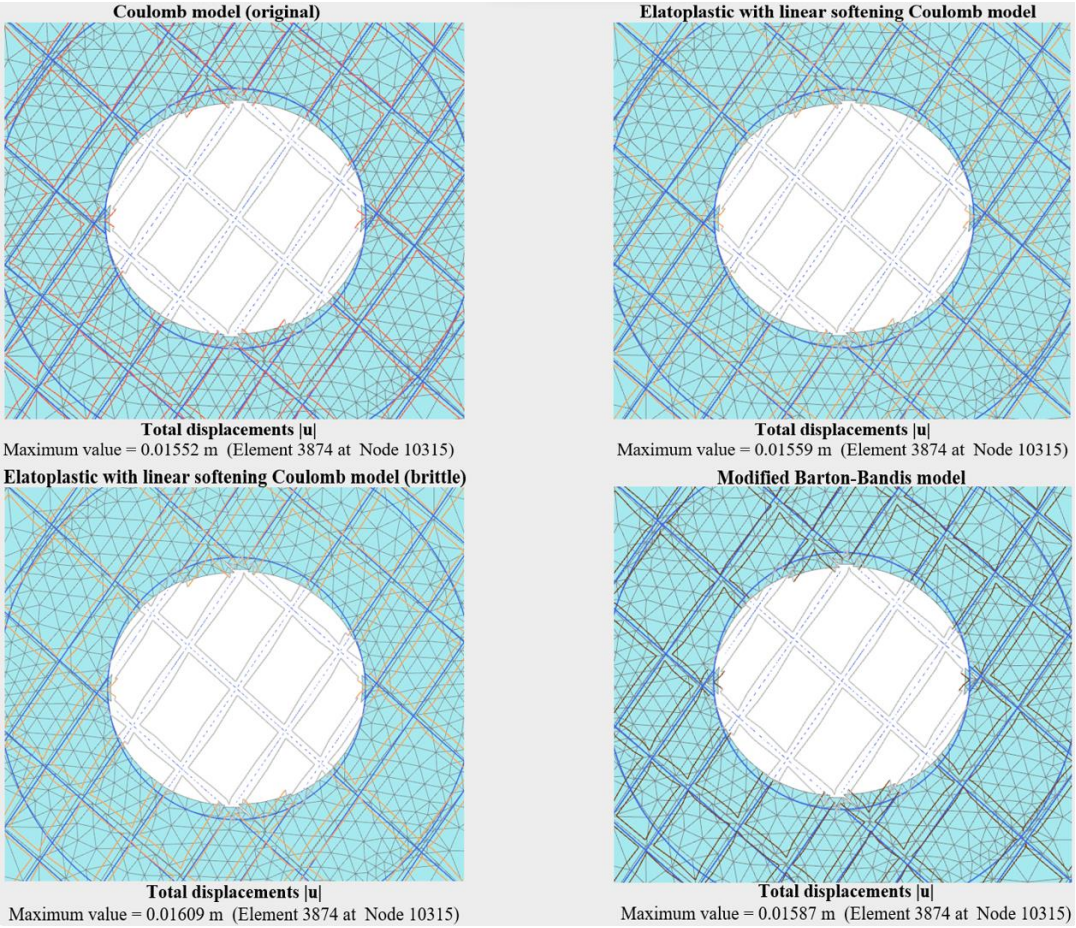

Figure 6.10: Obtained deformed mesh at the end of the simulation

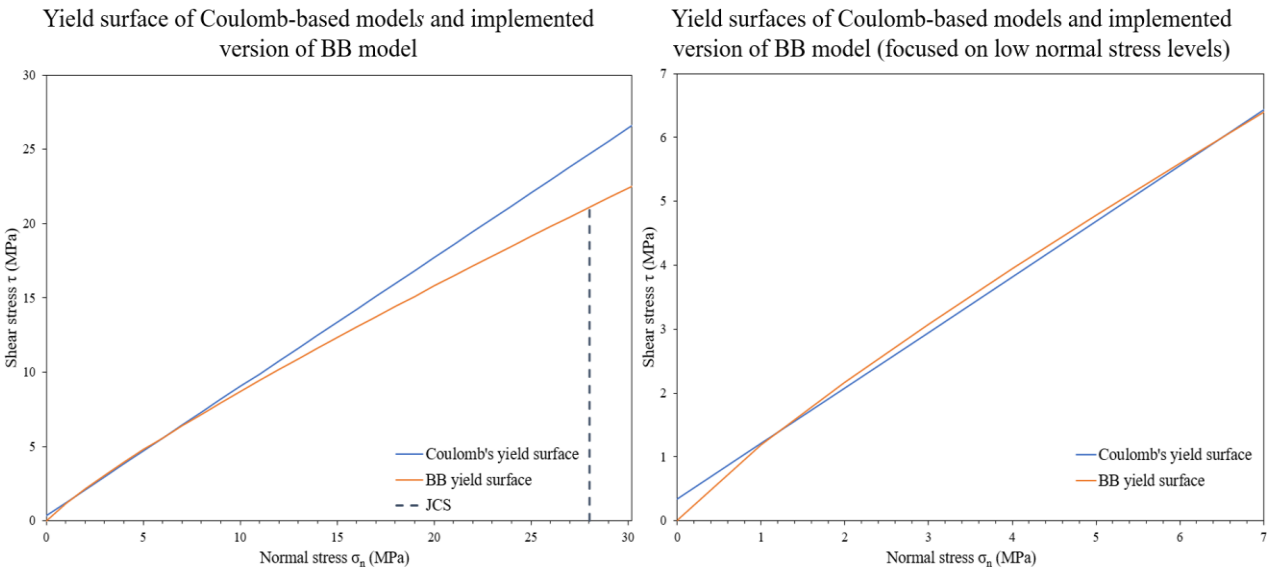

Figure 6.11: Yield surfaces of Coulomb-based models and modified Barton-Bandis model

Furthermore, it should be noted that higher displacements are concentrated on the two wedges located at the roof and the floor of the tunnel. This can be explained by a high-stress release around these wedges due to the excavation. Concretely, when radial stresses are completely removed at the end of the excavation, these two wedges are then 'pushed' towards the centre of the tunnel which causes the movement of the intact rock blocks of the wedges under both shearing and especially opening along the discontinuities.

Failure and instabilities

The shear failure and tension cut-off points along the discontinuities are illustrated in Figure 6.12.

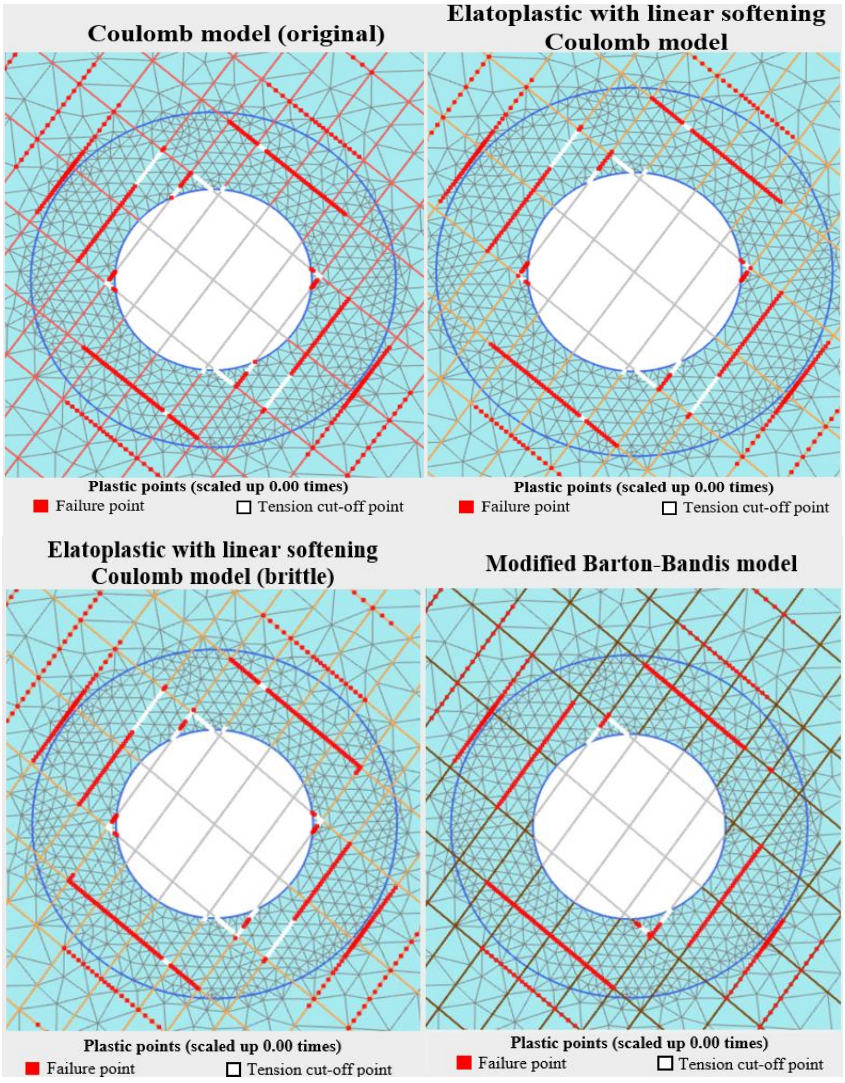

Figure 6.12: Obtained failure and tension cut-off points for each constitutive law

Similar to the deformation pattern, it can be observed that the distribution of both shear failure and tension cut-off points does not deviate considerably among the used constitutive models. Furthermore, in all the cases some discontinuities around the tunnel fail in shear or tension. Tension reasonably occurs around the critical wedges in the vicinity of the excavation. However, the extracted results using the implemented version of the Barton-Bandis model indicate tension cut-off points only along the discontinuities which form the wedges on the roof and the floor of the tunnel. Compared to the other models, in the modified Barton-Bandis

model, no plastic points are visible at the two small wedges on the left and right of the excavation at the end of the phase (Step 193). This is related to the PLAXIS numerical stepping control procedure because these wedges did fail in previous steps as indicated by Figure 6.13.

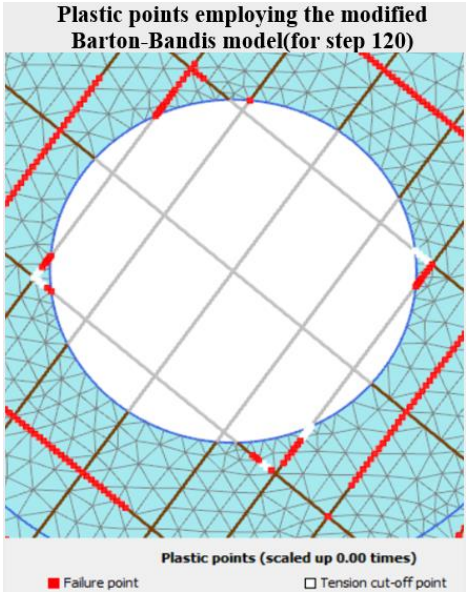

Figure 6.13: Obtained plastic point at step 120 using the implemented version of the Barton-Bandis model

An important point is that the 120th step already represents an end stage of the excavation, as the value of ΣMstage is already very close to 1 as can be seen in Figure 6.14. Note that ΣMstage is the proportion of the unbalanced that is to be solved in a staged construction calculation, which should reach 1 at the end of the excavation when stress removal due to excavation is almost complete. From Figure 6.14 it can also be seen that ΣMstage changes very little from step 100 but due to localized failure at the wedges, PLAXIS activates its automatic stepping and loading control procedure to slowly capture these local mechanisms, leading to a stress redistribution. Some stress points then move slightly inside the yield domain and become elastic.

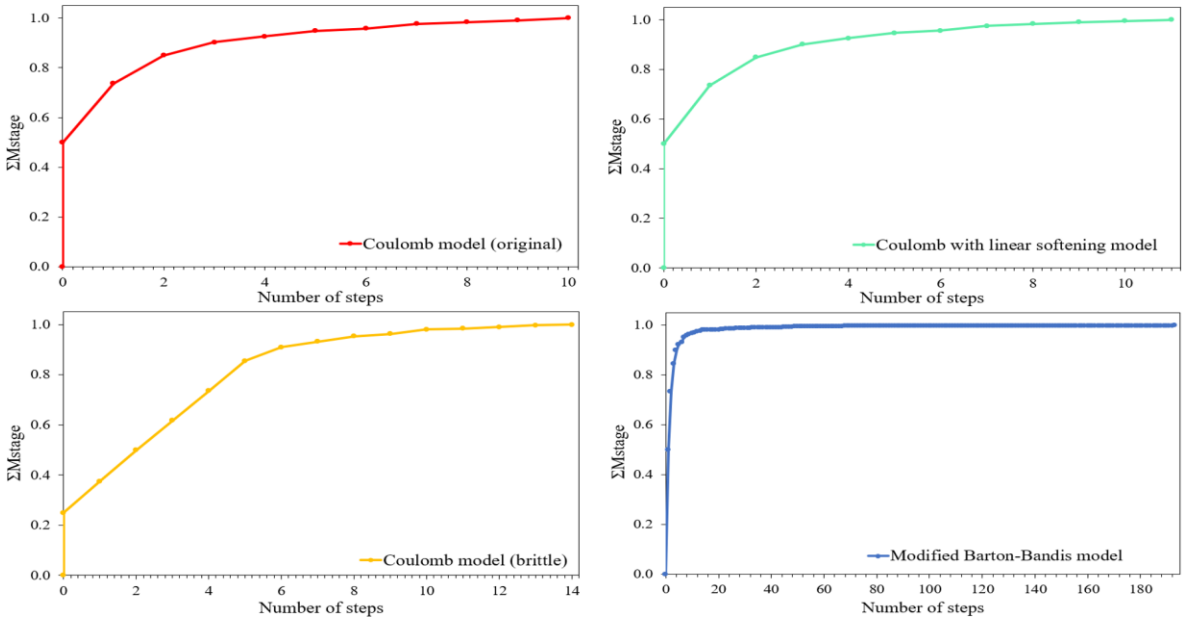

Figure 6.14: Plot ΣMstage vs Number of steps for each constitutive law

In addition, the model failure and instability can be assessed indirectly through a measurement of the Current relative Stiffness Parameter (CSP). CSP is 1 for elastic loading and close to zero when failure is detected, i.e., when a large amount of deformation is generated with a very small amount of load. Figure 6.15 shows the evolution of CSP with step numbers in the 4 analyses. For the modified Barton-Bandis model, CSP reaches a much lower value (and close to zero) compared to other models. Note that at step 150 of the Barton-Bandis analysis, CSP jumps back to 1 before going down again to a very small value (0.01435) at the end of the analysis, indicating a numerical unloading procedure explained earlier. Overall, the very small CSP obtained with the Barton-Bandis model gives an indication in all the cases, that the local wedge failures do not explicitly lead to global instability and that the model using the modified Barton-Bandis law is more prone to failure compared to other models. This again can be explained by the difference between these two models at very low-stress region (Figure 6.11). In this zone of low or zero normal stresses, while the Coulomb models still allow to mobilize a quite high amount of shear strength which contributes to the stability of the wedges due to the cohesion, the modified Barton-Bandis has a very low shear strength which might indicate more instability of the wedges.

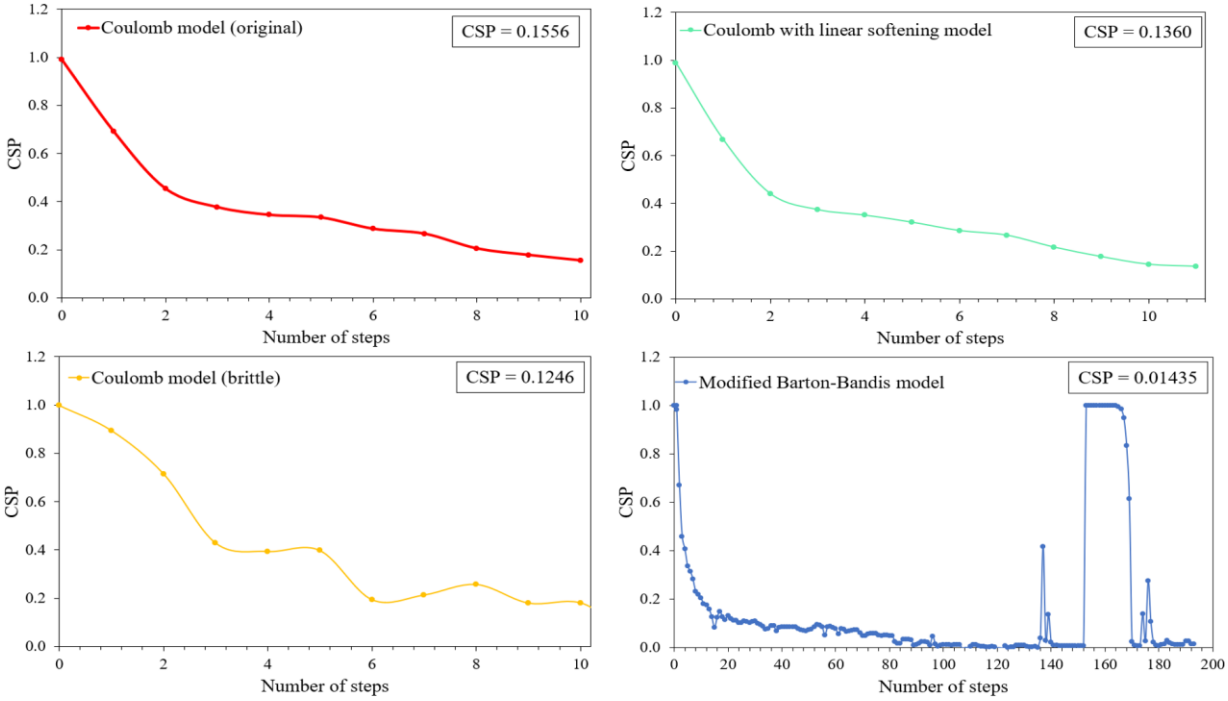

Figure 6.15: Plot CSP vs Number of steps for each constitutive law

To explain further the failure obtained in the models, a stress analysis is performed hereafter for a critical wedge.

6.3.2 Behaviour of the discontinuities of the most critical wedge

The evolution of the generated shear and normal stresses along the discontinuities which form the wedge at the roof of the tunnel was further investigated. The selection of the upper wedge was done considering that all the performed simulations using the four different constitutive laws denote the existence of several tension cut-off points along the discontinuities which are related to the generation mechanism of this wedge. Furthermore, it should be noted that the position of the selected wedge in combination with the fact that is larger than the wedges at the sides of the tunnel enhance the effect of the gravitational loading which is critical for the

stability of the considered wedge. Figure 6.16 illustrates the examined wedge and discontinuities.

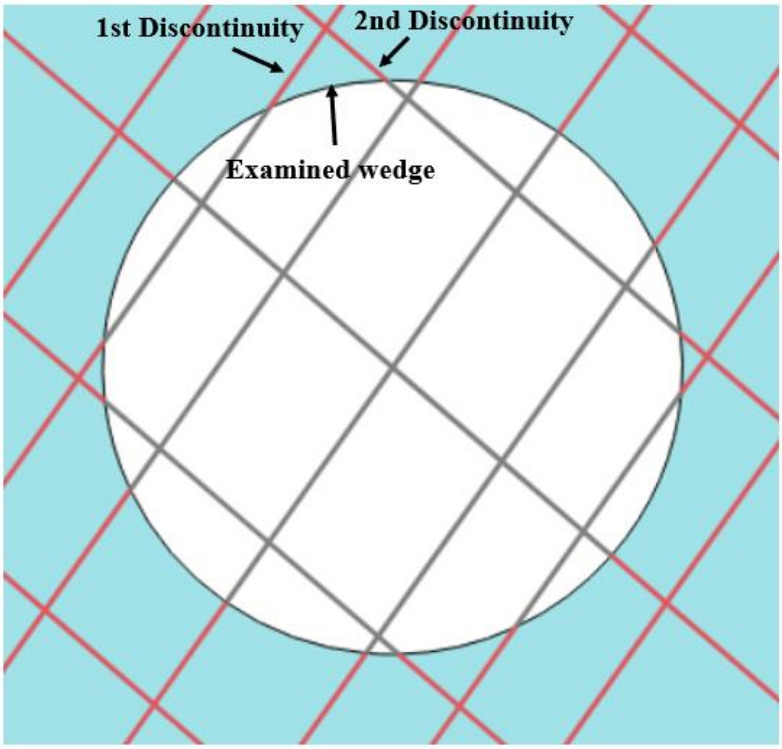

Figure 6.16: Examined wedge and discontinuities at the roof of the tunnel

6.3.2.1 Stress analysis of the first discontinuity

Figures 6.17 and 6.18 present the evolution of normal and shear stress along the 1st discontinuity respectively. The measuring of the length of both examined discontinuities started from the points where the two discontinuities intersect the tunnel.

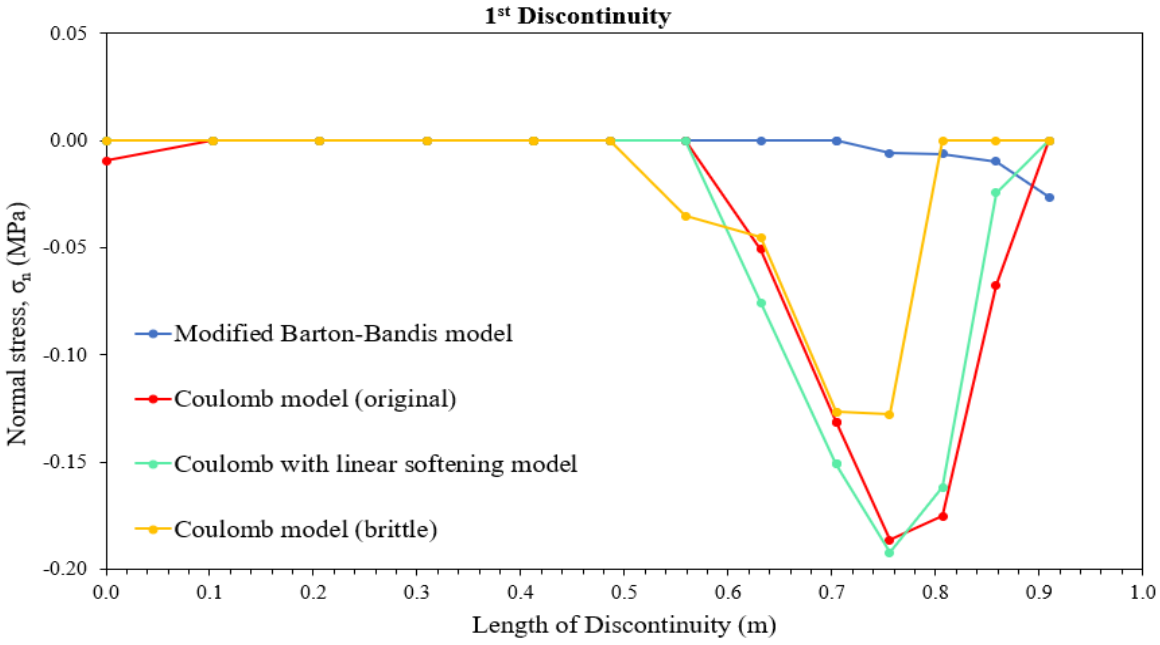

Figure 6.17: Evolution of normal stress along the 1st Discontinuity for each constitutive law

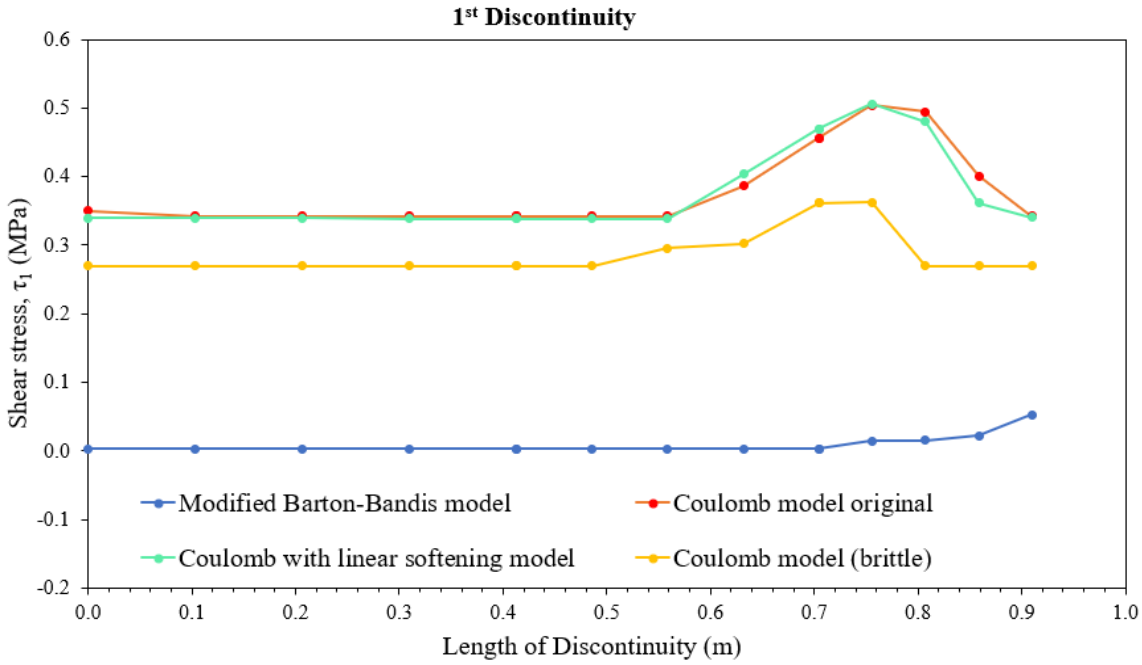

Figure 6.18: Evolution of shear stress along the 1st Discontinuity for each constitutive law

From a qualitative aspect, the obtained results presented in Figure 6.17 indicate that for all constitutive laws, the normal stress is negligible when being close to the excavated tunnel which is in accordance with the distribution of the tension cut-off points along the examined discontinuity presented in Figure 6.12.

Furthermore, it can be observed that the normal stress using the modified Barton-Bandis model remains negligible for a larger distance than the one using one of the Coulomb-based models. In this way, the existence of more tension cut-off points using the considered model can be explained. Additionally, the observed peak value of normal stress using the Coulomb-based models is considerably higher than the corresponding one using the implemented value of Barton-Bandis.

Moreover, Figure 6.18 indicates that the original Coulomb model and the Coulomb with linear softening model show a higher value of shear stress as was expected considering that the highest value of the applied normal stress was obtained using these two constitutive laws. Additionally, the brittle version of the Coulomb model leads to lower shear strength as was expected while the use of the implemented version of the Barton-Bandis model results in a considerably lower peak value of shear stress. This can be justified by the differences between the strength envelops used laws as previously analysed (Figure 6.11), especially at low or nil normal stresses. Hereafter, a more in-depth verification of the stress state of two specific plastic points is carried out in order to further check the accuracy of the implementation for each examined model. In more detail, for both examined discontinuities two points were selected. The first point corresponds to the intersection point of the examined discontinuity with the excavated tunnel while the second point corresponds to the intersection point of the two examined discontinuities. Figure 6.19 indicates the selected point for each discontinuity.

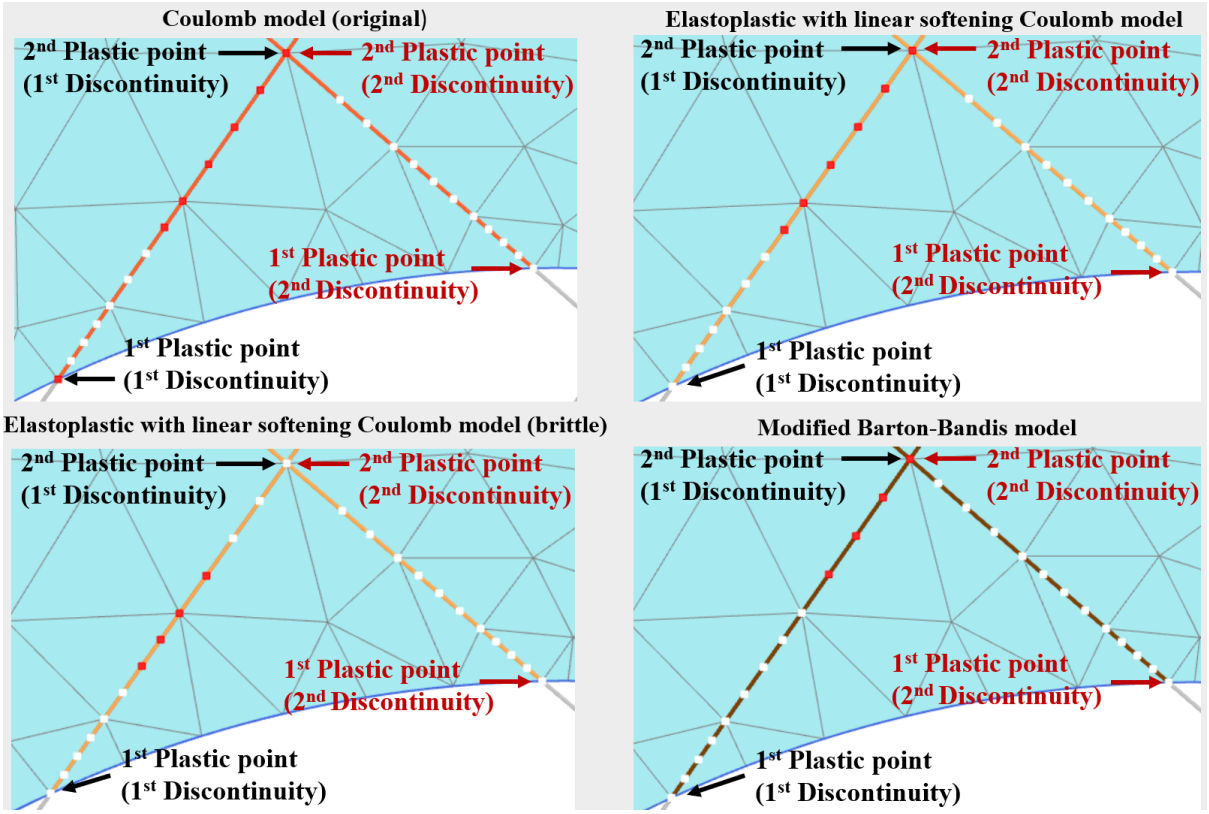

Figure 6.19: Selected Plastic points of each discontinuity

As it is indicated by Figure 6.19 the second examined plastic point of the first discontinuity lies in the same location with the corresponding examined point of the second discontinuity.

Original Coulomb model

The obtained results of the calculated stresses at the end of the calculation phase show that the first point fails in shearing while the second fails in tension (Table 6.5).

Table 6.5: Results of the stress analysis of the 1st Discontinuity using the original Coulomb model

Structural element	Plastic point	Node	Local number	X [m]	Y [m]	σ'_N [kN/m²]	σ_N [kN/m²]	τ_1 [kN/m²]	τ_{max} [kN/m²]
Discontinuity_7_18 Element 868-1149 (Discontinuity) (Disc_UddCoulomb_original)	1	20181	5	-1.14	2.45	-9.32	-9.32	350.10	350.10
Discontinuity_7_18 Element 868-1151 (Discontinuity) (Disc_UddCoulomb_original)	2	26463	1	-0.62	3.19	0.00	0.00	342.00	342.00

The depicted results in Table 6.5 indicate the obtained stress results of these two nodes. Node 20181 corresponds to the first point where the discontinuity intersects with the tunnel while node 26463 corresponds to the intersection point of the two discontinuities. For the first point, the value of the current shear stress (τ_1) is equal to the value of the peak shear strength (τ_{max}) which corresponds to the current normal stress level (easily calculated with the Coulomb criterion 3.36), indicating a shear failure state. For the second node, the value of τ_1 is also equal to the value of τ_{max} but due to its nil normal stress, the stress state is considered to be at the corner of the yield contour, namely at the intersection of shear and tensile failure. Therefore, the validity of the exported plastic failure point is confirmed.

Coulomb with linear softening model

For this newly implemented model, the peak shear strength (τ_{max}) of the discontinuity is not available from the software output and must be calculated manually. The obtained results from the stress analysis of the two examined nodes of the 1st discontinuity using the considered model after the calculation of the τ_{max} are presented in Table 6.6. Note that these points are also in a failure state.

Table 6.6: Results of the stress analysis of the 1st Discontinuity using the Coulomb with linear softening model

Structural element	Plastic point	Node	Local number	X [m]	Y [m]	σ'_N [kN/m²]	σ_N [kN/m²]	τ_1 [kN/m²]	State parameter	τ_{max} [kN/m²]
Discontinuity_7_18 Element 868-1149 (Discontinuity) (Disc3_UddMcSoft)	1	20181	5	-1.14	2.45	0.00	0.00	339.87	0.0004729	339.87
Discontinuity_7_18 Element 868-1151 (Discontinuity) (Disc3_UddMcSoft)	2	26463	1	-0.62	3.19	0.00	0.00	340.51	0.0003311	340.51

The current shear strength should be calculated based on the current normal stress, which are both zero for both these two points. It is important to note that at zero normal stress, the shear strength is less than the peak cohesion (342 kN), which can be explained by the fact that the points have already undergone softening. To exactly calculate the maximum shear strength the adopted state parameter had to be exploited using the VBin tool which is provided with the installation of PLAXIS software.

Knowing the number of each examined discontinuity element and knowing that each discontinuity element includes five nodes, the exact rows that correspond to the nodes which were selected for further investigation, were spotted. For each examined node two values are provided by the tool. The first value indicates whether the node is elastic or plastic while the second value indicates the value of the state parameter. If the node is elastic the first value is equal to 0. On the other hand, if the node is plastic the first value is equal to 1. The second value indicates the state parameter. The softened cohesion is calculated as follows:

$$c = c_{peak}\left(1 - \frac{\kappa}{Dc}\right) - c_{res}\left(\frac{\kappa}{Dc}\right) \leq 0 \tag{6.1}$$

Employing Equation (6.1) and the retrieved value of the state parameter the current value of cohesion was calculated. For both nodes, it can be seen that the current value of cohesion is equal to the obtained value of current shear stress indicating that both points are located consistently at the corner between the tensile and shear strength failure lines.

Coulomb with linear softening model (brittle)

In this case, the value of the τ_{max} of the discontinuity was also calculated manually. Furthermore, considering the brittle softening nature, the current cohesion drops immediately to the residual value (270 kN) once the point has reached failure. Table 6.7 presents the obtained results.

Table 6.7: Results of the stress analysis of the 1st Discontinuity using the brittle version of the Coulomb with linear softening model

Structural element	Plastic point	Node	Local number	X [m]	Y [m]	σ'_N [kN/m²]	σ_N [kN/m²]	τ_1 [kN/m²]	τ_{max} [kN/m²]	τ_{res} [kN/m²]
Discontinuity_7_18 Element 868-1149 (Discontinuity) (Disc4_UddMcSoft_brittle)	1	20181	5	-1.14	2.45	0.00	0.00	270.00	342.00	270.00
Discontinuity_7_18 Element 868-1151 (Discontinuity) (Disc4_UddMcSoft_brittle)	2	26463	1	-0.62	3.19	0.00	0.00	270.00	342.00	270.00

The depicted results in Table 6.7 denote that the values of the current shear stress for the examined points are equal to the adopted value of the cohesion at the residual state, which again indicates the failure state of these points and the consistency of the implementation.

Modified Barton-Bandis model

For the modified Barton-Bandis model, the same process as the one described in the case of Coulomb with the linear softening model was followed to obtain the value of the state variable (accumulated slip). The mobilized roughness JRC_{mob} (equation 3.65) is then evaluated to calculate the current shear strength. The obtained results are depicted in Table 6.8:

Table 6.8: Results of the stress analysis of the 1st Discontinuity using the modified Barton-Bandis model

Structural element	Plastic point	Node	Local number	X [m]	Y [m]	σ'_N [kN/m²]	σ_N [kN/m²]	τ_1 [kN/m²]	State parameter	τ_{max} [kN/m²]
Discontinuity_7_18 Element 868-1149 (Discontinuity) (Disc5_UddBB)	1	20181	5	-1.14	2.45	0.00	0.00	2.87	0.001	2.87
Discontinuity_7_18 Element 868-1151 (Discontinuity) (Disc5_UddBB)	2	26463	1	-0.62	3.19	-26.37	-26.37	52.31	0.0007211	52.31

The calculated values of current cohesion (for point 1) and peak shear strength (for point 2) were equal to the corresponding values of current shear stress which being exported by PLAXIS 2D. Therefore, the failure state of each examined plastic point along the examined discontinuity is justified.

6.3.2.2 Stress analysis of the second discontinuity

Similarly, to the analysis performed for the distribution of the stresses along the 1st Discontinuity, the evolution of both shear and normal stress along the 2nd Discontinuity was also assessed. Figure 6.20 and Figure 6.21 present the evolution of normal and shear stress along the examined discontinuity.

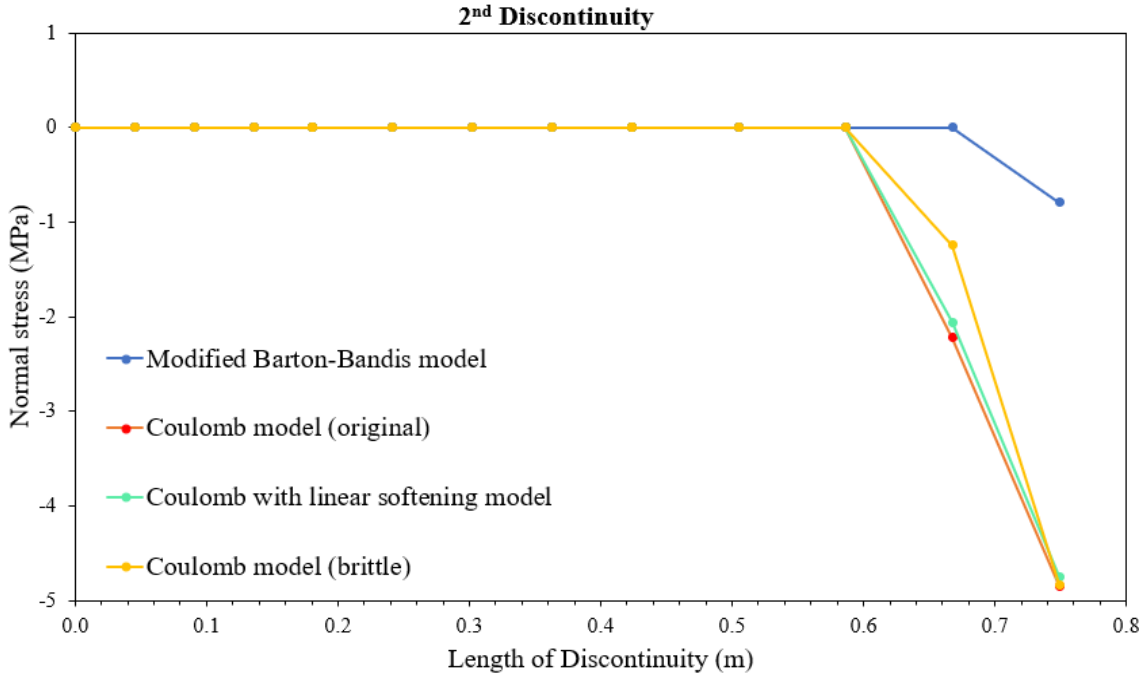

Figure 6.20: Evolution of normal stress along 2nd Discontinuity for each constitutive law

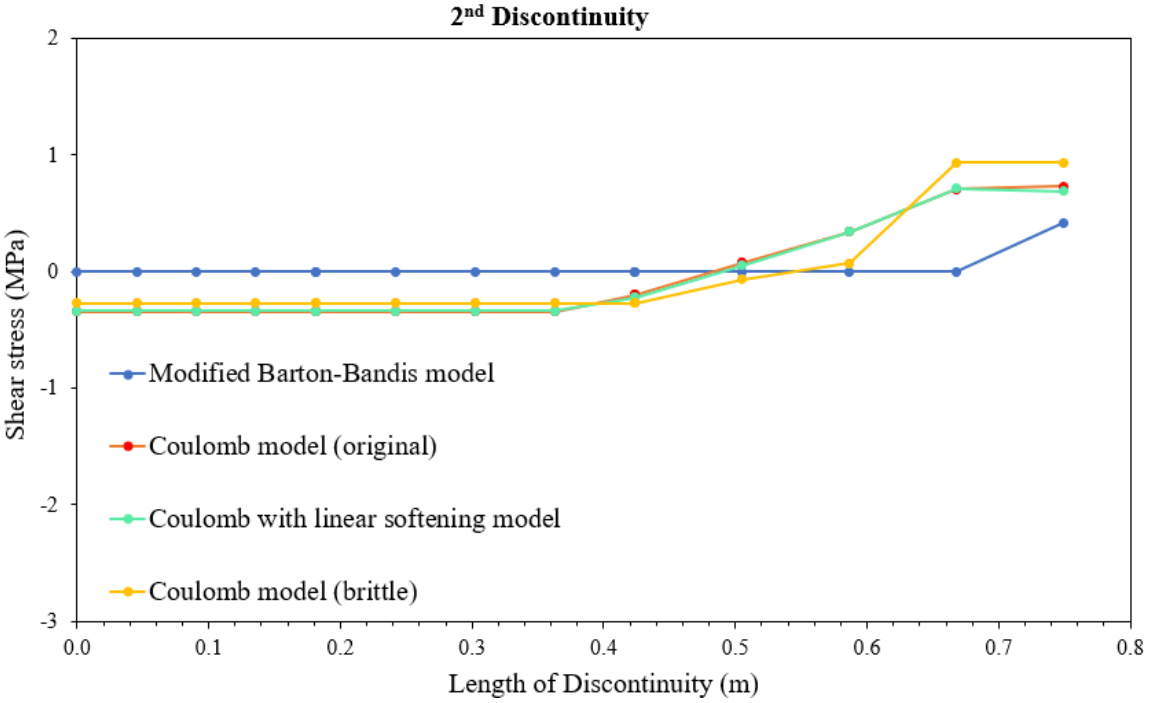

Figure 6.21: Evolution of shear stress along the 2nd Discontinuity for each constitutive law

The obtained results regarding the evolution of the normal stress along the 1st Discontinuity presented in Figure 6.20, indicate that for all constitutive models, the normal stress is null close to the excavated tunnel while an increment of the normal stress value is observed close to the point where the two examined discontinuities are intersected. Moreover, it should be noted that the extracted evolution of normal stress is in accordance with the distribution of the tension cut-off points along the examined discontinuity which is presented in Figure 6.12. More specifically, tension cut-off points are depicted in the same points where the value of normal stress is nil.

On the other hand, a considerable difference between the Coulomb-based models and the modified Barton-Bandis model is noted. Concretely, the obtained results show that the calculated value of peak normal stress employing the Coulomb-based models is considerably higher than the corresponding one using the Barton-Bandis model with linear reduction of roughness. This difference in the maximum value of the applied normal stress justifies also the observed difference in the obtained value of the maximum shear stress for each law.

As in the performed stress analysis for the 1st Discontinuity so in this case also a further investigation of the exported results was carried out to give an insight into the distribution of the stresses along the 2nd Discontinuity. Accordingly, to the performed analysis for the 1st discontinuity, the validity of the two plastic points as indicated by Figure 6.19.

Coulomb model original

The stress analysis started with the verification of the exported results using the original version of the Coulomb model. The obtained results are illustrated in Table 6.9:

Table 6.9: Results of the stress analysis of the 2nd Discontinuity using the original Coulomb model

Structural element	Plastic point	Node	Local number	X [m]	Y [m]	σ'_N [kN/m²]	σ_N [kN/m²]	τ_1 [kN/m²]	τ_{max} [kN/m²]
Discontinuity_3_26 Element 865-1144 (Discontinuity) (Disc_UddCoulomb_original)	1	27063	5	-0.06	2.70	0.00	0.00	-342.00	342.00
Discontinuity_3_26 Element 865-1146 (Discontinuity) (Disc_UddCoulomb_original)	2	30021	1	-0.62	3.19	-4845.05	-4845.05	706.08	4553.73

The depicted results in Table 6.9 indicate the obtained stress results of two nodes. Node 27063 corresponds to the point where the discontinuity intersects with the tunnel while node 30021 corresponds to the intersection point of the two discontinuities. For the first point, the value of the current shear stress (τ_1) is equal to the value of the peak shear strength (τ_{max}) which corresponds to the current normal stress level (easily calculated with the Coulomb criterion 3.36), indicating a shear failure state. For the second node, the value of τ_1 is less than the value of τ_{max} indicating that the stress state of the considered node remains in the elastic area. However, it must be pointed out that in the intersection point of the discontinuities, two points are overlapping. Considering that in the previously performed analysis using the Coulomb model the existence of the plastic failure point was justified it can be concluded that the obtained failure point corresponds to the first discontinuity while for the second discontinuity, no point was projecting (because for the applied normal stress no failure state occurs). Therefore, the validity of the exported plastic failure point is confirmed.

Coulomb with linear softening model

The second step of the analysis concerns the investigation of the obtained results after the simulation of the modelled underground rock excavation using the Coulomb with linear softening model. The analysis of the obtained results using the considered model was performed using the same process as the one described for the assessment of the validity of the extracted plastic points along the first discontinuity using the same model. The obtained results after the calculation of the τ_{max} Table 6.10:

Table 6.10: Results of the stress analysis of the 2nd Discontinuity using the Coulomb with linear softening model

Structural element	Plastic point	Node	Local number	X [m]	Y [m]	σ'_N [kN/m²]	σ_N [kN/m²]	τ_1 [kN/m²]	State parameter	τ_{max} [kN/m²]
Discontinuity_3_26 Element 865-1144 (Discontinuity) (Disc3_UddMcSoft)	1	27063	5	-0.06	2.70	0.00	0.00	-337.24	0.001056792	337.24
Discontinuity_3_26 Element 865-1146 (Discontinuity) (Disc3_UddMcSoft)	2	30021	1	-0.62	3.19	-4744.36	-4744.36	689.85	0.00	-3782.21

For the first point it is important to note that at zero normal stress, the shear strength is less than the peak cohesion (342 kN), which can be explained by the fact that the points have already undergone softening. Therefore, using Equation (6.1) and the retrieved value of state parameter the current value of cohesion was calculated. The calculated value of cohesion is equal to the obtained value of current shear stress indicating that the first point is located consistently at the corner between the tensile and shear strength failure lines. Additionally, for the second point the value of the peak shear strength (τ_{max}) which corresponds to the current normal stress level was calculated denoting that the calculated value is larger than the obtained value of the τ_1. Considering this condition, it can be stated that the examined point is elastic. Therefore, the reliability of the exported results is confirmed.

Coulomb with linear softening model (brittle)

The next step of the analysis was focused on the investigation of the results obtained after the simulation of the considered underground excavation using the brittle version of the Coulomb with linear softening model. According to the previously presented results, the value of the τ_{max} of the discontinuity was also calculated manually. Furthermore, as stated before considering the brittle softening nature, the current cohesion drops immediately to the residual value (270 kN) once the point has reached failure. Table 6.11 presents the obtained results:

Table 6.11: Results of the stress analysis of the 2nd Discontinuity using the brittle version of the Coulomb with linear softening model

Structural element	Plastic point	Node	Local number	X [m]	Y [m]	σ'_N [kN/m²]	σ_N [kN/m²]	τ_1 [kN/m²]	τ_{max} [kN/m²]	τ_{res} [kN/m²]
Discontinuity_3_26 Element 865-1144 (Discontinuity) (Disc4_UddMcSoft_brittle)	1	27063	5	-1.14	2.45	0.00	0.00	-270.00	342.00	270.00
Discontinuity_3_26 Element 865-1146 (Discontinuity) (Disc4_UddMcSoft_brittle)	2	30021	1	-0.62	3.19	-4833.52	-4833.52	909.56	4543.72	3781.76

The depicted results in Table 6.11 denote that the values of the current shear stress for the first examined point is equal to the adopted value of the cohesion at the residual state, which again indicates the failure state of this point. However, the extracted value of the current shear stress for the second examined point is lower than the peak shear strength which corresponds to the current normal stress denoting that the considered point is elastic. Therefore, the consistency of the implementation is confirmed.

Modified Barton-Bandis model

The final step of the analysis regarding the investigation of the obtained stress results along the 2nd discontinuity concerns the modified Barton-Bandis model. The same process as the one described in the case of Coulomb with the linear softening model was followed to obtain the value of the state variable (accumulated slip). The mobilized roughness JRC_{mob} (equation 3.65)

is then evaluated to calculate the current shear strength. The obtained results are depicted in Table 6.12.

Table 6.12: Results of the stress analysis of the 2nd Discontinuity using the modified Barton-Bandis model.

Structural element	Plastic point	Node	Local number	X [m]	Y [m]	σ'_N [kN/m²]	σ_N [kN/m²]	τ_1 [kN/m²]	State parameter	τ_{max} [kN/m²]
Discontinuity_3_26 Element 865-1144 (Discontinuity) (Disc5_UddBB)	1	27063	5	-1.14	2.45	0.00	0.00	-2.75	0.00122	2.75
Discontinuity_3_26 Element 865-1146 (Discontinuity) (Disc5_UddBB)	2	30021	1	-0.62	3.19	-793.22	-793.22	416.76	0.00	705.31

The calculated value of current cohesion (for point 1) was equal to the corresponding value of current shear stress which has being exported by PLAXIS 2D justifying the existence of the extracted failure point. On the other hand, the extracted value of the current shear stress for the second examined point is lower than the peak shear strength which corresponds to the current normal stress denoting that the considered point is elastic. Therefore, the stress state of each examined plastic point along the examined discontinuity is verified.

6.3.2.1 Results of the analysis

The performed analysis of the stress regimes that govern the behaviour of the two discontinuities which form the wedge at the roof of the excavated tunnel denote that the employed constitutive laws result in noticeable differences regarding the level of the applied normal stress and the evolution of shear stress along the examined discontinuities.

More specifically, the obtained results using the Coulomb-based models showed a higher value of peak normal stress in comparison with the one obtained using the implemented version of Barton-Bandis. This difference consequently leads to a smaller value of shear strength using the modified Barton-Bandis model. Additionally, it must be pointed out that the performed analysis indicated that in the framework of the considered engineering application, no difference was noted between the original Coulomb model and the Coulomb with linear softening model. This behaviour of the considered models is closely related to the obtained results illustrated in Figure 6.9. In more detail, as was described in Section 6.3.1 a non-considerable amount of displacements is caused due to the excavation of the simulated tunnel. Considering the small amount of displacement in combination with the fact that the behaviour of the Coulomb model in comparison with the behaviour of the Coulomb with linear softening model differs significantly at the post-peak area, it can be safely assumed that the generated displacements are not enough to denote the capabilities of the most advanced constitutive relationships adopted by the Coulomb with linear softening model.

Therefore, the aforementioned observations lead to the following conclusions regarding the stability of the examined discontinuity using the implemented constitutive laws:

- Coulomb-based models: Despite the several plastic failures and tension cut-off points the wedge at the roof of the tunnel is stabilised after a relatively small amount of displacements The stabilisation of the wedge can be explained considering that the Coulomb-based models generate high normal stress levels which consequently lead to adequately high shear strength levels to secure the stability of the wedge. In addition, the adopted value of cohesion which controls the shear strength at the areas where no normal stress is applied is large enough to resist the gravitational loading and prevent the collapse of the wedge.

- Modified Barton-Bandis model: Several plastic failure and tension cut-off points were also obtained employing the modified Barton-Bandis model. However, even though considerably lower values of stresses are generated using the considered model in comparison with those extracted using the Coulomb-based models, it was concluded that the generated stresses are enough to keep the wedge stable. Additionally, similar to the Coulomb-based models, the adopted value of cohesion which was added to the implemented version of the Barton-Bandis model after the described modifications, was judged adequate to prevent the occurrence of a failure mechanism along the discontinuities which form the examined wedge.

7 Conclusion and recommendations

The aim of this research project was to evaluate the capabilities and the limitations of different constitutive laws for rock discontinuities in terms of numerical implementation and modelling of the mechanical behaviour of fracture rock masses. To accomplish the research objective, the following research questions were formulated.

The first question concerns on how the mechanical behaviour of a discontinuity can be modelled. The carried-out literature review indicated that several constitutive models have been introduced by many researchers which help the rock engineers to understand the mechanical behaviour of discontinuities. These models are of either theoretical or empirical nature with different degrees of complexity. In this research project, two constitutive laws were selected for a more detailed investigation due to their high adoption in research and industry: the Coulomb law and its enhanced versions, and the modified Barton-Bandis model. The first constitutive law concerns the Coulomb model which is considered as the most adopted model in engineering practice. The Coulomb model is a simple model with a small number of easy-to-determine parameters. However, because of its simplicity, it cannot capture several features of the mechanical behaviour of the discontinuities. Considering its limitations, the Coulomb model was enhanced with the addition of strain softening, residual dilation and dilation cut-off. The enhanced model was implemented as a user-defined model in PLAXIS 2D.

To answer the second research question, concerning the proper validation of the implemented model, a simple numerical model of two rock blocks and a single discontinuity was simulated in PLAXIS 2D (as described in detail in Section 5.2). Employing the created model, the implementation was successfully verified against the theoretical simulation and experimental data for the behaviour of a discontinuity subject to shearing under Constant Normal Load (CNL) conditions. This enhanced version proves to be able to reproduce more accurately the mechanical response of discontinuity than the original Coulomb model by capturing with adequate accuracy several important features of the peak and residual shear strength, as well as the non-linear evolution of dilation usually observed in the post-peak region. Compared to the existing Coulomb brittle softening model in PLAXIS which uses a unique reduction factor for both friction angle and cohesion, this enhanced version allows for a more flexibility in the calibration of experimentation, as well as a better representation of post-peak dilation. Additionally, the adopted enhancements allow for a more accurate representation of the post-peak dilation in contrast with the current PLAXIS Coulomb brittle model which assumes a nil residual dilation.

The second constitutive law which was selected for further investigation was the Barton-Bandis model which is probably one of the most cited models in research. The model can generally reproduce more accurately the strength envelope as well as the non-linear behaviour of a discontinuity subject to shear displacement. Their parameters, although not very easy to determine, have clear physical meaning. However, its high non-linearity and especially the empirical nature makes the numerical implementation of the model challenging.

Considering these limitations several improvements were adopted to the Barton-Bandis model to enhance its applicability to ensure the theoretical rigorousness. Firstly, considering that during the simulation of an engineering application, several stress paths along the $\tau - \sigma_n$ space

will occur, the applied improvements were focused on the mathematical treatment of the model to ensure its validity in the areas of high and low normal stress. Therefore, within the framework of this thesis, the modifications described in Section 3.5 were applied to the mathematical formulations of the Barton-Bandis model and an open and convex yield surface which is valid for every stress state was adopted. The second set of improvements was focused on the generation of a linear approximation of the highly non-linear Barton-Bandis model which can provide accurate results and be aligned with the considerations of Barton regarding the contribution of the roughness of the discontinuity walls in the evolution of shear strength. Concretely, the linear softening feature was adopted to the examined law with the application of a reduction factor whose value was dependent on the value of the state parameter. The formulated reduction factor was applied to the JRC_{peak} to reduce linearly its value and represent the concept of mobilized roughness. In this way, a simplified model that can capture the shear strength of the post-peak area was formulated based on the Barton-Bandis model.

The modified Barton-Bandis model was implemented as a user-defined model in PLAXIS 2D. Accordingly to the implemented Coulomb model the validity of the modified Barton-Bandis model was verified by employing the same numerical model created in PLAXIS 2D and by comparing the simulation results of CNL shear tests with theoretical and experimental data. The obtained results indicated that the created model could capture the trend of the mechanical response of a discontinuity, including the peak and residual strength, although a conservative estimation of the strength evolution in the post-peak area is observed. The model could reproduce the dilation onset and evolution which is tightly related to the mobilized roughness. The obtained results indicated that the higher the amount of the mobilized roughness is, the larger the amount of dilation is. Moreover, when the amount of mobilized roughness is equal to zero indicates the end of the dilation and the complete shearing-off of the asperities. However, the empirical nature of the model seems to have little flexibility to capture quantitatively the evolution of dilation of different types of discontinuity, as no dilation parameter is available for such a calibration of the dilation curve.

To answer the last question regarding the ability of the implemented constitutive laws to capture the real mechanical behaviour of fractured rock mass in a large-scale problem, their applicability was examined more extensively in a finite element simulation of a deep underground rock excavation in a discontinuous rock mass. For this practical application, considering that the projection of a realistic discontinuity network is a challenging and time-consuming process, improvements were made to an existing generator tool that allows for the automatic generation of a discontinuity network by means of the PLAXIS Python scripting API. Employing the improved version of the tool the whole model geometry of the considered underground excavation was generated including two inclined fully persistent with random spacing discontinuity sets. The obtained results denoted that through the adopted improvements a useful and efficient tool for the automatic generation of realistic discontinuity networks had been created.

Additionally, the performed FE simulations further validate the numerical implementation of the models. More concretely, deformation and local failure around the tunnel, as well as stresses developed in the discontinuities of the most critical wedges agreed with physical observation. The performed analysis showed that in this case, where only a small amount of displacement is expected compared to the critical distance, and the softening is not so significant, the original Coulomb model and the enhanced version of the Coulomb model with linear softening do not indicate significant differences in the calculation of the generated stresses. Finally, for the considered engineering application it was noted that the modified Barton-Bandis model

generated lower stresses for the tensile discontinuities due to its low cohesive strength, which might imply more instabilities on the critical wedges.

Finally, the simulations performed in both lab and large scales indicated that the examined constitutive laws could provide reliable results regarding the mechanical behaviour of rock discontinuities. Based on the employed implemented versions of the examined models and the examined large-scale engineering application, the results highlight the importance for rock engineering practitioners to first consider the stress ranges that should be taken into account in the project to be designed before the selection of a more advanced law. In more detail, the simulated underground excavation performed within the framework of this research work indicated that for the considered stress levels the yield surfaces of the examined models do not present significant differences to justify the selection of a more advanced constitutive laws, which would require a more challenging calibration of empirical parameters. The results in terms of deformations indicated that the investigated constitutive laws reproduce comparable results while in terms of stability, it can be noted that at low-stress levels the Barton-Bandis model provide a more conservative solution in comparison with the Coulomb-based models. Therefore, engineering judgment is always required to decide the most efficient way to model the behaviour of a rock discontinuity based on the effectiveness of the model and the easiness of the calibration of the required parameters.

This research work opens several directions for future works. Firstly, only linear stiffnesses are considered in this work. Nonlinear stiffnesses will be considered in a future implementation, especially in the context of hydro-mechanical coupling where mechanical aperture mutually interacts with fluid flow through the discontinuity. Secondly, other enhancements on the dilative behaviour of the Barton-Bandis model, more realistic roughness mobilization law, as well as other constitutive laws, will be considered. Finally, it is important to note that this study focuses on the validation of the numerical enhancements and implementation of the models. A more in-depth study on different applications will be needed to clarify further the applicability of different models in rock practical engineering.

8 References

Bandis, S., Lumsden, A., & Barton, N. (1983). Fundamentals of rock joint deformation. International Journal of Rock Mechanics and Mining Sciences & Geomechanics Abstracts, 20 (6), 249–268.

Barton, N. (1976). The shear strength of rock and rock joints. International Journal of rock mechanics and mining sciences & Geomechanics abstracts, 13 (9), 255–279.

Barton, N., et al. (1978). Suggested methods for the quantitative description of discontinuities in rock masses. ISRM, International Journal of Rock Mechanics and Mining Sciences & Geomechanics Abstracts, 15 (6), 319–368.

Barton, N., Bandis, S., & Bakhtar, K. (1985). Strength, deformation and conductivity coupling of rock joints. International journal of rock mechanics and mining sciences & geomechanics abstracts, 22 (3), 121–140.

Barton, N., & Choubey, V. (1977). The shear strength of rock joints in theory and practice. Rock mechanics, 10, 1–54.

Bentley Systems Incorporated. (2023). PLAXIS 2D v2023.01-Manuals 2D.

Brown, S. R., & Scholz, C. H. (1986). Closure of rock joints. Journal of Geophysical Research: Solid Earth, 91 (B5),4939–4948.

Duffaut, P. (2013). The traps behind the failure of malpasset arch dam, france, in 1959.Journal of Rock Mechanics and Geotechnical Engineering, 5 (5), 335–341.

Gens, A., Carol, I., & Alonso, E. (1990). A constitutive model for rock joints formulation and numerical implementation. Computers and Geotechnics, 9(1-2), 3–20.

Goodman, R. (1970). The deformability of joints. In Determination of the in situ modulus of deformation of rock. ASTM International.

Goodman, R. E., et al. (1989). Introduction to rock mechanics (Vol. 2). Wiley New York.

Grasselli, G., & Egger, P. (2003). Constitutive law for the shear strength of rock joints based on three-dimensional surface parameters. International Journal of Rock Mechanics and Mining Sciences, 40 (1), 25-40.

Hakami, E. (1995). Aperture distribution of rock fractures (tech. rep.). Royal Inst. of Tech.

Itasca Consulting Inc. (2019). 3DEC manuals version 7.0.

Jing, L., & Stephansson, O. (2007). Fundamentals of discrete element methods for rock engineering:Theory and applications. Elsevier.

Ladanyi, B., & Archambault, G. (1969). Simulation of shear behavior of a jointed rock mass. Proceedings of the11th Symposium on Rock Mechanics, 1.

Ladanyi, B., & Archambault, G. (1980). Direct and indirect determination of shear strength or rock mass.

Lei, Q., & Barton, N. (2022). On the selection of joint constitutive models for geomechanics simulation of fractured rocks. Computers and Geotechnics, 145, 104707.

Leichnitz, W. (1985). Mechanical properties of rock joints. International Journal of Rock Mechanics and Mining Sciences & Geomechanics Abstracts, 22 (5), 313–321.

Nassir, M. (2013). Geomechanical coupled modelling of shear fracturing in non-conventional reservoirs (Doctoral dissertation). University of Calgary.

Pratt, H., Black, A., Brown, W., & Brace, W. (1972). The effect of speciment size on the mechanical properties of unjointed diorite. International Journal of Rock Mechanics and Mining Sciences & Geomechanics Abstracts, 9 (4), 513–516.

Priest, S. D. (1993). Discontinuity analysis for rock engineering. Springer Science & Business Media.

Saeb, S., & Amadei, B. (1992). Modelling rock joints under shear and normal loading. International journal of rock mechanics and mining sciences & geomechanics abstracts, 29 (3), 267–278.

Skinas, C., Bandis, S., & Demiris, C. (1990). Experimental investigations and modelling of rock joint behaviour under constant stiffness. International symposium on rock joints, 301–308. Page 27

Thirukumaran, S., & Indraratna, B. (2016). A review of shear strength models for rock joints subjected to constant normal stiffness. Journal of Rock Mechanics and Geotechnical Engineering, 8 (3), 405–414.

Wyllie, D. C., & Mah, C. (2004). Rock slope engineering. CRC Press.